NASA CR-~~144839~~

R-963

FINAL REPORT

ADVANCED EARTH OBSERVATION SYSTEM INSTRUMENTATION STUDY

(AEOSIS)

by

Robert E. Var

June 1976

The Charles Stark Draper Laboratory, Inc.

Cambridge, Massachusetts 02139

1. Report No.	2. Government Accession No.	3. Recipient's Catalog No.
4. Title and Subtitle FINAL REPORT ADVANCED EARTH OBSERVATION SYSTEM INSTRUMENTATION STUDY		5. Report Date May 31, 1976
		6. Performing Organization Code
7. Author(s) Robert E. Var		8. Performing Organization Report No. R-963
9. Performing Organization Name and Address The Charles Stark Draper Laboratory, Inc. 68 Albany Street Cambridge, MA 02139		10. Work Unit No.
		11. Contract or Grant No. NAS 5-21917
		13. Type of Report and Period Covered
12. Sponsoring Agency Name and Address Goddard Space Flight Center National Aeronautics and Space Administration Greenbelt, MD 20771 (Tech. Monitors: S. Kant/720.0; B. Peavey/563.0)		Final Report 1 December 1974 to 31 December 1975
		14. Sponsoring Agency Code
15. Supplementary Notes		

16. Abstract

This report represents the results of an investigation into the feasibility, practicality, and cost of establishing a national system or grid of artificial landmarks suitable for automated (near real time) recognition in the multispectral scanner imagery data from an EOS spacecraft. The intended use of such landmarks, for orbit determination and improved mapping accuracy is reviewed, and the desirability of using xenon searchlight landmarks for this purpose is explored theoretically and by means of experimental results obtained with Landsat 1 and Landsat 2. These results are then used, in conjunction with the demonstrated efficiency of an automated detection scheme, to determine the size and cost of a xenon searchlight that would be suitable for an EOS Searchlight Landmark Station (SLS). This result is then used in turn to facilitate the development of a conceptual design for an automated and environmentally protected EOS SLS. An attempt is then made to describe the tasks that would have to be completed in order to obtain a realistic estimate for the expense associated with the fabrication, installation, operation, and maintenance of a national system of 100 SLS's.

17. Key Words Suggested by Author Earth Observation Spacecraft Landmark Utilization by EOS Xenon Searchlight Landmark Stations Optimum Beacon Landmarks	18. Distribution Statement

19. Security Classif. (of this report) Unclassified	20. Security Classif. (of this page) Unclassified	21. No. of Pages 141	22. Price

R-963

FINAL REPORT

ADVANCED EARTH OBSERVATION SYSTEM
INSTRUMENTATION STUDY

(AEOSIS)

by

Robert E. Var

June 1976

Approved: _N.E. Sears_

The Charles Stark Draper Laboratory, Inc.
Cambridge, Massachusetts 02139

ACKNOWLEDGEMENTS

TABLE OF CONTENTS

LIST OF ILLUSTRATIONS

LIST OF ILLUSTRATIONS (Cont.)

LIST OF TABLES

GLOSSARY OF SYMBOLS

Symbol	Units	Definition
Rad	Radian(s)	Unit of Two-Dimensional Angular Measure.
Str	Steradian(s)	Unit of Three-Dimensional Angular Measure.
M	Meter(s)	Unit of Length
W	Watt(s)	Unit of Power.
μ	Micron	Unit of Wavelength Equal to 10^{-6}M.
i	--	MSS Channel Number Index. (4-7 for Landsat MSS), (1-4 for EOS MSS).
λ_i	μ	Center Wavelength of ith MSS Channel
θ	Rad	Unit of Angular Measure.
ϕ	Rad	Unit of Angular Measure.
θ_D	Rad	Linear Optical Field of View of MSS Detector
θ_S	Rad	Angle Scanned by MSS (in Section 2.0). Angle Subtended by Diameter of Solar Disc (in Appendix C).
θ_T	Rad	Total Intract Field of View of MSS Detector Array.
θ_{DR}	Rad	Reference Field of View for MSS Detector.
θ_{N_D}	--	Linear Optical Field of View of MSS Detector in Units of θ_{DR}.
Ω_A	Str	Solid Angle Subtended by MSS Aperture Lense.

Symbol	Units	Definition
Ω_D	Str	Solid Field of View of MSS Detector $(\Omega_D = \theta_D^2)$.
A_A	M^2	Area of MSS Aperture Lens.
A_{DG}	M^2	Earth's Surface Area Intercepted by Ω_D.
AT_i	--	Atmospheric Transmission Factor for Reflected Solar Radiation.
BR_{GMi}	W/M^2-str	Bolometric Radiance at MSS Aperture Lens Corresponding to a Maximum MSS Output Signal for the ith Channel.
BW_i	μ	Bandwidth of ith MSS Channel
D_S	M	Diameter of Image Spot or Blur Circle Produced in MSS Image Plane by Plane Parallel Radiation (estimated for the Landsat MSS).
D_S'	M	Theoretical (Diffraction Limited) Diameter of Central Image Spot Produced by Plane Parallel Radiance.
DT	Seconds	Dwell Time for MSS Detector.
$EBPA_i$	% Full Scale	Experimental Beacon Pulse Amplitude in ith Channel of Landsat MSS.
f	M	Focal Length of MSS Imaging Optics.
F_i	M^2/W	MSS Channel Sensitivity Constants for Xenon Searchlight Landmark Beacon.
FD	--	Fraction of MSS Detector Dimension (L) Contained in Blur Circle.
FT_i	--	Filter Transmission Factors for Solar Beacon Landmark Mirror.

Symbol	Units	Definition
g	--	Ratio of MSS Detector Sampling Repetition Period (T_{SR}) to the Detector Dwell Time (DT).
G_i	% FS/M^2	MSS Channel Sensitivity Constants Solar Beacon Landmarks.
I	$W/M^2 - \mu$	Irradiance of Solar or Searchlight Radiation.
$I_o(\theta)$	W/M^2	Measured Bolometric Radiation Intensity (Profile) From Xenon Searchlight.
L	M	Linear Dimension of MSS Detector
α_i	--	The ratio of $(D_S)_i$ to L.
OT_i	--	Vertical Optical Thickness of a Standard Clear Atmosphere.
PAS_i	$\dfrac{\% \text{ Full Scale}}{W/M^2}$	Pulse Amplitude Sensitivities of Landsat MSS for Xenon Searchlight Landmark Pulses.
P_{BD}	W	Beacon Power Contained in Blur Circle (Spot Image).
PCF_i	--	Power Correction Factors, Normalized to 15 kw.
P_{ED}	W	Extended Source (background) Power Imaged on MSS Detector.
R	M	Altitude of MSS Above Earth's Surface.
R_G	$W/M^2 - \mu - str$	Radiance of Light From an Extended Source
R_o	M	Distance From Xenon Searchlights at Which Values of $I_o(\theta)$ Were Measured.

GLOSSARY OF SYMBOLS (Cont.)

Symbol	Units	Definition
T_S	Seconds	Time Interval for Active Portion of Forward Scan of MSS Mirror.
T_{SR}	Seconds	Sampling Repetition Period. The Time Interval Between Successive Samples of a Given MSS Detector.

SECTION 1

INTRODUCTION AND SUMMARY

1.1   INTRODUCTION

This report has been prepared as the Final Report in a series
of studies performed by the Charles Stark Draper Laboratory, Inc.,
(CSDL), for the NASA Goddard Space Flight Center (GSFC), during the
period from 13 April 1973 to 31 December 1975. The present report
gives the results of a recent study conducted during the period from
1 February 1974 to 31 December 1975 which is referred to as the Arti-
ficial Landmark Implementation Study (ALIS). This study was an inves-
tigation into the feasibility, practicality, and cost of establishing
a national system of artificial landmarks suitable for automated recog-
nition in the electronic processing of imagery data from an Earth
Observation Satellite (EOS). The results of the other studies performed
under this contract are presented in References 1, 14, 15 and 16.

1.1.1   Background

The ALIS study was motivated by the preliminary results of
another study performed by CSDL for NASA (GSFC), during the period from
1 February 1974 to 31 July 1974. That study, herein referred to as the
Landmark Utilization Study (LUS), was an investigation into the feasibil-
ity of using ground truth data, associated with selected landmarks in
the EOS imagery, and also star measurement data in combination with
landmark data, to estimate the orbital ephemeris, attitude and gyro bias
drift of EOS satellites.

The preliminary findings of the LUS study indicated that the
automated recognition of a small number of ground targets (in the EOS
imagery data) in combination with star measurement data (from an on-
board star tracker) could be used to determine the orbital ephemeris of
the EOS spacecraft and to create a significant improvement in the geo-
metric mapping accuracy of the telemetered imagery data. These prelimi-
nary findings of the LUS study were subsequently substantiated by a more
detailed analysis which indicated that the above benefits could be ob-
tained with as little as ten star sightings per orbit and just one or
two landmark sightings per orbit.[1] These findings were derived by

means of a statistical covariance analysis, employing optimal filtering and smoothing techniques to process the star and landmark measurement data along with the ordinary attitude and gyro bias drift data. In this way, star and landmark data were used to update the spacecraft attitude and gyro bias drift data, and to determine the orbital ephemeris of the spacecraft. The accuracy of the latter was found to be comparable with the accuracy of the ephemeris estimates ordinarily obtained from the data supplied by ground tracking stations. Thus it was concluded that the use of landmark and star measurement data in this manner could provide two potential benefits for NASA's EOS program. Namely, an attractive alternative to ground tracking for the purpose of orbit determination and a significant improvement in the geometric accuracy or fidelity of the telemetered earth imagery data.

It was noted however, that the potential exploitation of ground truth data, for the purposes envisioned by the LUS study, imposed certain requirements on the types of landmarks that would be most useful. Namely, those types that could be accurately and reliabily detected in the imagery data stream by means of an automated process involving a minimal amount of computer time and hardware. This latter requirement was due in part to the belief that several additional benefits could possibly be realized if the automated landmark detection scheme could be economically implemented in the EOS spacecraft itself rather than in a ground based data processing facility. These additional potential benefits relate to improvements in the precision of the onboard attitude control scheme and the fact that the location (or time of occurrence) of each landmark could then be conveniently recorded and subsequently identified (in the data processing) by means of a specific word in the down link data stream. The possibility of realizing these additional benefits served therefore to augment the desire for an extremely rapid and efficient automated landmark detection scheme.

Section 2.1 describes the historical reasons for believing that these stringent landmark detection requirements could be satisfied by using man made or artificial landmarks consisting of and defined by any sufficiently powerful source of radiation in the visible and/or near IR portions of the electromagnetic spectrum. In brief, it was theorized

that the electronic signature of such radiation sources (hereafter re-
ferred to as beacon landmarks) should consist of a narrow (essentially
single pixel) pulse, superimposed on the relatively low frequency
(quasi d.c.) background signal generated by an EOS multispectral scanner.
The theorized pulse signature of beacon landmarks therefore provided a
reasonably sound theoretical basis for envisioning a standardized auto-
mated landmark detection scheme, based on the well known techniques of
pulse detection, that could provide an intrinsically high precision
with a minimal amount of computer time and hardware. It was realized,
however, that the net value of a beacon landmark utilization program
would depend on the answers to a number of questions relating to the
feasibility, practicality, and costs associated with the construction
and performance of beacon landmark stations per se, and the implement-
ation and operation of a national grid of approximately 100 such stations
through the United States. The ALIS study was therefore undertaken with
the general objective of generating answers to these types of questions,
and the scope of the study was later expanded to include a series of
beacon landmark experiments with Landsat 1 and Landsat 2. The structure
of the ALIS study and the conclusions reached are briefly summarized in
the following section.

1.2   . SUMMARY

1.2.1 Beacon Landmark Trade Study

    . Section 2.2 describes the results of a trade study which examined
the relative technical merits and costs of various candidate types of
radiation sources for a beacon landmark station. The types of radiation
sources considered by the study included visible and IR lasers, flat
and curved mirrors, and high intensity searchlights covering the visible
and near IR portions of the electromagnetic spectrum. The results of
this study suggested that a Xenon searchlight would be the most prac-
tical and cost effective type of radiation source for a beacon type
landmark station. The practicality of using either visible or IR lasers
as sources for a fixed beacon landmark was found to be severely limited
by either their intrinsically low output powers or by their relatively
low efficiences for converting electrical power into useful radiant
power. In general, one pays a very high price per watt of radiant power
for the highly monocromatic and collimated features of a laser beam,
neither of which is actually required or even desired for a fixed beacon

landmark source. The practicality of using a curved solar reflector as a source for a fixed beam artificial landmark was found to be severely-limited by the uncommonly large surface that would be required to accommodate seasonal changes in the solar zenith angle. Smaller reflector surfaces could be utilized, but only at the expense of a two degree of freedom sun tracking and pointing system. Thus, the particular advantages that lasers and solar reflectors would otherwise offer, if the requirements called for a monochromatic and/or highly collimated beacon, turned out to be of little value for meeting the cost requirements of a fixed beacon landmark. The size and pointing requirements for a Mirror Landmark Station or MLS are derived and discussed in detail in Appendix C.

Subsequent investigations into the efficiency and maximum radiant power obtainable with conventional sources of broad band radiation revealed some rather surprising facts of particular value for the selection of a cost effective landmark beacon. Throughout the past decade or so a significant technological advancement has been achieved in the area of concentrated high intensity light sources, primarily through the development of the xenon short-arc discharge projection lamp. Featuring an operating efficiency of nearly 50%, a very minimum of maintenance over a long life (approximately 1000 hours), and push button start up, xenon lamps can provide up to 10,000 watts of radiant power with a spectral distribution closely matching that of the sun. These desirable attributes of the xenon short-arc lamp account for the appearance, over the past decade, of many new types of optical equipment including new and compact types of military and commercial searchlights, signaling beacons, solar simulators, and wide screen projectors. Because of these factors it was determined (in Section 2.6) that a commercially available xenon searchlight, rated at 4 kilowatts (d.c. input power), should adequately satisfy the intensity requirements for an EOS landmark beacon, in the most practical and cost effective manner. The approximate cost of these xenon searchlights, including a power supply for operation from a 220 volt, 60 cycle single phase line, and a power relay or line contactor for remote control switching operations, is currently estimated at $7,000.00 (in lots of 100).

1.2.2 Theoretical Signature Characteristics of Xenon Searchlight Landmarks

Section 2.3 describes the theoretical model developed for pre-

dicting the pulse amplitude of a Xenon searchlight signature in the various output channels of a multispectral scanner (MSS) like the MSS in the current Landsat spacecraft and/or the MSS planned for the EOS spacecraft. For the purposes of this summary it is noted that the model transforms the actual (measured) bolometric intensity of a Xenon search-light into the theoretical amplitude of the pulse response expected in each MSS channel expressed as a percent of the full scale range for each channel. · The pulse amplitude model is therefore formulated entire-. ly in terms of empirically known wavelength dependent parameters and intensity calibration data for the MSS and the Xenon searchlight under consideration.

A significant prediction generated by this model is that the pulse amplitude in the near IR channel should be nearly twice as large as the pulse amplitude in the first (visible) channel. This contrasts significantly with the spectral response of pulses that may be readily generated by a variety of man made and natural specular reflectors of solar radiation. In the latter case the near IR pulse amplitude would nominally be expected to be less than that observed in the first visible channel. This distinguishing characteristic of a Xenon searchlight land-mark is due to the existence of a pronounced XENON FLARE in the near IR portion of a high intensity Xenon discharge. Consequently, it was anticipated that this feature of a Xenon searchlight landmark could be exploited to improve the selectivity, and to therefore reduce the min-imum pulse amplitude threshold requirement for an automated detection scheme.

1.2.3 Empirical Signature Characteristics of Xenon
       Searchlight Landmarks

The accuracy of the theoretical Xenon searchlight signature (pulse amplitude) model was determined by means of a series of Xenon searchlight experiments that were carried out with Landsat 1 and Landsat 2 during the period from 3 November 1974 to 26 June 1975. The experi-mental program was conducted with the generous (unfunded) support of the New Hampshire Army National Guard (Searchlight Battery A, of the 197th Field Artillery Group), which furnished the portable (tactical) Xenon searchlights and the necessary vehicles and volunteer personnel required for their transportation and operation.[2]

The experimental searchlight landmark program resulted in the acquisition of 17 searchlight landmark data points in the Landsat MSS imagery data, providing 68 spectrally distinct searchlight signatures (in the four MSS bands) from 11 spatially resolved and non overlapping scan lines. This statistically significant data base was generated from eight separate experiments that were conducted at six different geographical locations (cities) encompassing the states of New Hampshire, Massachusetts, New York, and Utah. The multiplicity of searchlight landmark data points resulted from the use of two or three spatially resolved lights in a few of the experiments and a total of nine spatially resolved searchlights in the last experiment.[3] Details concerning these experiments and the results obtained are presented in Section 2.4.

1.2.4   Signature Modeling Accuracy

The accuracy of the signature (pulse amplitude) model is determined in Section 2.5 by comparing the theoretically predicted pulse amplitudes in each wavelength channel of the Landsat MSS with the averaged values of the pulse amplitudes obtained from the digitized Landsat imagery data. On the basis of this analysis, the empirical pulse heights were found to be generally greater than the model predictions, with fractional excesses of 7.7, 4.8, -.03 and 10 percent (for the .55, .65, .75 and .95 micron channels) and corresponding standard (1σ) deviations of 26, 22, 21, and 15 percent. The decrease in the standard deviation with wavelength was found to be consistent with the predicted and observed increase of pulse height with wavelength. Thus, to the accuracy indicated above, the Xenon searchlight experiments with Landsat 1 and Landsat 2 served to establish the validity of the predictive model and the anticipated factor of two enhancement of the band 7 pulse amplitude relative to the band 4 pulse amplitude.

1.2.5   Selection of a Prototype Xenon Searchlight for an EOS SLS

The above results were then utilized, in the manner described in Section 2.6 to determine the size (or power rating) and cost of a Xenon searchlight that would be suitable for an EOS searchlight landmark station or SLS. In brief, the Landsat imagery data (obtained from the experimental program) was used to facilitate the design and testing of a digital Xenon Searchlight Landmark Detection (XSLD) algorithm. The

XSLD algorithm functions as a filter, which incorporates a set of ab-
solute and relative (channel 7 to channel 6) pulse amplitude threshold
criteria, to identify the pixel numbers of all Xenon searchlight pulse
signatures (if any) in the Landsat imagery data passed through the
filter. The channel 7 pulse amplitude threshold was then varied to
determine the minimum channel 7 pulse amplitude required to assure a
high degree of discrimination against the variety of solar radiation
pulse signatures found in the Landsat imagery data. In this way it was
found that a minimum channel 7 pulse threshold of seven percent (of the
full scale) could be adopted as a guide for selecting a prototype Xenon
searchlight that would be suitable for an EOS SLS.

Based on this result it was concluded that a commercially avail-
able Xenon searchlight (trade named XENOSPOT) would be suitable for an
EOS SLS. In brief, it was found that the Xenospot has the theoretical
capacity to generate a pulse amplitude of between 30 and 46 percent
of the full scale range for the near IR channel of the MSS planned for
the EOS spacecraft. The 30 percent value was derived from the conser-
vative theoretical pulse amplitude model and actual measurements of the
minimum calibration radiation intensity over a 1.5 by 6.0 degree rect-
angular cone within the center portion of a slightly defocused beam.

These results were obtained however with a non optimal beam
spread lens, and the manufacturer is confident that an optimally de-
signed lens could boost the minimum intensity in such a cone by as
much as 54 percent. The 46 percent estimate for the minimum pulse am-
plitude over such a cone is therefore regarded as a realistic design
goal estimate for the near IR pulse amplitude of an EOS SLS employing a
Xenospot searchlight. The delivery price for a Xenospot, including its
power supply and an optimally designed lens, would be approximately 7K
in lots of 100 or more.

The 1.5 by 6.0 degree cone size specification was adopted, in
the above considerations, in order to provide a generous allowance for
pointing offsets that can result from the anticipated cyclic deviations
in the attitude and the orbital ephemeris of the EOS spacecraft.

Section 3 of this report attempts to provide a relatively clear picture of the overall magnitude of a searchlight landmark utilization program in terms of the major tasks that would have to be considered in connection with the implementation and operation of a national grid of searchlight landmark stations (SLSs). The theory of operation and the basic types of components that might be incorporated in one possible configuration of an SLS are briefly described in order to provide a preliminary conceptual basis for the generation of an RFQ for (1) a detailed engineering design, (2) a realistic cost estimate for the construction and testing of a prototype SLS, and (3) a realistic cost estimate for the fabrication, installation, and check out of 100 SLSs throughout the U.S.. Additional tasks relating to SLS site selection, land leasing, and surveying are also discussed.

SECTION 2

SELECTION AND TESTING OF AN OPTIMAL

ARTIFICIAL LANDMARK FOR AN EOS SPACECRAFT

2.1   MSS SIGNATURE CHARACTERISTICS OF BEACON TYPE ARTIFICIAL LANDMARKS

2.1.1   Introduction

This section reviews the general operation of a multispectral scanner (MSS) and the historically anticipated pulse signature characteristics of beacon type artificial landmarks which suggested their ideal suitability for the kind of landmark utilization program described in Section 1.1.1. An understanding of the geometrical relationships and imaging characteristics described here will be assumed in the later sections dealing with the theoretical pulse amplitude model, the searchlight experiment results, and the discussions in Appendix A concerning the statistical probability of signature degradation due to detector sharing and data sampling. The imaging of extended sources (earth scenes) and the operation of a Landsat MSS responsible for the ordinary MSS scan signal is described first and followed by a description of the imaging of a beacon landmark., which results in the superposition of a pulse signature on the ordinary MSS scan signal.

2.1.2   Extended Source Imaging Characteristics

The various ray paths associated with the imaging of extended and point sources in a multispectral scanner (MSS) are depicted by the simplified (heuristic) drawings in Figure 2-1.

The Instantaneous Field of View or IFOV of an MSS is defined as the divergence angle of the individual detectors (or light pipes) located in the image plane of the MSS. The IFOV is therefore denoted by the subscripted angle parameter θ_D (Theta detector). The solid angle (or solid field of view) defined by each detector is then denoted by the corresponding solid angle parameter $\Omega_D = \theta_D^2$. At each instant of time a given MSS detector views a square element of the earth's surface denoted by the area parameter $A_{DG} = R^2 \Omega_D$, where R is the instantaneous altitude of the spacecraft. A given detector is therefore illuminated by only that portion of the scattered solar radiation from A_{DG} which is propagating and converging toward the MSS scan mirror within the directions defined by the viewing cone Ω_D (as indicated by the

(b)

P — Plane Parallel Radiation From Point Source
E — Convergent Radiation From Extended Source

(a)
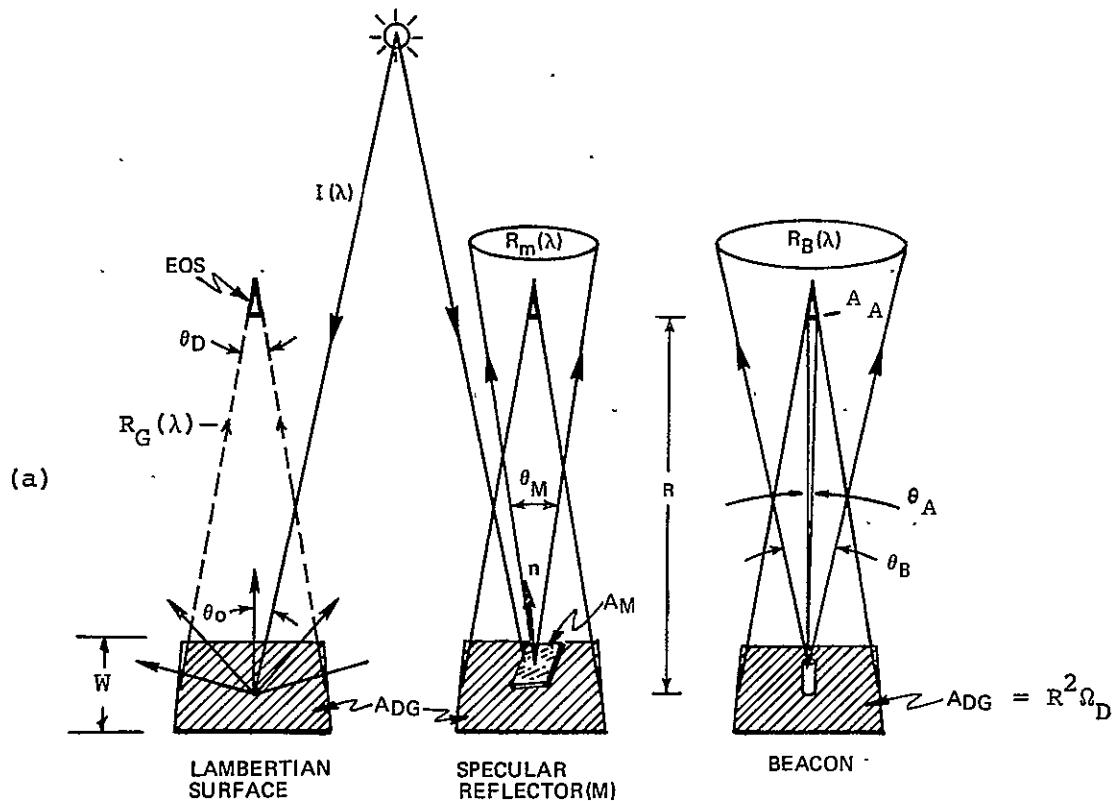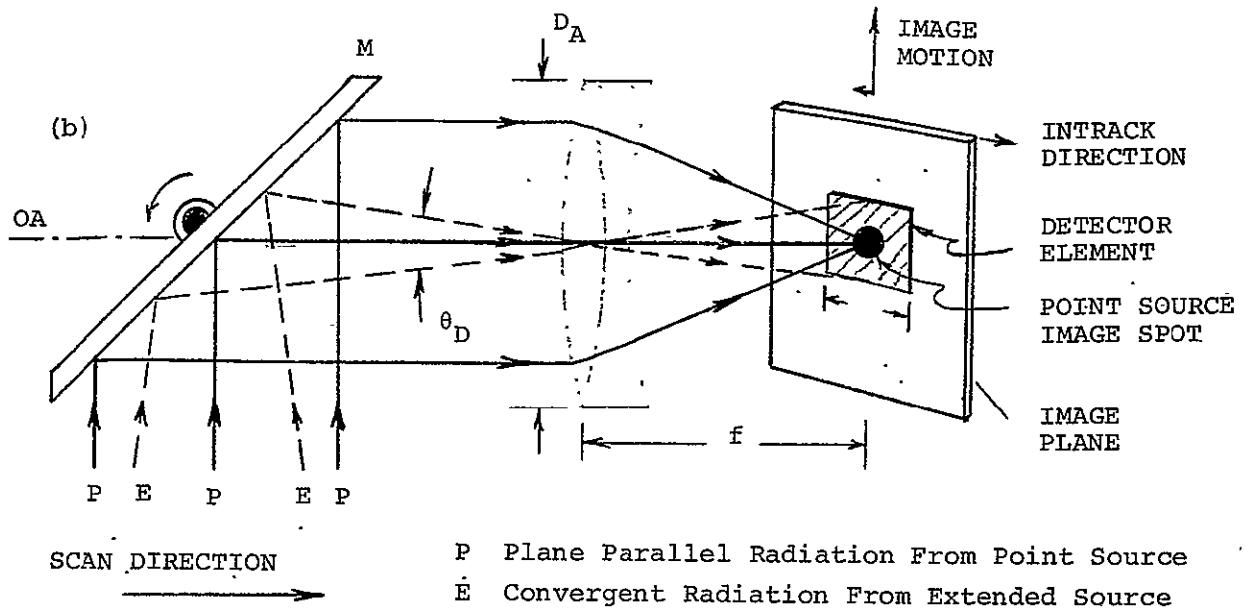
FIGURE 2-1   MSS IMAGING GEOMETRY FOR
EXTENDED AND POINT SOURCES

dashed lines (E)). The particular surface area (AD_G) being viewed by a given detector in the image plane, at a given instant in time, is therefore determined by the instantaneous orbital position and attitude of the MSS, and by the instantaneous orientation of the scanning mirror (M) relative to the optic axis (OA). For the Landsat MSS, R (mean) = .916 x 10^6 meters and θ_D = 86 x 10^{-6} radians. Thus, Ω_D = 7.4 x 10^{-9} steradians, and the instantaneous ground resolution width W = $R\theta_D$ is equal to about 79 meters.

The recorded portion of the electronic output from the MSS detectors is synchronized with that half of the scan mirror oscillation corresponding to an eastward sweep of the earth's surface (NW to SE in the crosstrack direction), and the size of the strip thus scanned by each detector (in the Landsat MSS) is approximately 79 meters by 185 km (100 nm). The varying illumination experienced by each MSS detector during a scan therefore generates an analog scan signal which is then amplified and digitized and telemetered to earth, where it is processed and used to generate a photgraphic scan line in the resultant imagery products. A representative analog scan signal from an MSS detector is illustrated in Figure 2-2 (following a calibration pulse), and the complete detector array for the Landsat MSS is illustrated in Figure 2-3.[4]

In reference to Figure 2-3, it is noted that the Landsat MSS employs six contiguous detectors in the intrack direction, which are split up or divided spectrally into four wavelength channels covering the following spectral ranges (in microns):

$$\lambda_1 = 0.55 \ (\pm \ .05) \tag{2-1}$$
$$\lambda_2 = 0.65 \ (\pm \ .05)$$
$$\lambda_3 = 0.75 \ (\pm \ .05)$$
$$\lambda_4 = 0.95 \ (\pm \ .15)$$

Each oscillation of the scan mirror therefore results in the generation of six contiguous IFOV scan signals in each of the four wavelength channels, or a total of 24 spatially and spectrally independent scan signals per mirror scan. The motion of the scan mirror therefore

CALIBRATION PULSE

BEACON LANDMARK PULSE

SCAN SIGNAL (% FS)

100

40

0

T_s

DT

TIME
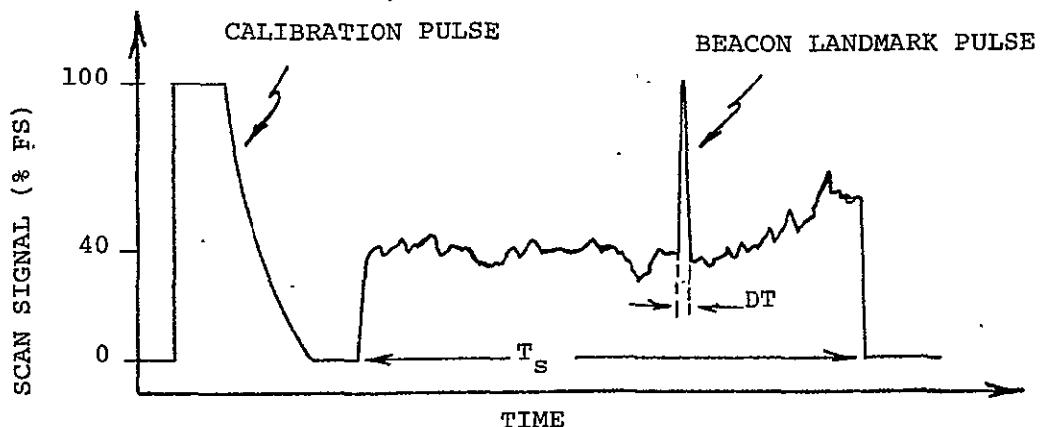
FIGURE 2-2   Representative MSS Scan Signal With
Beacon Landmark Signature

IMAGE MOTION

ROW λ_4 λ_3 λ_2 λ_1

6   1   2   13   14

5   3   4   15   16   SCAN DIRECTION
                                             (NW ——— SE)

4   5   6   17   18

3   7   8   L   19   20

2   9   10   21   22   SPACECRAFT MOTION
                                             (NE ——— SW)

1   11   12   23   24

TIME

DATA SAMPLING PULSES FOR ROW 5
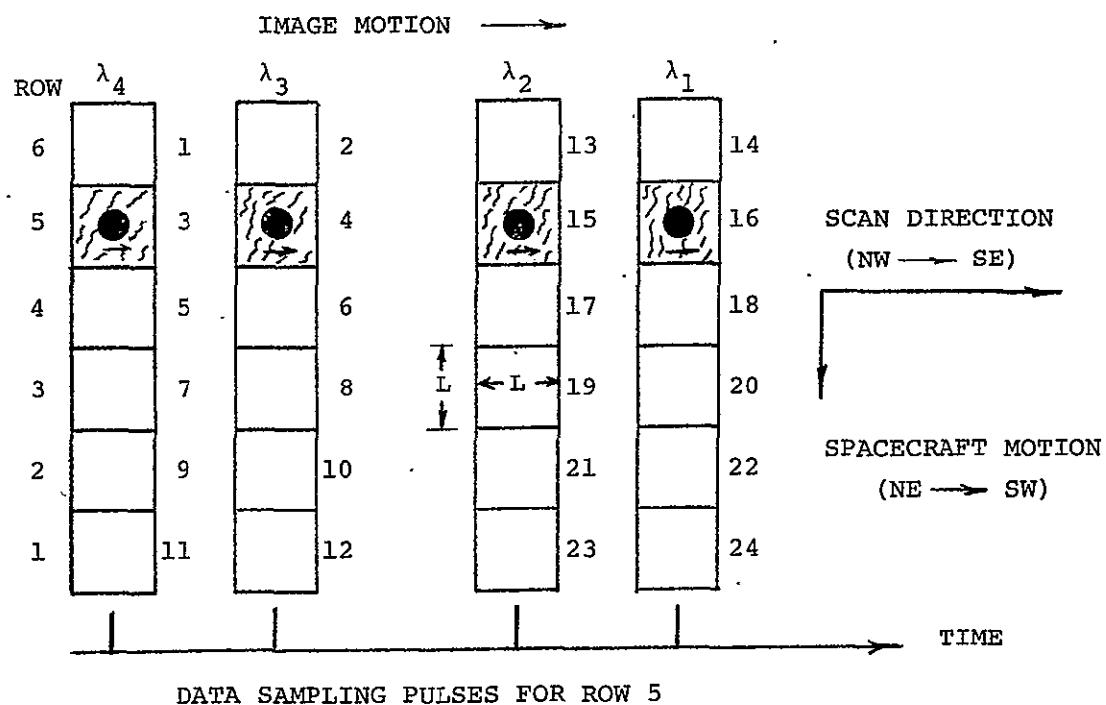
FIGURE 2-3   Landsat MSS Detector Array Showing
Sequential Positions and Sampling of
Beacon Landmark Image

causes the total radiometric image from a 0.468 by 185 km (wide) strip
to translate across the entire MSS image plane in the direction shown
in Figure 2-1 (b) and 2-3. The scene illumination recorded in the
successive wavelength channels (4 to 1) therefore corresponds to the
illumination conditions at the scene for successively greater points in
time.

2.1.3   Beacon Landmark Imaging Characteristics

The radiation arriving at the aperture of an MSS from a man-
made beacon or solar reflector (as illustrated in Figure 2-1) can be
described as plane parallel radiation from a distant point source. The
ray paths of such radiation are indicated by the solid lines (P). In a
perfectly constructed optical instrument, the image of the source (point)
would be transformed into a series of concentric rings about a central
spot (called an Airy disc) containing about 85 percent of the radiant
power passing through the aperture lens. The theoretical diameter of
this central image spot is given by the well known formula

$$D_S' = \frac{2.44\ \lambda\ f}{D_A} \qquad (2\text{-}2)$$

where λ is the wavelength of the radiation being considered; f is the
focal length of the imaging system; and D_A is the diameter of the aper-
ture lens. In most practical optical instruments however, the image of
a point source (or plane parallel radiation) is diffused throughout a
larger spot (sometimes referred to as a blur circle) due to the combined
effects of diffraction, figure imperfections, and misalignment of the
optical elements. The diameter (D_S) of the blur circle for the Landsat
MSS is approximately three times the diffraction value (D_S') expressed
by Equation 2-2[5]. The ratio of the blur circle diamter (D_S) to the
detector width $(L = f\ \theta_D)$ for the Landsat MSS can be estimated from the
formula

$$\alpha \equiv \frac{D_S}{L} = \frac{7.62\lambda}{D_A\ \theta_D} \qquad (2\text{-}3)$$

Using the values of D_A and θ_D for the Landsat MSS (.23 meters and 86 micro radians) gives the following values of α for each of the MSS channels:

$$\alpha_1 = 0.21 \qquad\qquad (2\text{-}4)$$
$$\alpha_2 = 0.25$$
$$\alpha_3 = 0.29$$
$$\alpha_4 = 0.37$$

2.1.3.1 Imaging Constraints

The spot image of a landmark beacon is depicted in Figure 2-1, (b) at an instant when the beacon landmark is located directly in the center of the viewing cone Ω_D (and the instantaneous surface area A_{DG}), and when the image spot is, accordingly, positioned at the center of the detector. The observation of a point source of radiation, in this sense, is accomplished by means of the small fraction of its total radiation output which is propagating in the direction of the spacecraft at the instant that the source point (or landmark) comes within the IFOV of a given detector. The radiation in all other directions is totally wasted at this point since it in no way contributes to the radiant power impinging on the scan mirror and thus the image spot at the detector. A certain minimal amount of beam divergence and thus wasted power would necessarily be required however in order to allow for the unavoidable uncertainties in the angular position and/or the attitude of the spacecraft relative to the beacon landmark at the instant of sighting.

Thus for all practical purposes, the point source radiation impinging on the MSS, as indicated by the solid rays labeled (P) in Figure 2-1 (b), may be viewed as being contained within an extremely narrow and directionally fixed beam, with a full cone angle (D_A/R) on the order of 1.5×10^{-5} degrees. These remarks are made only to clarify a potential source of misunderstanding. In particular, it is noted that a beacon landmark cannot be repeatedly imaged or observed, on successive scans, unless the point on the earth's surface where it is located is repeatedly imaged on successive scans, and then only if the spacecraft is still within the macroscopic angular limits of the beacon.

2.1.3.2 Pulse Amplitude Considerations

A pulse like signature for a beacon landmark would logically be expected to occur in the output of each MSS channel as the scanning mirror translates the corresponding image spot over the surfaces of the respective viewing detectors in the manner indicated in Figures 2-2 and 2-3. The amplitude of the pulse (in the ith wavelength channel) should then be directly proportional to the maximum amount of beacon power $[P_{BD}(\lambda_i)]$ which is thereby superposed on the respective viewing detector. This power can be expressed quite simply in terms of the aperture area $(A_A = \Pi D_A^2/4)$ and the beacon radiation intensity $I(\lambda_i)$ at the aperture. The value of $I(\lambda_i)$ represents the average number of watts per square meter and per unit wavelength interval within the spectral bandwidth of the ith channel.

Thus,

$$P_{BD}(\lambda_i) \quad = \quad k_i I(\lambda_i) A_A \ BW_i , \qquad\qquad (2-5)$$

where k_i is the MSS optical transmission factor for the center wavelength λ_i, and BW_i is the corresponding bandwidth of either the radiation per se or the MSS channel filter, whichever is less.

It is helpful to compare this expression with a similar expression for the background signal or extended source power $[P_{ED}(\lambda_i,t)]$ which illuminates the full surface of the detector.

$$P_{ED}(\lambda_i,t) \quad = k_i R_G(\lambda_i,t) \Omega_D A_A \ BW_i \qquad\qquad (2-6)$$

Here, $R_G(\lambda_i,t)$ is the average instantaneous radiance over the instantaneous viewing surface A_{DG}, but as seen at the MSS aperture (that is, after being attenuated by the atmosphere). The value of $R_G(\lambda_i,t)$ therefore represents the intensity per unit solid angle and per unit wavelength interval (watts/(m^2 -μ -str)) within the spectral bandwidth of the ith channel. The product of $R_G(\lambda_i,t)$ and Ω_D may therefore be regarded as an "effective" average intensity $I_E(\lambda_i,t)$ over the aperture

which is analogous to $I(\lambda_i)$ except for the fact that it is not plane
parallel and it serves therefore to illuminate the full surface of
the detector element.

The calibrated magnitude of $R_G(\lambda_i)$ associated with the maximum
(full range or full scale) output for a given MSS channel is a known
parameter of an MSS which is here denoted by $R_{GM}(\lambda_i)$. Substituting
$R_{GM}(\lambda_i)$ for $R_G(\lambda_i,t)$ in Equation 2-6 gives the related expression
for the detector illumination power $[P_{EDM}(\lambda_i)]$ associated with a full
scale response in the ith channel of an MSS.

$$P_{EDM}(\lambda_i) = k_i \ R_{GM}(\lambda_i) \ \Omega_D A_A \ BW_i \qquad (2\text{-}7)$$

The ratios $(100 \ P_{ED}/P_{EDM})$ and $(100 \ P_{BD}/P_{EDM})$ can thus be conveniently
formed and used to describe the ordinary MSS scan signal level $SS(\lambda_i,t)$
and the superposed beacon landmark pulse amplitude $BPA(\lambda_i)$ as a fract-
ional percent of the full scale outputs for the detectors in the ith
wavelength channel.

Thus,
$$SS(\lambda_i t) = 100 \ R_G(\lambda_i,t)/R_{GM}(\lambda_i) \ \%, \qquad (2\text{-}8)$$

and
$$BPA(\lambda_i) = \frac{100 \ I(\lambda_i)}{\Omega_D R_{GM}(\lambda_i)} \ \%. \qquad (2\text{-}9)$$

The pulse amplitude of a beacon landmark signature can therefore be ex-
pected to be directly proportional to the radiation intensity of the
beacon $[I(\lambda_i)]$ and inversely proportional to either the solid IFOV
(Ω_D) of the MSS (or the square of its linear IFOV (θ_D). The radiation
intensity $I^*(\lambda_i)$ required to satisfy a given minimum pulse amplitude
or design specification $BPA^*(\lambda_i)$ is therefore directly proportional to
Ω_D and given by the expression:

$$I^*(\lambda_i) = \Omega_D \ R_{GM} \ (\lambda_i) \ BPA^*(\lambda_i)/100 \qquad (2\text{-}10)$$
$$= .5 \ \Omega_D \ R_{GM}(\lambda_i) \ (\text{for } BPA^* = 50\%)$$

Equations 2-9 and 2-10 are utilized and/or referred to extensively in
the remaining subsections (2.2 through 2.6).

2.1.3.3 Pulse Width ·Considerations

The width of a beacon landmark pulse affects the accuracy with which the geographical position of the landmark can be established in the MSS data stream, and it provides a useful parameter for the development of an appropriate detection scheme. The theoretically expected pulse width (at half amplitude) is discussed accordingly in terms of both an analog or continuous time base (seconds) and a quantized time base associated with a digital picture element (pixel).

The theoretical width of a beacon landmark pulse (at half amplitude) should be very nearly equal to the so called Dwell Time for a detector (DT), which is the time required for a point in the image to move across the surface of a detector, or the time for the IFOV to sweep across a given point on the earth's surface. Identifying T_S as the time interval associated with the active (forward) portion of each scan, and θ_S as the total angle scanned relative to the spacecraft, permits the dwell time (DT) to be expressed by the simple formula:

$$DT = (\theta_D/\theta_S)\ T_S. \qquad (2-11)$$

From ·Figure 2-4 it is clear that DT represents the time interval during which one half or more of the image spot, and thus the image power P_{BD} (λ_i), remains on a given detector. The detector dwell time should therefore provide a reasonably good estimate for the half amplitude analog pulse width provided only that the detector-amplifier response time constant is significantly less than DT. For the Landsat MSS, $\theta_S = 0.2$ radians (11.56 degrees), $\theta_D = 86 \times 10^{-6}$ radians, and $T_S = .0315$ seconds. The corresponding beacon landmark pulse width, with respect to the analog output of the Landsat MSS,· would therefore be expected to be about 13.5 microseconds (at half ·amplitude). The position uncertainties associated with the analog and digital signatures of beacon landmarks are discussed in Section 2.1.4.

The digital signature of a beacon landmark, as it would appear in the telemetered data stream, can be predicted from the following considerations relating to the operation of the Landsat MSS. The 24 detector array in the Landsat MSS, as shown in Figure 2-3, is sampled in the sequence indicated by the numbers to the right of each detector during a total sampling period denoted by the parameter T_{SR} which is approximately 9.95 microseconds. The relatively instantaneous sampling duration for each detector is therefore about 0.41 microseconds and each and every detector is therefore repeatedly sampled once every T_{SR} seconds. The spacing of the channel detectors in the scan direction is chosen accordingly to insure that a given scene moving across the image plane will be sampled in the same position relative to the detectors in the successive wavelength channels.

The time interval (T_{SR}) between successive samples of a given detector determines the distance (ΔX) that a given point in the imagery moves within or relative to a detector between successive samples. This distance can be expressed as $\Delta X = gL$, where $g \equiv T_{SR}/DT$ defines the fraction of the dwell time represented by sampling period. Thus, in the case of the Landsat MSS, DT = 13.5 μs and g ≈ 0.74, so that $\Delta X = 0.74L$. (The imagery in this case is said to be over sampled, with the IFOV for each sample or pixel element containing about 26 percent of the IFOV from the previous sample or pixel element).

For the purpose of analyzing the digital pulse signature of a beacon landmark, it is convenient to parameterize the fraction of the image spot falling on a given detector, during the jth sample, by the linear fraction $FD_j = X_j/D_S$ of its diameter (D_S) which overlaps a given detector relative to either its left or right edge. It is further convenient to use the subscript value j = 1 to denote the first non zero value FD_j, and the parameter $\alpha \equiv D_S/L \leq 1.0$, as before, to denote the relative spot diameter (in units of the detector width). With these definitions the sum of the first two image fractions takes the form:

$$FD_1 + FD_2 = 1 + \frac{(1-g)}{\alpha} \tag{2-12}$$

Thus, for the case of perfect sampling (neither over nor under sampling), $g = 1$, and there can only be (at most) two non zero samples of the spot image which are then consistent with the restriction $FD_2 = 1 - FD_1$. The maximum value of FD_1 is just $g/\alpha = 1/\alpha$, or unity, whichever is largest. Since the values of $\alpha_i = \alpha(\lambda_i)$, from equations 2-4, range between 0.2 and 0.4, it is clear that the perfect sampling of a spot image would generally produce two non zero samples of the spot consistent with the relation $FD_2 = 1 - FD_1$ where the value of FD_1 (and thus FD_2 also) is randomly distributed over the interval from zero to unity.

.However, for the over sampling case (where $g = .74$) we see that the sum of FD_1 and FD_2,

$$FD_1 + FD_2 = 1 + \frac{.26}{\alpha} \qquad (2-13)$$

will generally be greater than one, and for the smallest spot size, $\alpha_1 = 0.21$, would even be greater than two, implying that the full spot image and pulse amplitude could be sampled twice. These considerations are illustrated in Figure 2-4 for three spot sizes corresponding to $\alpha = 1$, 1/3, and 1/5, and for a slightly smaller sample step size $\Delta X_s = gL = 0.6L$. The ordinate scale defines the fraction of the spot area associated with a given linear diameter fraction overlap ($FD_j = X_j/D_s$), where:

$$f_j(A_j) = \frac{1}{2} + \frac{1}{\pi} [A_j \sqrt{1 - A_j^2} + \sin^{-1}(A_j)] \qquad (2-14)$$

and $\qquad A_j \equiv 2FD_j - 1$

Thus to the extent that the image spot intensity is uniform over the spot area $A_s = \pi D_s^2/4$, the spot area fraction $f_j(FD_j)$ also represents the fraction of the maximum pulse amplitude BPA (described in Section 2.1.3.2) that would then be recorded in the jth sample or pixel. The beacon landmark position uncertainties associated with the size of the IFOV and the digital sampling are discussed next.
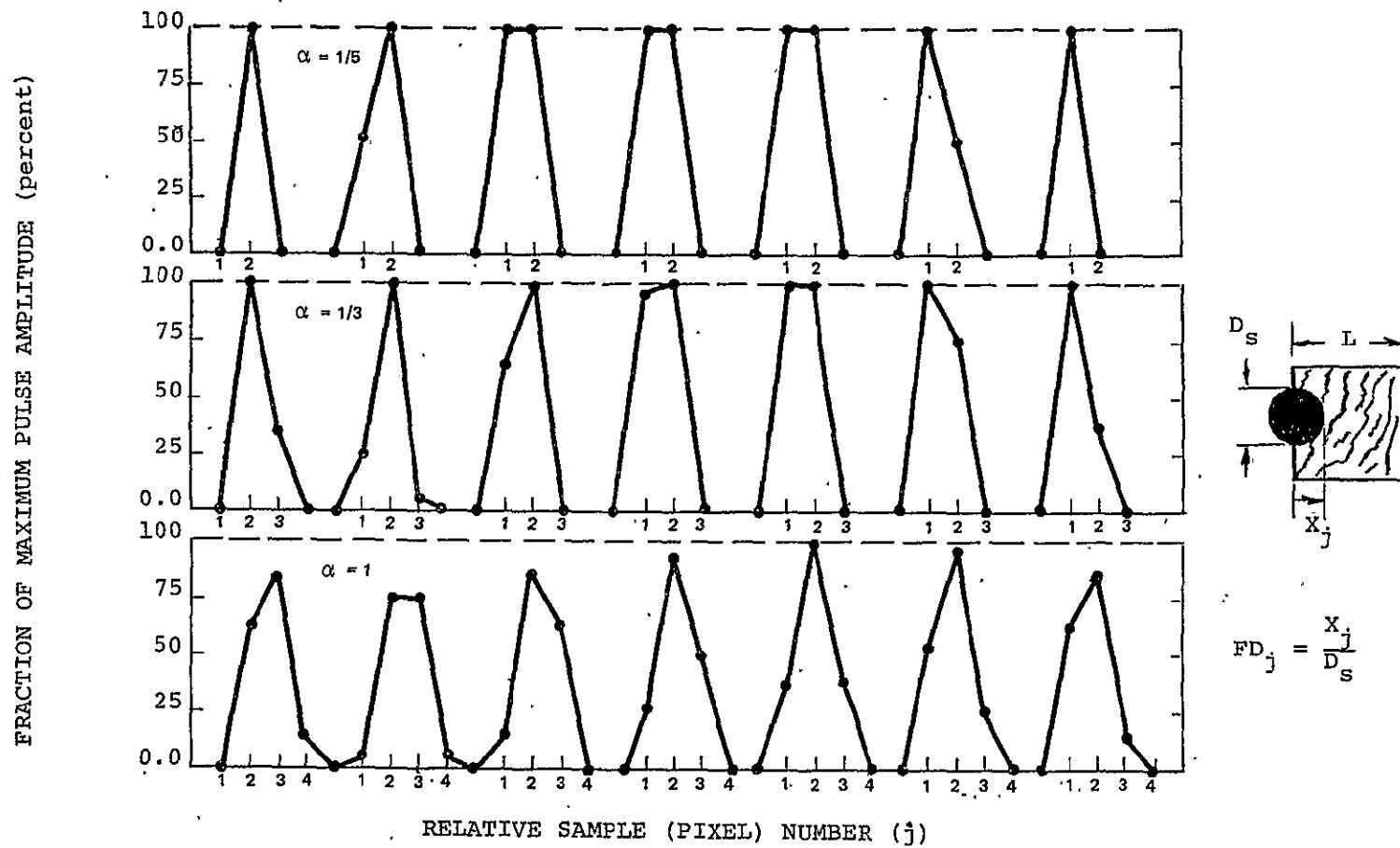
FIGURE 2-4   Efficiency and Shapes of Beacon Landmark Pulse Signatures for a
Uniform Distribution of Equally Probable Initial Conditions.
Shown for 3 Fractional Spot Diameters ($\alpha = D_s/L$) and a Sampling
Step Size $\Delta X = 0.60L$.

2.1.4　Beacon Landmark Position Accuracy

Measurement data relating to the orbit ephemeris and the attitude of the spacecraft, as well as the operation of the MSS, can be used to compute the surface coordinates corresponding to the center of the instantaneous ground area associated with a given detector in the MSS at a given instant of time. With reference to one set of the channel detectors shown in Figure 2-3 (the λ_4 set for example) we denote the relative locations of a given intrack detector by means of a row subscript R. The computed longitude and latitude associated with the center of the IFOV for the detector D_{4R}, at the time of its jth sample, are then denoted by the parameters $\phi_{4R}^C(j)$ and $\psi_{4R}^C(j)$ respectively, and the corresponding true values of the longitude and latitude are denoted by the parameters $\phi_{4R}^T(j)$ and $\psi_{4R}^T(j)$. The computation errors associated with the determination of the longitude and latitude for the pixel $P_{4R}(j)$ may therefore be denoted symbolically as $\Delta\phi_{4R}^C = \phi_{4R}^C(j) - \phi_{4R}^T(j)$ and $\Delta\psi_{4R}^C(j) = \psi_{4R}^C(j) - \psi_{4R}^T(j)$.

For the heuristic case of an exact polar orbit, the detector width (L), and thus the instantaneous ground resolution distance (W), serve to identify a specific longitude increment $\Delta\phi_{4R}(j)$ in the scan or crosstrack direction, and a specific latitude increment $\Delta\psi_{4R}(j)$ in the intract direction. Thus if the imagery of a specific (kth landmark) point on the earth's surface, with coordinates ϕ_K^T and ψ_K^T, is known to have been somewhere within the detector's surface area $S_{4R} = L^2$, at the instant of its jth sample, then the longitude and latitude of the center of the corresponding IFOV or the jth picture element can be measured (in the imagery processing) as $\phi_{4R}^M(j) = \phi_K^T$ and $\psi_{4R}^M = \psi_K^T$ to within a maximum uncertainty of $\pm.5\,\Delta\phi_{4R}(j)$ and $\pm.5\Delta\psi_{4R}(j)$ in the longitude and latitude.

In general, however, it should be possible to make use of the finite spot size to determine the position of the image spot, relative to the observing detector, to an accuracy of better than $\pm$ 0.5L. For example, suppose the maximum pulse amplitude BPA is such that the overlapping of the spot diameter on a given detection by a fraction FD_M could be readily observed as a partial pulse (f_MBPA) against the background signal. Then one of two cases would then prevail with regard to

the position of the image spot in the intrack direction. In one case, no portion of the pulse signature would be observed in the data from either of the adjacent intrack detectors $D_{4,R-1}$ and $D_{4,R+1}$, and one could conclude that the center of the spot is therefore at least $(.5-FD_M)D_S$ away from either of the intrack edges of D_{4R}. The intrack or latitude uncertainty in this case would be reduced to $\pm.5L[1-2\alpha(.5-FD_M)]$. Thus if $FD_M = 0.3$, this uncertainty becomes $\pm.5L(1-.4\alpha)$ or $\pm.4L$ and $\pm.3L$ for α equal to 0.5 and 1.0 respectively.

In the other intrack case, the image spot would be overlapping an adjacent detector (say $D_{4,R+1}$) by at least $FD_M D_S$ but by no more than $.5D_S$, since that would just reverse the respective roles of the primary and adjacent detectors. In this case one would know that the center of the spot is within a distance of $(.5-FD_M)\cdot\alpha L$ of the edge of the primary detector, or just $0.2\alpha L$ (for $FD_M = 0.3$). This suggests that the intrack or latitudinal position uncertainty can be minimized the most in the cases where the beacon landmark image is shared by two intrack detectors.

The same types of arguments can be applied to the crosstrack or longitudinal uncertainties. Here, one would make use of the relative pulse amplitudes, making up the pulse signature profile or shape, to narrow down the position of the image spot relative to the detector at the time corresponding a particular sample, called the primary_sample. The statistics associated the probability of intrack detector sharing are discussed in Appendix A.

2.2 BEACON LANDMARK TRADE STUDY

The objective of this task was to determine the relative merits, with respect to practicality and cost, of various candidate types of beacons for an EOS beacon landmark station. The specific types of beacons considered included solar radiation from specular reflectors, lasers, and commercial searchlights. As a basis for comparison, the radiant power required from a given type of beacon was established in accordance with the following criteria. The radiation intensity produced at an altitude of 700 km by a beacon should be sufficient to generate a pulse amplitude signature of at least 50 percent of the full

scale range in one spectral channel of an EOS MSS having an instantaneous field of view (IFOV) of 43 microradians or less. The radiant power criterion then follows from the requirement that this minimum intensity criterion must be satisfied over a rectangular conic section or beam spread covering 1.5 by 6.0 degrees. These criteria served to establish the minimum total radiant power required from a beacon and thus, through other considerations relating to performance and efficiency, the size and cost of a beacon that would be suitable for an EOS landmark station.

The 43 microradian IFOV anticipated for the EOS MSS is one half of that in the Landsat MSS. The radiation intensity required, in accordance with Eq. 2-10, is therefore one fourth of that which would be required for a Landsat beacon landmark. The fact that the intensity is specified at a lower mean altitude, 700 km versus 916, means that the output radiation intensity (at a given reference distance) is decreased again by a factor of $(700/916)^2 = 0.58$. Thus the near field beacon intensity required for an EOS beacon landmark is only about 15 per cent of that which would be required for a Landsat beacon landmark.

Because of the seemingly obvious economic and/or spectral attributes associated with solar reflectors and lasers, the feasibility and practicality of using these types of sources for a fixed beacon landmark were investigated first, with the following results. The practicality of using either visible or IR lasers as sources for a fixed beacon landmark was found to be severely limited by either their intrinsically low output powers or by their relatively low efficiences for converting electrical power into useful radiant power. In general, one pays a very high price per watt of radiant power for the highly monochromatic and collimated features of a laser beam, neither of which is actually required or even desired for a fixed beacon landmark source. The practicality of using a curved solar reflector as a source for a fixed beam artificial landmark was found to be severely limited by the uncommonly large surface that would be required to accommodate seasonal changes in the solar zenith angle. Smaller reflector surfaces could be utilized, but only at the expense of a two degree of freedom sun tracking and pointing system. Thus, the particular advantages that lasers and solar reflectors would otherwise offer, if the requirements called

for a monochromatic and/or highly collimated beacon, turned out to be of little value for meeting the cost requirements of a fixed beacon landmark. The size and pointing requirements for a Mirror Landmark. Station or MLS are derived and discussed in detail in Appenxdix C.

Subsequent investigations into the efficiency and maximum radiant power obtainable with conventional sources of broad band radiation revealed some rather surprising facts or particular value for the selection of a cost effective landmark beacon. Throughout the past decade· or so a significant technological advancement has been achieved in the area of concentrated high intensity light sources, primarily through the development of the xenon short-arc discharge projection lamp. Featuring an operating efficiency of nearly 50%, a very minimum of maintenance over a long life (approximately 1000 hours)., and push button start up, xenon lamps can provide up to 10,000 watts of radiant power with a spectral distribution closely matching that of the sun. These desirable attributes of the xenon short-arc lamp account for the appearance, over the past decade, of many new types of optical equipment including new and compact types of military and commercial searchlights, signaling beacons, solar simulators, and wide screen projectors.[6-10] Because of these factors it was determined (in Section 2.6) that a commercially available xenon searchlight, rated at 4 kilowatts (d.c. input power), should adequately satisfy the intensity requirements for an EOS landmark beacon, in the most practical and cost effective manner. The approximate cost of these xenon searchlights, including a power supply for operation from a 220 volt, 60 cycle single phase line, and a power relay or line contactor for remote control switching operations, is currently estimated at $7,000.00 (in lots of 100).

2.3   THEORETICAL SIGNATURE CHARACTERISTICS OF XENON SEARCHLIGHT
        LANDMARKS

This section describes the formulation of a theoretical model for predicting the maximum amplitude of the pulse that could be generated in the ith wavelength channel of an orbiting multispectral scanner (MSS) due to the effective point source radiation from an xenon searchlight beacon. The phrase "maximum amplitude" refers to the pulse amplitude that would be expected for the case of a standard "clear" atmos-

REPRODUCIBILITY OF THE
ORIGINAL PAGE IS POOR

phere and the case where the image spot falls entirely within the in-track dimension (L) of one row of the intrack field detectors (as illustrated in Figure 2-3). Under these conditions, the beacon pulse amplitude

$$BPA(\lambda_i) = \frac{100 I(\lambda_i)}{\Omega_D R_{GM}(\lambda_i)} \quad (\%FS) \quad , \qquad (2-15)$$

as developed in Section 2.1.3.2, is expressed most simply as a fractional percent of the full scale intensity range for the ith wavelength channel. The only unknown quantity in the formulation at this point is the beacon radiation intensity $I(\lambda_i)$ at the satellite. The solid field of view of the detectors $(\Omega_D = \theta_D^2)$, and the calibrated radiance $R_{GM}(\lambda_i)$ corresponding to a full scale or maximum scan signal [$SS(\lambda_i)=100\%$], are accurately known parameters for a given MSS. In addition, it is noted that the radiance sensitivity implied by $R_{GM}(\lambda_i)$ is determined primarily by the solar illumination conditions for a particular sun synchronous orbit. The values of $R_{GM}(\lambda_i)$ for the Landsat MSS should therefore be essentially the same for all EOS MSSs which contain the same λ_i channels and are designed for the same sun synchronous orbit and launch time (or window).

The basic objective of the present task is to simply express the beacon intensity at the satellite in terms of (a) its measured intensity $I_O(\lambda_i)$ at some convenient and more or less arbitrary distance R_O from the searchlight, and (b) the average atmospheric optical thickness $OT(\lambda_i)$ over the wavelength range or bandpass associated with the center wavelengths (λ_i) of the MSS channels. For this purpose it is convenient to express the MSS IFOV (θ_D) in units of a reference IFOV $\theta_{DR} = 25$ microradians, by means of the normalized (dimensionless) IFOV parameter $\theta N_D = \theta_D/\theta_{DR}$. With this notation, the theoretical pulse amplitude model can be expressed quite simply as:

$$BPA_i = I_o(\theta) F_i / (\theta N_D)^2 \quad (\%FS), \qquad (2-16)$$

where $I_o(\theta)$ [watts/meter^2] is the measured bolometric (or spectrically integrated) intensity of the beacon at a distance R_O from the searchlight and at an angle θ [degrees] from the central axis of the beacon.

In the case of a rectangular beam, θ would be decomposed into two orthogonal components θ_1 and θ_2. The term F_i contains all the other relevant constants and wavelength dependent parameters in the form:

$$F_i = \frac{100 \, P_{Bi} e^{-OT_i} BW_i (R_o/R)^2}{BR_{GMi} \Omega_{DR}} \qquad [m^2/watt]. \qquad (2\text{-}17)$$

Here, P_{Bi} [1/microns] is the value of the normalized zenon spectral distribution (shown in Figure 2-5); exp ($-OT_i$) is the atmospheric transmission due to a vertical optical thickness OT_i (averaged over BW_i); BW_i [microns] is the MSS bandwidth for the ith channel; R_o [meters] is the calibration distance associated with $I_o(\theta)$; R [meters] is the altitude of the MSS above the earth's surface; BR_{GMi} is the full scale radiance value [watts/m^2-str] integrated (spectrally) over BW_i; and Ω_{DR} [str] is the solid IFOV reference defined by $\theta_{DR}^2 = (25 \times 10^{-6} \text{ radians})^2$ The values of F_i and the corresponding parameters used in its computation are listed in Table 2-1 for a reference calibration distance R_o = 62 meters, and a satellite altitude R = 916 km (which corresponds to the mean altitude of the current Landsat EOS spacecraft). The optical thicknesses (OT_i) were obtained from standard atmospheric data reference tables.[11]

A comparison of the F_i values (hereafter referred to as the channel sensitivity constants) shows that the pulse height sensitivity increases monotonically with increasing wavelength, with a factor of nearly two in evidence between the .95 micron(or near IR channel sensitivity)and the .55 micron channel sensitivity. Inspection of Figure 2-5 shows that the relatively large sensitivity for the near IR channel is due to a pronounced "Xenon Flare" which falls completely within the .3 micron bandpass of the near IR channel of the MSS. The pulse amplitude sensitivity (PAS_i) defined by:

$$PAS_i \equiv \frac{BPA_i}{I_o} = F_i / \theta N_D^2 \qquad (2\text{-}18)$$

gives the pulse amplitude [%FS] per watt/meter^2 of searchlight intensity at the reference calibration distance R_o. For the Landsat MSS
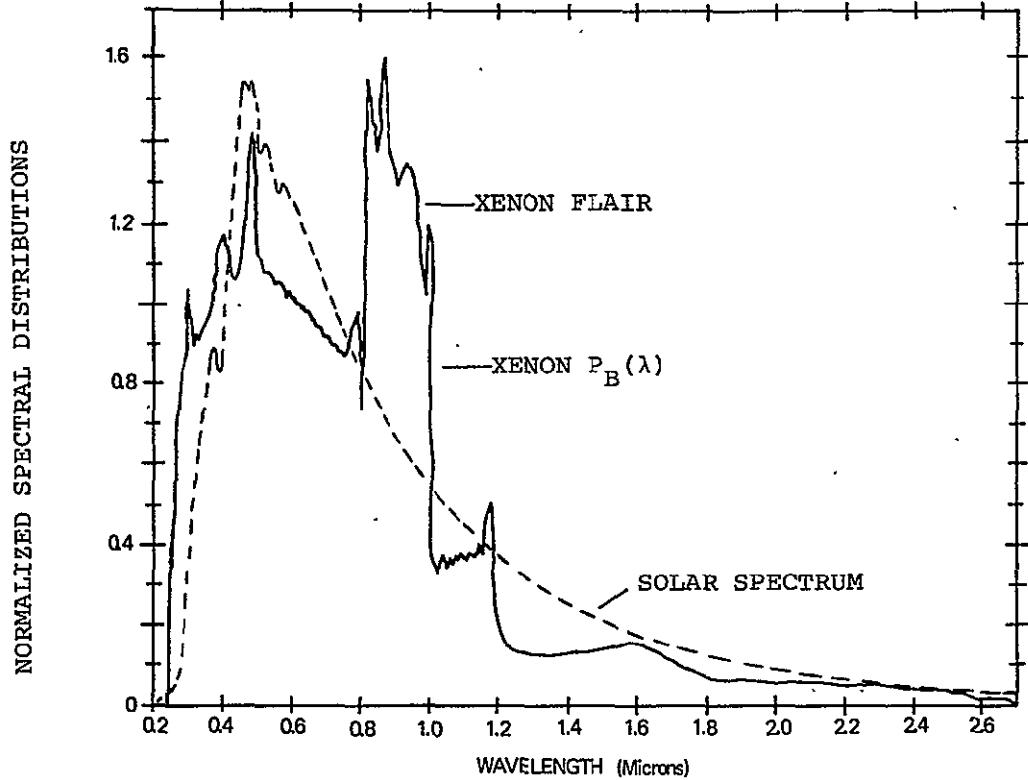
Figure 2-5   Normalized Spectral Distributions for Solar
Radiation (Upper Atmosphere) and Xenon
Searchlight (in the kilowatt range).

TABLE 2-1

VALUES OF PARAMETERS DETERMINING F_i

CHANNEL (i)	BW_i [μ]	λ_i [μ]	P_{Bi} [μ^{-1}]	e^{-OT_i}	BR_{GMi} [W/M^2- str]	F_i [m^2/W]
Eos Landsat						
1 (4)	.1	.55	1.05	.685	24.8	2.118
2 (5)	.1	.65	0.94	.745	20.0	2.558
3 (6)	.1	.75	0.88	.785	17.6	2.867
4 (7)	.3	.95	1.00	.823	46.0	3.920

$R_o = 62$ [m]   R(Landsat) $= 0.916 \times 10^6$ [m] $\dot{\theta}_{DR} = 25 \times 10^{-6}$ [rad]

$$2\dot{I}_o/\theta N_D^2 < BPA_i < 4I_o/\theta N_D^2$$

θ_D = 86 microradians, θN_D = 3.44 and PAS_i = 0.179, 0.216, 0.242, and 0.331 respectively. The inverse (PAS_i^{-1}) = 5.587, 4.630, 4.132 and 3.021 $[w/m^2/(\%FS)]$ then gives the reference beam intensity associated with a theoretical pulse amplitude of one percent in each MSS channel. A pulse amplitude of 50 percent in the near IR channel, for example, would require a beam intensity (I_o) of about 151 watts/meter^2 at a distance of 62 meters (203 feet) from the searchlight. Intensities of this magnitude are readily generated by military (tactical) xenon searchlights like the army's 30 inch (diameter) AN/TVS-3. Figure 2-6 shows a family of curves representing the measured values of $I_o(\theta)$ from such a searchlight for various beam patterns parameterized by the number of turns (T) of a focus control. The data shown corresponds to a d.c. input power level of 15 kilowatts, which represents 75% of the maximum rated input power for an AN/TVS-3. The values of PAS_4^{-1} and PAS_7^{-1} (given above) were used to construct the scales shown in Figure 2-6 for the corresponding theoretical pulse amplitude response in channels 4 and 7 of the Landsat MSS. The experimentally determined accuracy of these scales, and the pulse amplitude model (defined by Equation 2-16) in general, is described in Sections 2.4 and 2.5.

2.4 EXPERIMENTAL SIGNATURE CHARACTERISTICS OF XENON SEARCHLIGHT LANDMARKS

In order to determine the accuracy of the theoretical pulse amplitude model represented by Equation 2-16, a series of AN/TVS-3 searchlight experiments were planned and carried out with NASA's experimental EOS satellites called Landsat 1 and 2. The experiments were conducted with the generous (unfunded) support of the New Hampshire Army National Guard, Searchlight Battery A, of the 197th Field Artillery Group, which furnished all of the AN/TVS-3 searchlights and power supplies and the volunteer support personnel required for their transportation and operation.[2]

2.4.1 Experimental Procedures

The experimental procedures employed in the searchlight landmark experiments and in the retrieval and location of the data are here briefly summarized as follows. Table 2-2 lists the satellite involved in each experiment, the date on which each experiment was conducted,
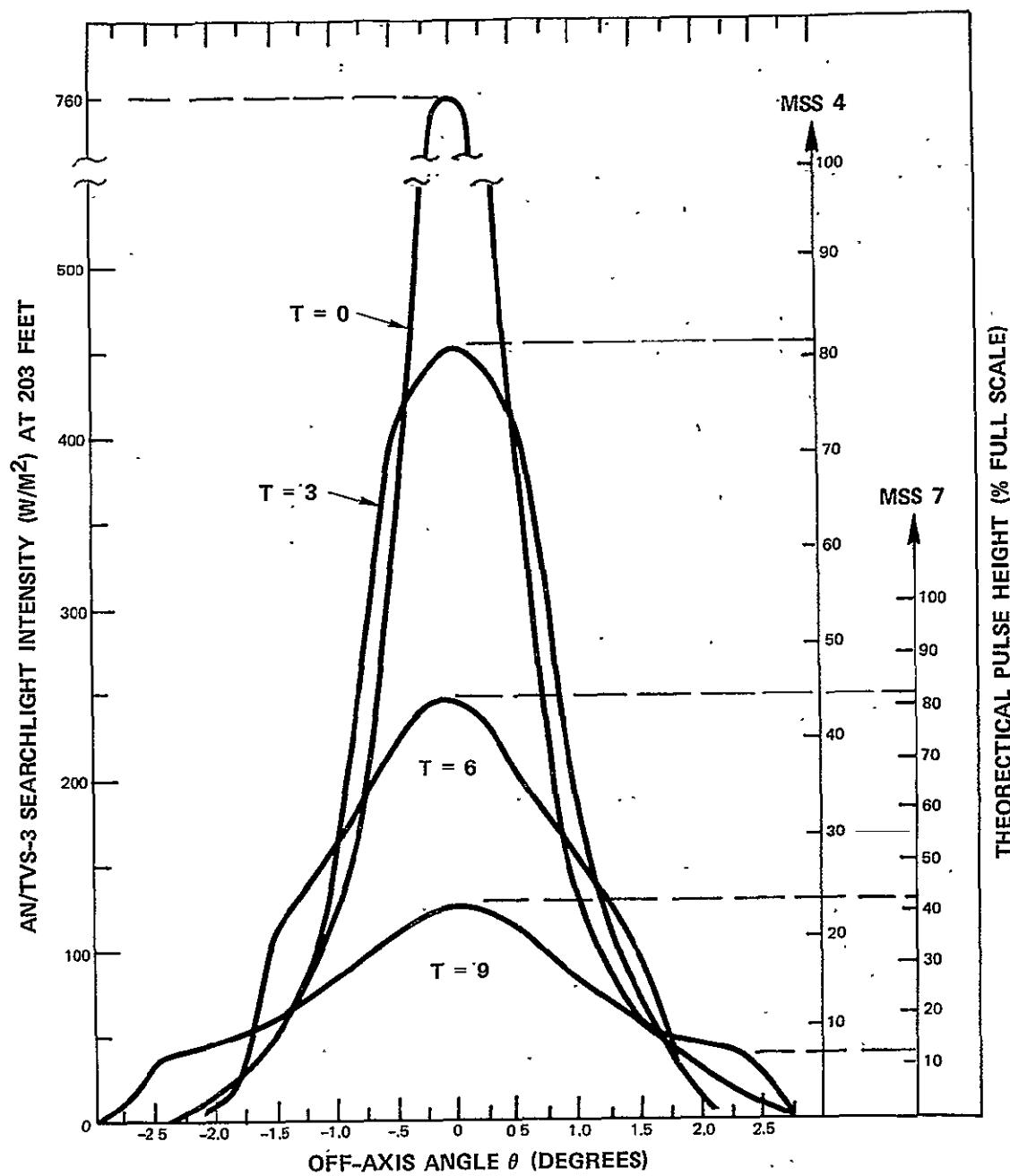
Figure 2-6   AN/TVS-3 INTENSITY PROFILES FOR T TURNS OF FOCUS CONTROL WITH CORRESPONDING PULSE AMPLITUDE SCALES FOR BANDS 4 AND 7 OF THE LANDSAT MSS

TABLE 2-2

LANDSAT/SEARCHLIGHT LANDMARK EXPERIMENT DATA

Landsat Number	Date Mo/Dy/Yr	Test Site Location	Searchlight Data		CCT Data		
			No.	Focus (T)	Scene Number	Tape	Line/Pixel
1	11/03/74	Manchester, NH W. Lon: 71.45° N. Lat: 42.93°	2	3(turns)	1833-14491	2	1652/655
2	02/28/75		1	6	2037-14494	2	1580/261
1	03/09/75	W. Lon: 71.47°	1	6	1959-14435	2	1709/648
2	03/18/75	N. Lat: 43.00°	1	6	2055-14493	2	1587/254
1	05/03/75	Westfield, MA W. Lon: 72.70° N. Lat: 42.16°	3	7	5014-14472	3	489/543
1	05/07/75	Batavia, NY W. Lon: 78.20° N. Lat: 43.02°	3	7	5018-15094	3	1171/456
2	06/26/75	Riverton, UT W. Lon: 111.95° N. Lat: 40.41°	9	9	2155-17310	3	883/416

the location of the test site for each experiment, the number of search-
lights employed in each experiment, and the searchlight beam spread
or profile used in each experiment, as defined by the number of turns
(T) of the beam focus control (see Figure 2-6).

2.4.1.1 Pointing

In each experiment the searchlight(s) were aimed to intercept
the predicted path of the Landsat orbit at right angles to the space-
craft's instantaneous heading vector, which was very nearly equal to
the point of closest approach to the test site. Predicted orbit posi-
tion data furnished by NASA (GSFC) was used to determine the cross-
track surface distance X between the test site and the subsatellite
ground track. The elevation pointing angle (ψ), measured relative to
the local vertical, was then computed from the formula:

$$\sin(\psi) = \frac{X}{R} \ (1 + \frac{X}{R_E}) \ [1 + (\frac{X}{R})^2 \ (1 + (\frac{R}{R_E})]^{-1/2} \qquad (2-19)$$

where R is the estimated altitude of the spacecraft and R_E is the
radius of the earth at the latitude of the test site. The cross-
track surface distance (X) was generally less than 30 km in all of the
experiments and the crosstrack orbit elevation pointing angle (ψ) was
generally between 1 and 2.5 degrees from the local vertical. The uncer-
tainty in the true pointing angle was estimated to be within $\pm$ 0.1
degrees.

2.4.1.2 Firing

Predicted orbit position data, pertaining to the time of the
picture center coordinates for the Landsat scene covering each test
site, was used to estimate the approximate fly-by time (t_o) at which a
test site would be scanned by the Landsat MSS. The values of t_o ranged
from apprximately 10:40 a.m. in Manchester, N.H. to 11:20 a.m. in
Riverton, Utah, and the searchlights were generally turned on from 5 to
10 minutes prior to t_o, and turned off about 5 minutes after t_o.

2.4.1.3 Data Retrieval and Display

Positive transparencies of the approximately 100 by 100 nautical mile scene covering each test site were furnished by NASA (GSFC) along with the corresponding system-corrected digital imagery data. The digital imagery data was formatted on four computer compatible tapes (CCTs) with each tape containing the 25 n.m. wide imagery data from one fourth of the total scan. The complete data array for a scene picture, generated by one of the four wavelength channels, consisted of 2,340 scan lines with approximately 3,240 intensity bits or pixels per scan line (810 pixels per tape). The pulse signature of each searchlight was generally observable in the band 7 (near IR) transparency with the unaided eye; and careful measurements of its position, relative to the top and left edge of the scene, allowed its CCT line number and pixel number to be estimated to within about ± 10 lines and ± 17 pixels. This process narrowed the search field considerably and permitted the actual locations of the signatures to be readily identified in the printed and plotted formats of the CCT data that were generated at CSDL.

The identifying numbers for the Landsat scene and the CCT tape containing the searchlight signatures for each experiment are listed in Table 2-2 along with the approximate scan lines and pixel numbers of the signatures. (The pixel numbers given are referenced to the first pixel in the tape indicated). Table 2-3 provides a sample listing of the MSS data for the first experiment. The pixel intensities are expressed as a percent of the full scale output for the MSS channel, where the symbol $$ is used to denote saturation or 100 percent of full scale. Sample plots of the corresponding data for the target scan line and the scan lines preceding and following it are shown in Figures 2-7 to 2-9. The absence of any noticeable signal sharing by the adjacent intrack detectors (or scan lines) is characteristic of all the data collected from the seven searchlight experiments. This data base which was expanded by the use of multiple searchlights, included 17 spatially distinct signatures, or 68 spatially and spectrally distinct signatures, on a total of 11 scan lines.

TABLE 2-3

LANDSAT 1 MSS PIXEL INTENSITY DATA FROM TAPE 2 OF SCENE 1833-14491

EXPRESSED IN PERCENT OF FULL SCALE OUTPUT (WITH $$ = 100).

SL	B	640					645					650					655					660					665				
1648	4	21	20	21	22	22	20	21	24	24	25	24	22	22	22	24	25	25	30	33	33	33	30	25	22	24	21	20	20	20	20
1648	5	17	14	18	19	19	18	20	22	24	24	20	19	18	20	22	24	22	27	34	35	34	33	24	19	18	17	16	18	19	18
1648	6	16	17	24	25	22	22	25	26	26	25	22	26	32	29	29	26	24	26	35	33	35	33	32	28	24	19	20	22	19	20
1648	7	12	14	20	20	20	20	22	23	22	20	19	23	30	31	26	22	19	22	28	26	28	26	28	26	19	14	15	19	15	15
1649	4	22	18	20	22	22	22	20	20	20	20	20	22	22	24	24	22	22	26	26	26	22	22	22	22	20	18	20	18	18	20
1649	5	17	16	17	18	21	18	18	18	18	18	17	18	18	21	22	22	22	22	22	22	18	21	21	17	16	16	16	17	18	
1649	6	16	14	20	22	22	22	20	20	18	20	20	22	25	27	24	24	27	27	27	32	29	24	20	18	18	18	18	20	22	
1649	7	14	14	23	23	22	23	22	22	23	20	23	22	20	26	28	23	25	28	30	31	33	31	22	19	19	22	20	20	23	22
1650	4	21	19	19	22	22	22	21	21	21	19	19	21	19	21	24	26	24	25	24	22	22	24	21	19	19	19	19	19	21	22
1650	5	17	14	16	18	19	19	18	17	17	16	14	16	17	18	21	23	21	23	21	19	20	19	18	16	17	14	16	17	18	19
1650	6	20	14	18	22	20	20	18	25	27	23	20	20	18	22	24	24	24	23	25	25	22	19	19	20	19	17	19	20	20	19
1650	7	19	12	20	22	19	20	20	30	33	25	22	22	20	23	23	25	26	23	26	26	22	19	19	19	19	19	20	22	22	20
1651	4	21	20	20	20	20	21	20	18	18	20	18	18	20	21	21	21	22	25	25	24	21	21	20	18	17	18	18	18	20	21
1651	5	19	17	17	17	18	18	18	14	15	17	14	15	17	17	19	21	21	22	22	22	19	18	18	15	14	15	17	15	19	19
1651	6	25	19	15	18	21	21	21	21	23	29	27	22	23	25	24	27	25	24	24	23	22	19	21	19	18	19	18	19	22	19
1651	7	25	19	14	19	22	20	20	20	23	33	26	22	23	26	25	26	23	22	23	20	17	19	20	20	20	19	19	19	20	17
1652	4	20	20	19	18	19	22	22	22	20	19	20	23	22	$$	$$	25	53	47	22	23	22	19	19	18	18	19	19	19	19	19
1652	5	18	17	13	14	18	18	18	18	17	17	18	18	18	$$	$$	21	57	40	21	21	18	17	15	14	14	14	15	17	18	17
1652	6	22	16	12	14	21	21	22	22	22	21	21	23	27	99	99	21	52	37	21	21	19	18	19	18	18	17	17	21	21	19
1652	7	23	14	9	12	22	22	23	23	23	22	20	26	30	$$	$$	95	85	33	17	19	19	19	17	19	20	17	19	20	19	19
1653	4	20	18	18	18	18	20	20	21	21	21	20	20	21	25	27	24	25	25	22	21	20	21	20	18	18	21	20	20	20	18
1653	5	17	16	13	13	17	18	18	18	18	17	16	14	17	22	26	22	22	25	21	18	17	18	17	17	17	18	17	18	17	16
1653	6	22	18	13	14	19	22	22	24	23	22	22	22	24	30	32	25	25	24	22	19	20	22	22	22	22	23	22	22	19	20
1653	7	23	15	9	12	20	20	22	23	22	20	20	22	25	34	33	26	26	22	20	15	19	22	22	22	22	22	20	22	19	17
1654	4	20	20	18	18	20	21	21	21	22	20	20	21	20	20	20	20	20	21	21	21	21	21	22	21	20	18	20	20	18	18
1654	5	18	17	14	14	17	17	17	19	18	18	16	14	17	16	17	16	18	18	17	19	18	19	19	18	17	16	16	18	16	16
1654	6	24	19	14	14	20	24	25	25	24	24	22	25	25	22	22	22	24	22	24	24	22	24	24	25	22	22	22	24	22	22
1654	7	22	17	11	11	17	20	25	22	22	22	19	25	23	19	19	20	23	20	22	19	20	23	22	23	20	19	22	22	19	19

LANDSAT 1
GRENIER FIELD, NH
3 NOV 1974
SCAN LINE 1651

⊕ BAND 4
(.5-.6μ)
◇ BAND 6
(.7-.8μ)
⊞ BAND 7
(.8-1.1μ)
· BAND 5
(.6-.7μ)

MSS SIGNAL LEVEL(% OF FULL SCALE)

PIXEL NUMBER

2-27
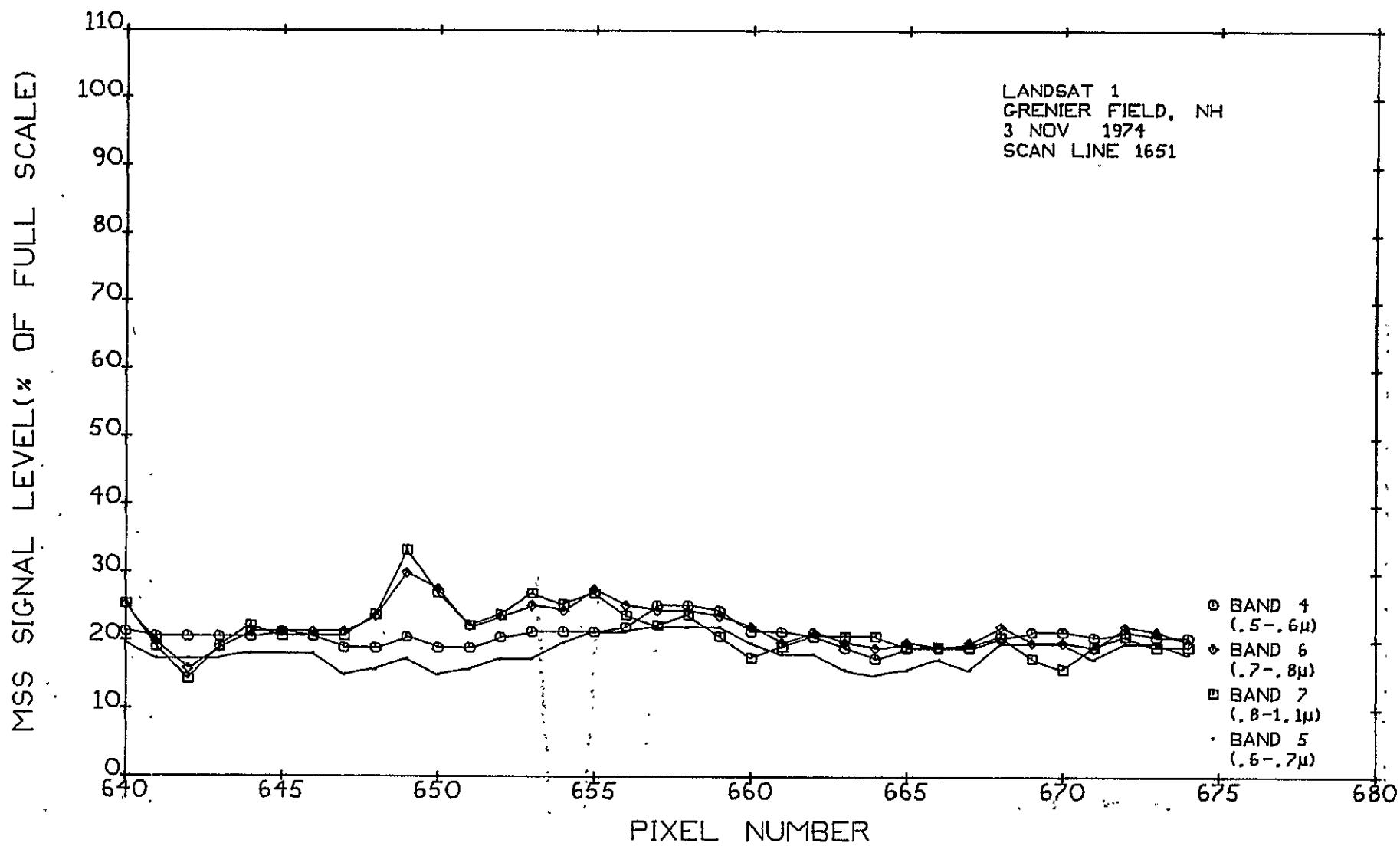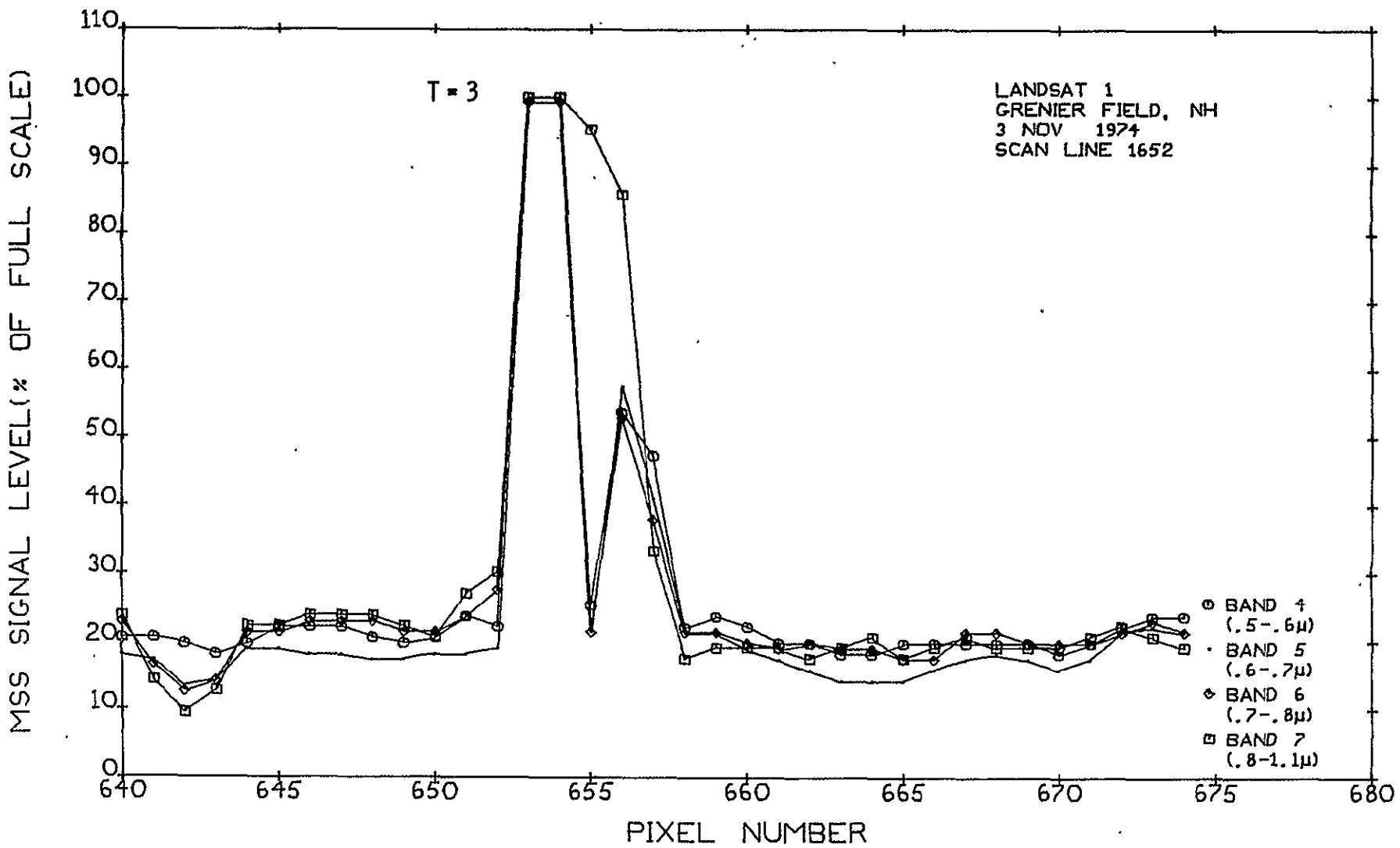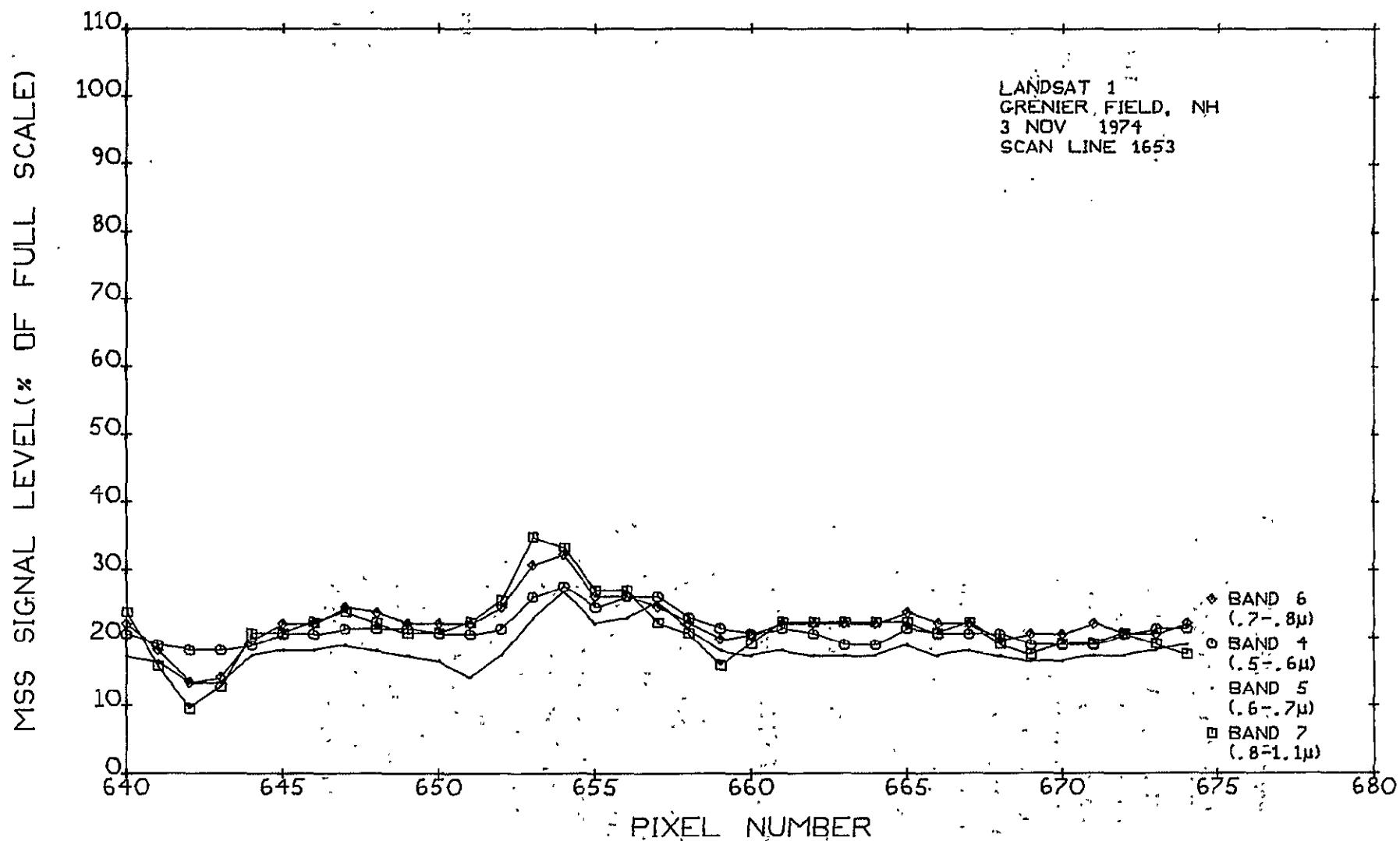
Figure 2-7

Figure   2-8

Figure 2-9

2.4.2   Data Reduction and Analysis

2.4.2.1   Definition of Experimental Beacon Pulse Amplitude (EBPA$_i$)

The experimental beacon pulse amplitude (EBPA$_i$) observed in the ith channel of the MSS was consistently evaluated as follows. Let P* represent the pixel number corresponding to the maximum signal level SL* of the searchlight signature in a given band of the MSS. The base line or background signal level BSL* was then defined as the average of SL(+P) and SL(-P), where SL(+P) was taken as the value of either SL(P*+1) or SL(P*+2), whichever was lower; and SL(-P) was taken as the value of either SL(P*-1) or SL(P*-2), whichever was lower. The empirical pulse amplitude was therefore consistently defined by the equation:

$$EBPA_i = SL* - BSL* = SL(P*) - .5[SL(+P)+SL(-P)] \text{ \%FS} \qquad (2-20)$$

2.4.2.2   Computation of Theoretical Beacon Pulse Amplitude (BPA$_i$)

The theoretical beacon pulse amplitude (BPA$_i$) was computed using Equation 2-16 with $\theta N_D \equiv 86/25 = 3.44$, the F_i values from Table 2-1, and the intensity values $I_o = I_o(\theta,T)$ from the calibration intensity curves given in Figure 2-6. The calibration intensity for a given profile is directly proportional to the d.c. input power (PS) to the xenon discharge lamp. This input power, which is displayed on each AN/TVS-3 searchlight by means of current and voltage meters, was found to vary slightly from searchlight to searchlight and even from one firing to the next of the same searchlight due to nominal deviations in the power supply control settings. The theoretical beacon pulse amplitude associated with a given searchlight was therefore adjusted in accordance with a power correction factor PCF $\equiv$ PS/15. The theoretically expected pulse amplitudes were therefore obtained from the following formulas:

$$BPA_4 = 0.179 \ PCF \ I_o(\theta,T) \ \%FS \qquad (2\text{-}21)$$

$$BPA_5 = 0.216 \ PCF \ I_o(\theta,T) \ \%FS \qquad (2\text{-}22)$$

$$BPA_6 = 0.242 \ PCF \ I_o(\theta,T) \ \%FS \qquad (2\text{-}23)$$

$$BPA_7 = 0.331 \ PCF \ I_o(\theta,T) \ \%FS \qquad (2\text{-}24)$$

The experiments and results obtained are briefly summarized in the following subsections. In those experiments involving more than one searchlight, it may help to recall that the pixel numbers correlate with a basically west to east scan.

2.4.3   Experiment No. 1 (Landsat 1)

The first experiment, of 11/3/74, was carried out at Grenier Air Field, Manchester, N.H., using two searchlights with PCF=1 and T=3. The searchlights were spaced 152 meters apart in the crosstrack direction, and the signatures obtained are shown in Figure 2-8. Due to a power cable mishap, it was thought that the eastward light was turned on a few seconds too late to be observed. The results suggest that either this was true and the light output had only reached about 36 percent of maximum, or the pointing angle was off by about one degree. In either case no meaningful comparison could be made with theory. The westward light, on the other hand, saturated all of the MSS channels. Consequently, the only conclusion that could be drawn from this data point was that the experimental pulse amplitudes were greater than 77, 81, 78, and 78 percent of full scale. This result is consistent with the predicted pulse amplitudes of 78, 94, 105, and 144 percent of full scale for $I_o(\theta=0, T=3)$, but the exact amount of agreement is indeterminate.

2.4.4   Experiments No. 2,3, and 4. (Landsats 2, 1, and 2)

Experiments 2, 3, and 4, of 2/28, 3/9, and 3/18/75, were carried out at the New Hampshire Army National Guard Armory in Manchester, New Hampshire, using one searchlight. The respective power correction factors (PCF) were 1.04, 1.04, and 1.03, and the beam spread for each light corresponded to the T=6 profile. The signatures obtained, with

the adjacent scan line data;are shown in Figures 2-10 through 2-18.
Experiments 2 and 4 were carried out with Landsat 2, and if one assumes
that all the lights scored a direct hit, $I_O = I_O(\theta=0, T=6)$, then the
theoretically expected MSS response is 46, 55, 62, and 85 per cent of
full scale for bands 4 to 7 respectively. A comparison of the theoreti-
cal and experimental responses is shown in Table 2-4 below, where the
symbols E and T are used to denote the experimental and theoretical
pulse amplitudes (for convenience) and the symbol SR is used to denote
the ratio E/T.

TABLE 2-4 .

Experimental Results and Theoretical Predictions·for Landsat

Searchlight Experiments 2, 3, and 4

	(2/28/75)			(3/9/75)					(3/18/75)		
	EXP.No.2			EXP.No.3					EXP.No.4		
	LANDSAT 2			LANDSAT 1					LANDSAT 2		
	E	T	SR	E	T	SR			E	T	SR
Band 4	56	46	1.22	41	46	0.89			58	45	1.29
Band 5	73	55	1.33	44	55	0.80			72	55	1.31
Band 6	74	62	1.19	45	62	0.73			64	61	1.05
Band 7	>90	85	>1.06	>83	85	>0.98			>86	84	>1.02

The Landsat 2 data was observed here to be consistently higher than the
Landsat 1 data by about 60 percent on bands 4 to 6 and by an indeter-
minate amount on band 7 which saturated in all three experiments. The
$BR_{gm}(i)$ values for the Landsat 2 MSS are the same as for Landsat 1, and
the same AN/TVS-3 searchlight was used in all three of these experi-
ments. It can only be concluded therefore that the searchlight inten-
sity for experiment No. 3 was somehow erroneously reduced to about 66
percent of its nominal value. This could be explained by an unbeliev-
ably large pointing offset, of about one degree,or by the assumption
that the searchlight power cable was inadvertently hooked up to the
10kw transformer receptacle instead of the 15kw receptacle.
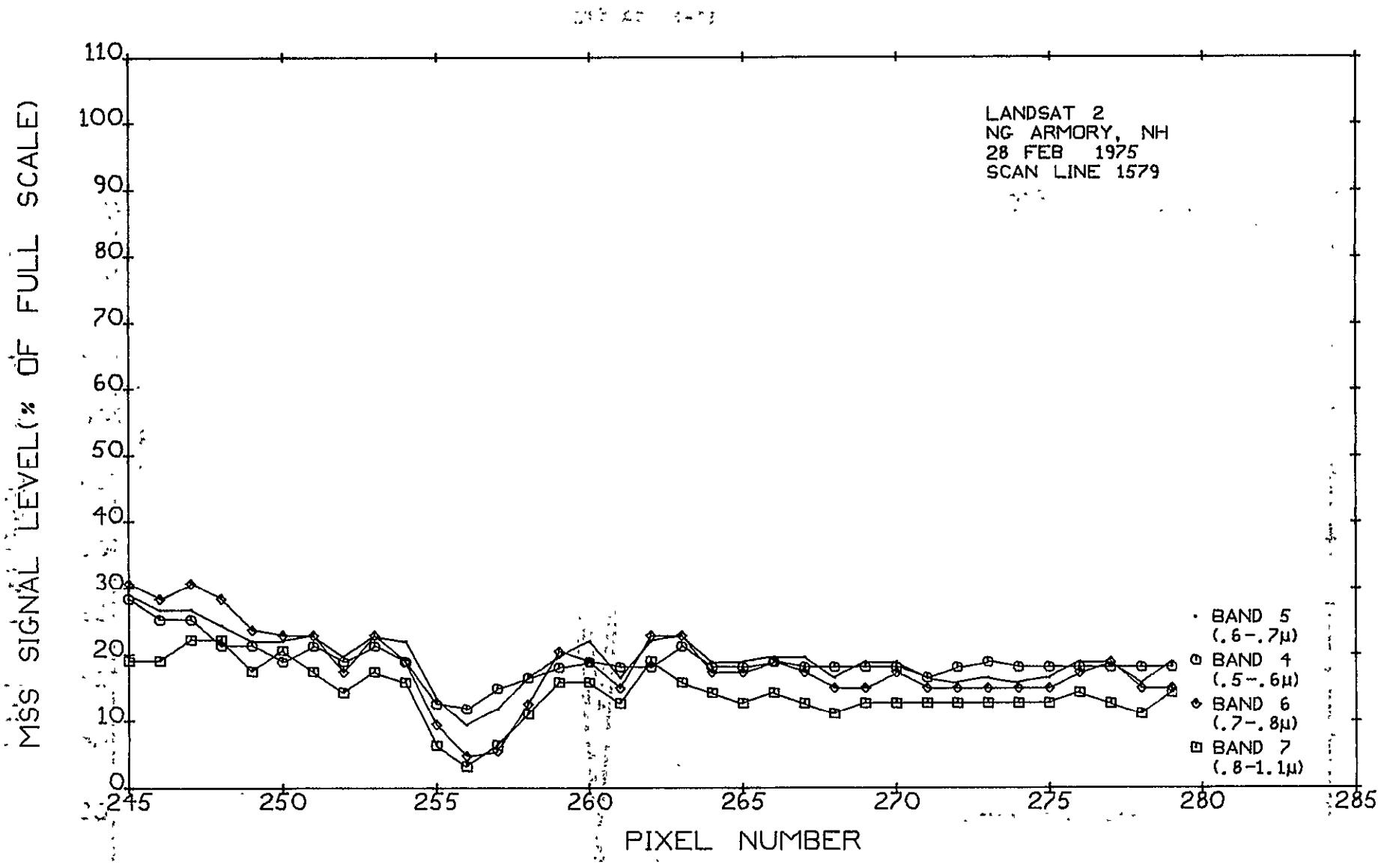
Figure 2-10
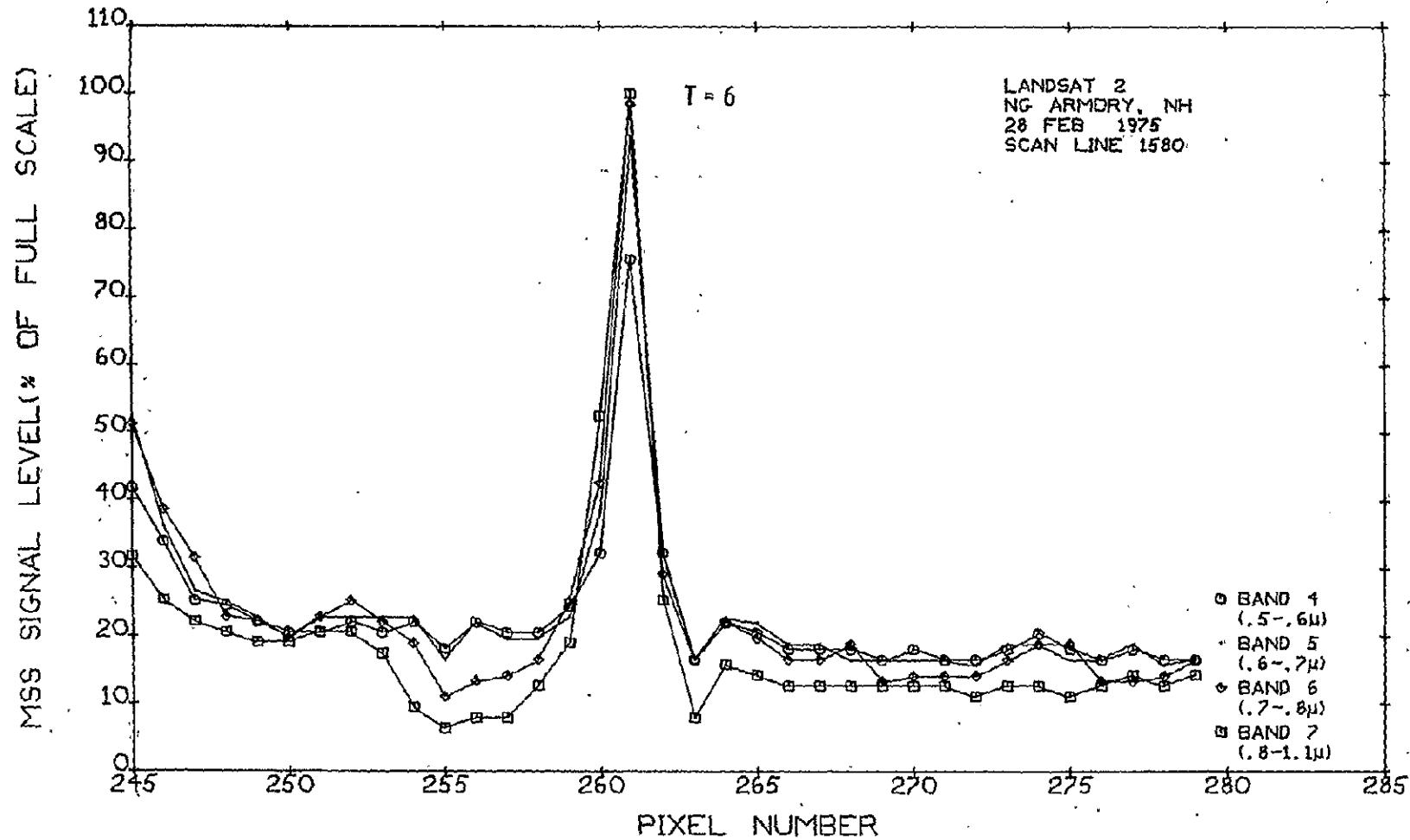
Figure 2-11
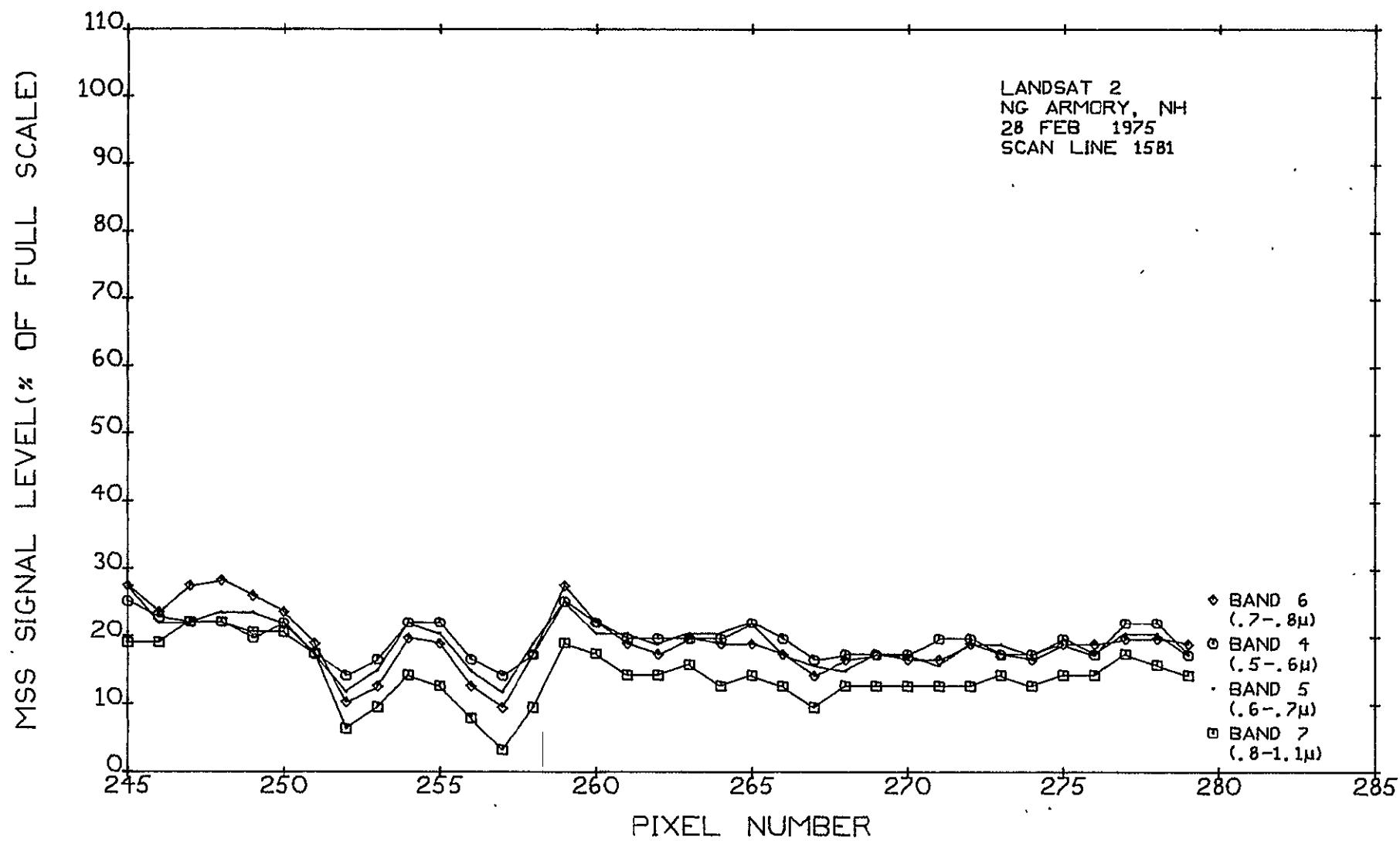
Figure   2-12
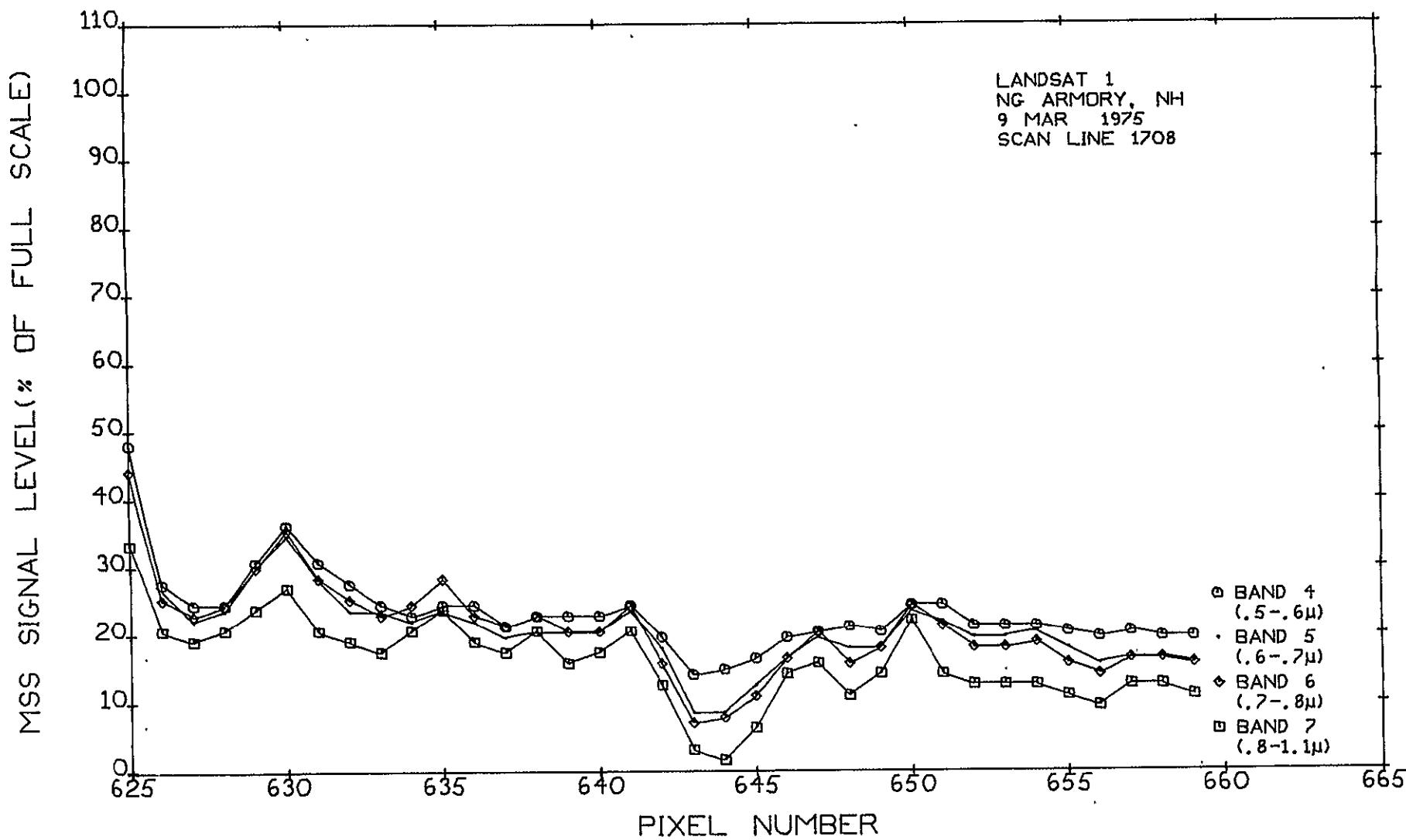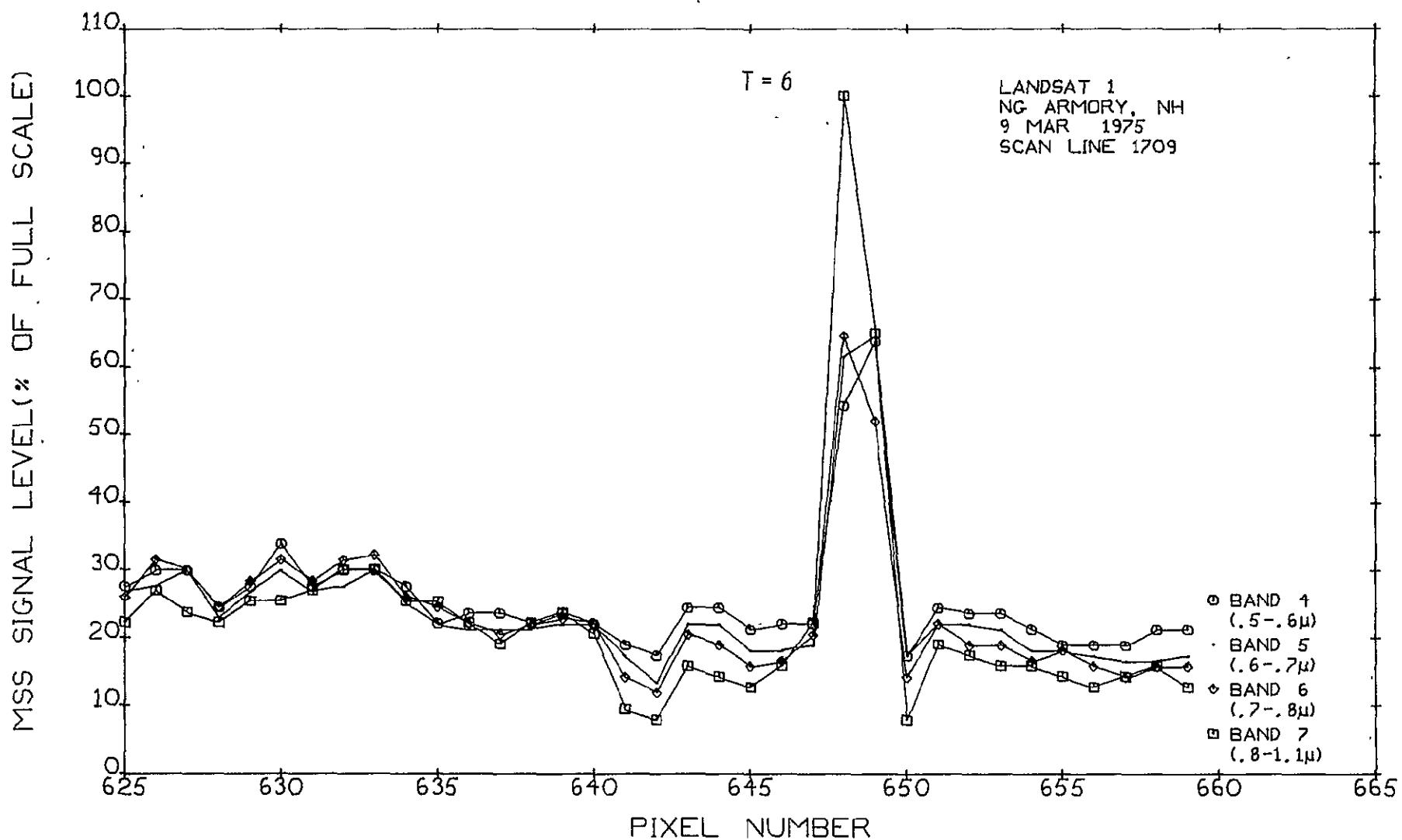
Figure 2-13

Figure 2-14
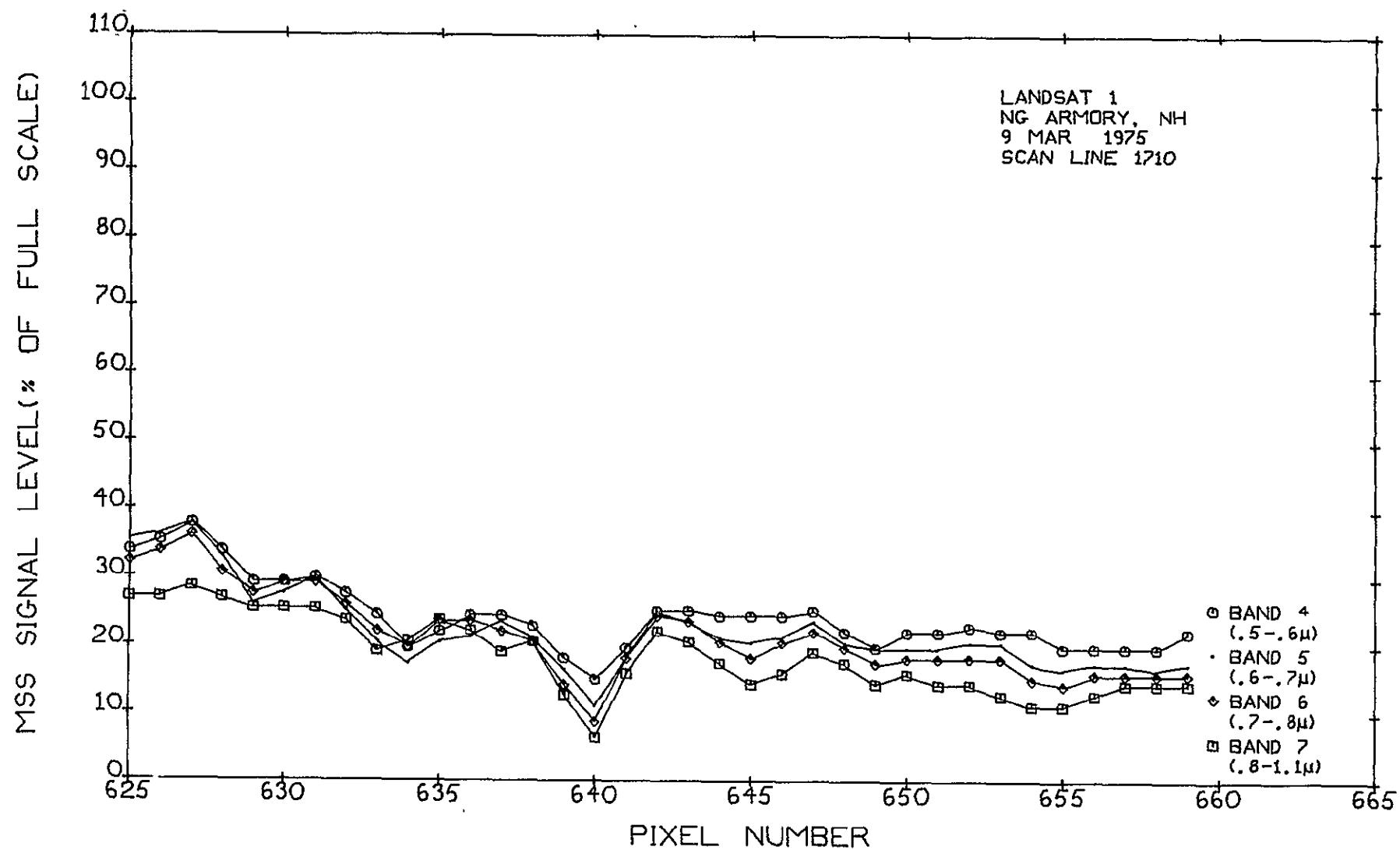
Figure 2-15
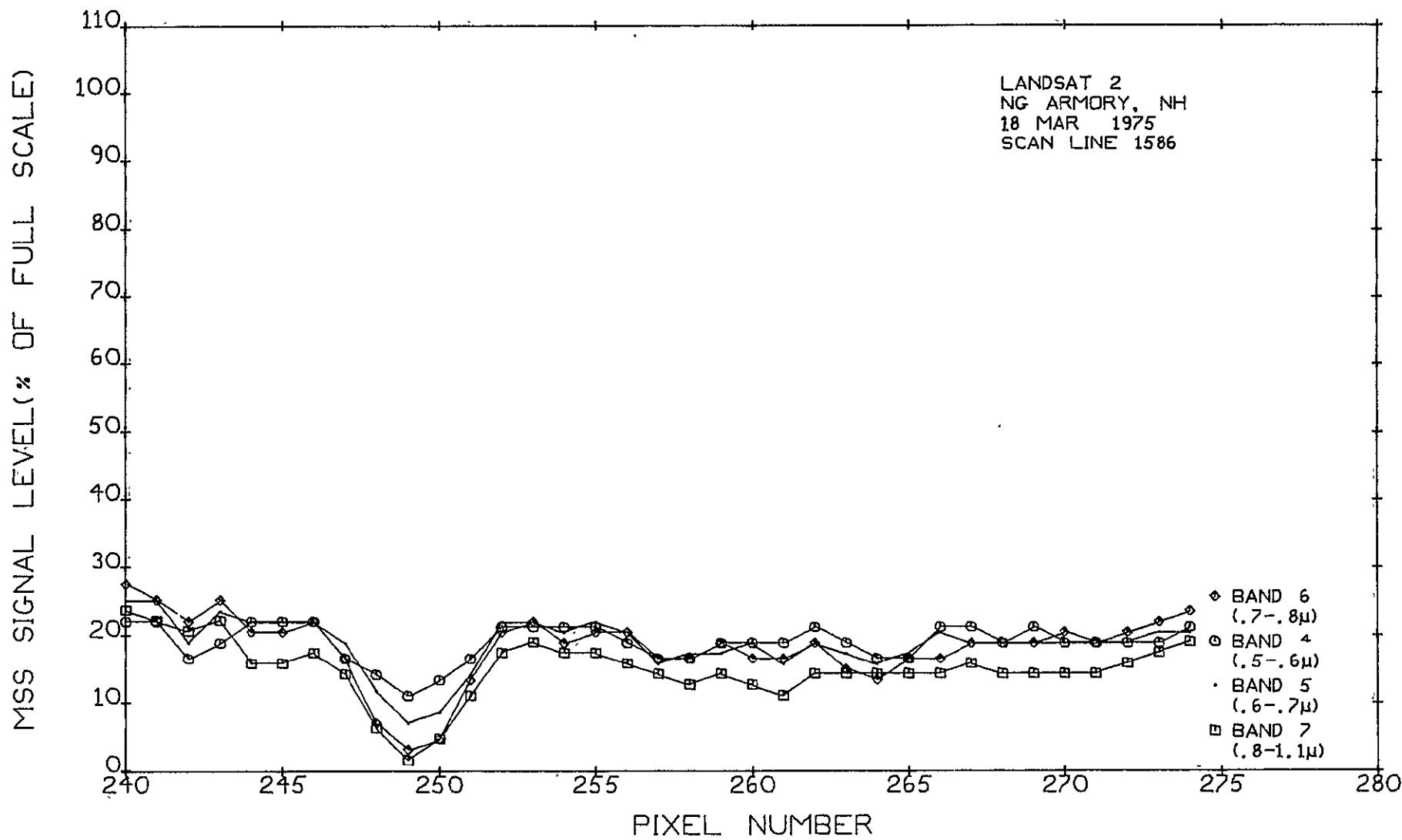
Figure 2-16
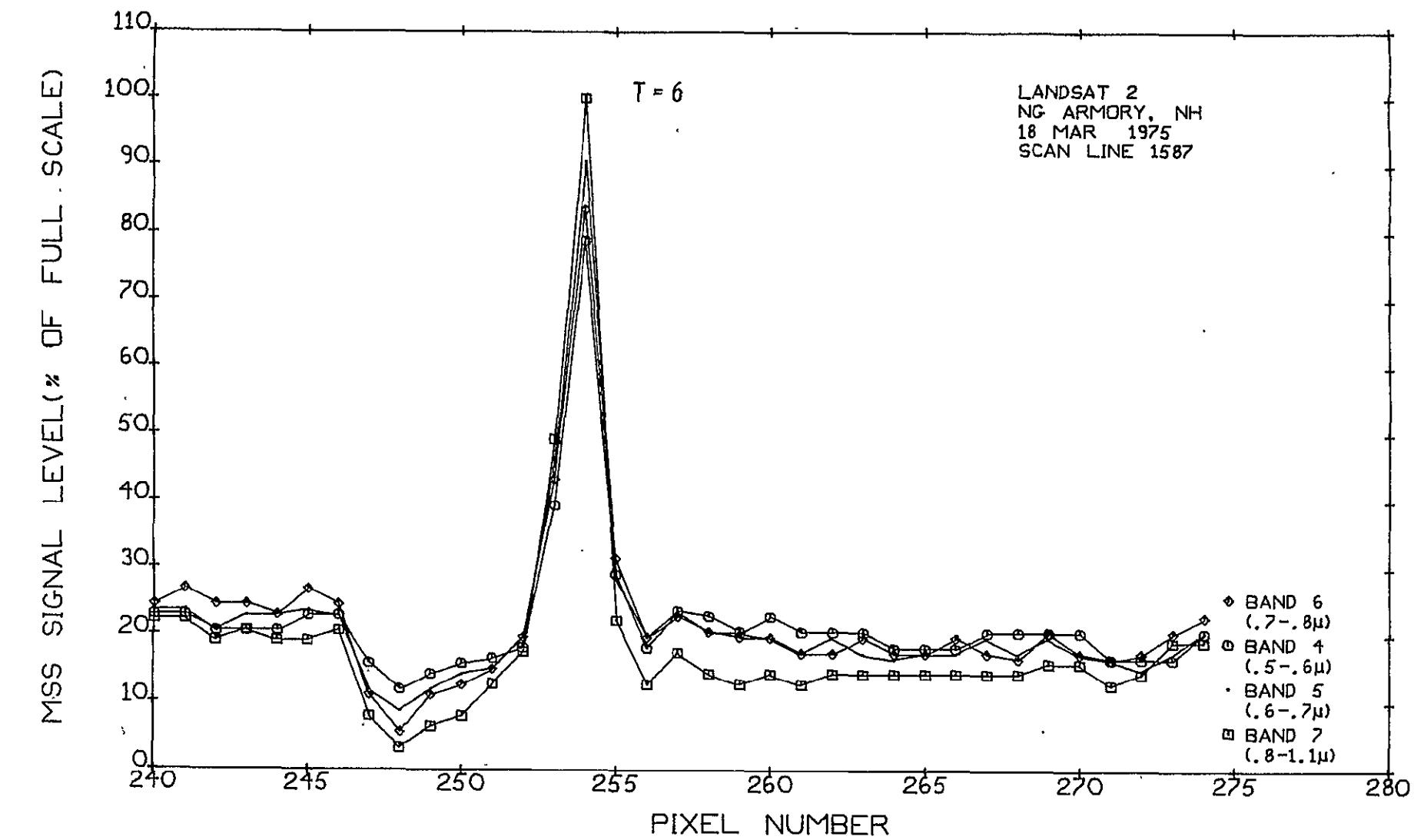
Figure 2-17
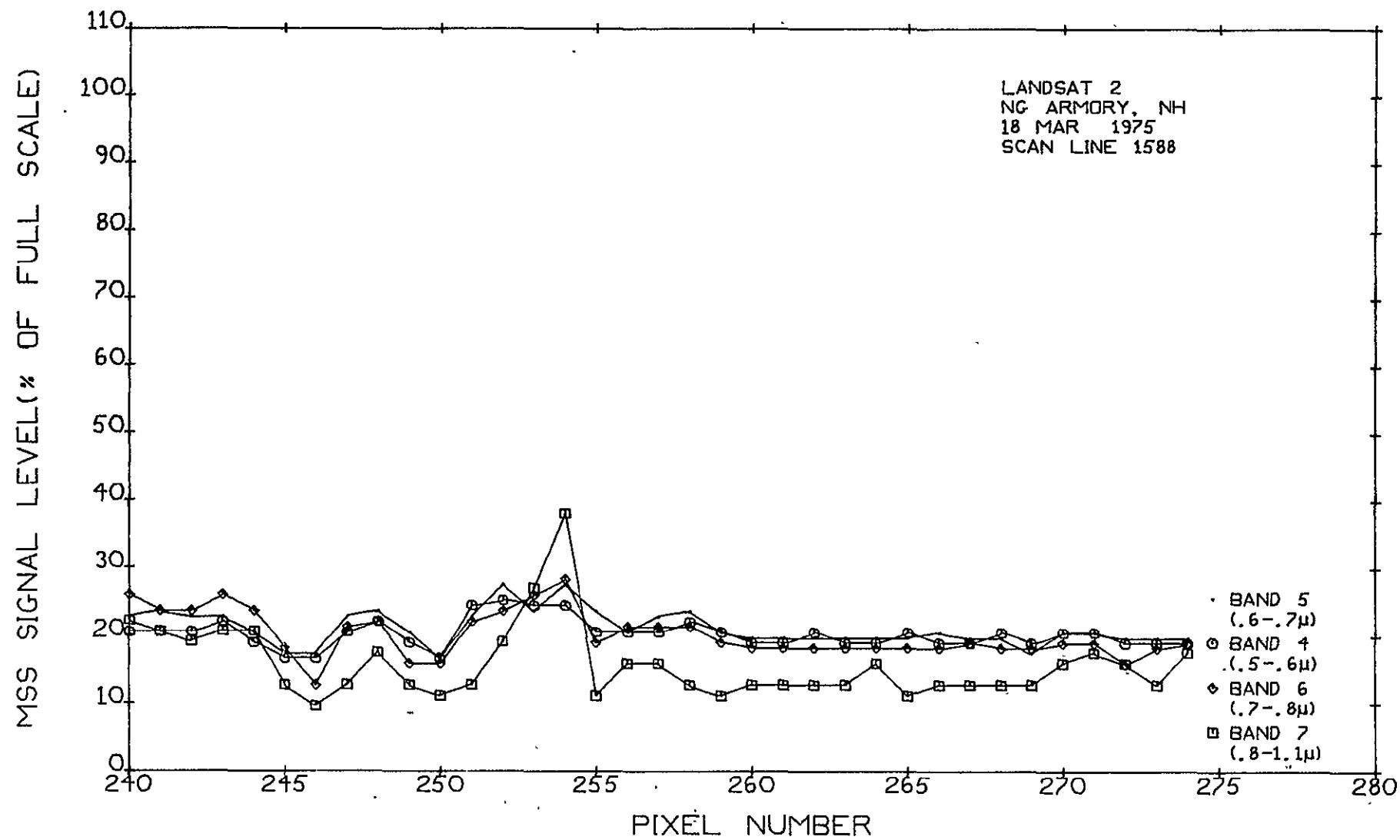
Figure 2-18

2.4.5   Experiment No. 5

        Experiment No. 5, of 5/3/75, was carried out at Barnes Munici-
pal Airport in Westfield, Massachusetts, utilizing three AN/TVS-3
searchlights. The lights were set up at three corners (NE, SW, and SE)
of a rectangle measuring 120 meters intrack by 157 meters crosstrack.
The PCF values for the NE, SW, and SE searchlights were 1.00, 1.03,
and 1.01, and the beam spread for each light was set at the T-7 profile.
The signatures obtained, and the adjacent scan line data,are shown in
Figures 2-19 through 2-22.

        This experiment was carried out with Landsat 1, and at the
time of the flyby the MSS was operating in the high gain mode for bands
4 and 5, and with zero compression for bands 4, 5, and 6. The signa-
ture for the NE light appears on scan line No. 488 where the band 4 and
5 components are seen to be saturation limited because of the high gain
mode employed.

        The signatures for the SW and SE lights appear on the next
scan line (489), and inspection of lines 487 to 490 reveals no visible
evidence of intrack detector sharing. In this experiment, the intrack
separation of the lights was equivalent to one and one half detector
elements. Thus if DS is the effective diameter of the image spot and
L is the width of the detector, this experiment shows that (1.5L + DS)
is less than 2L, or that DS is less than .5L. This is consistent with
the theoretical DS(λ) values (.2L, .25L, .29L, .37L) computed in
Section 2.1.3. If there had been an intervening line with no evidence
of detector sharing, the same result (DS<.5L) would have been implied.
A comparison of the experimental and theoretical pulse amplitudes is
shown in Table 2-5 for bands 6 and 7 only.
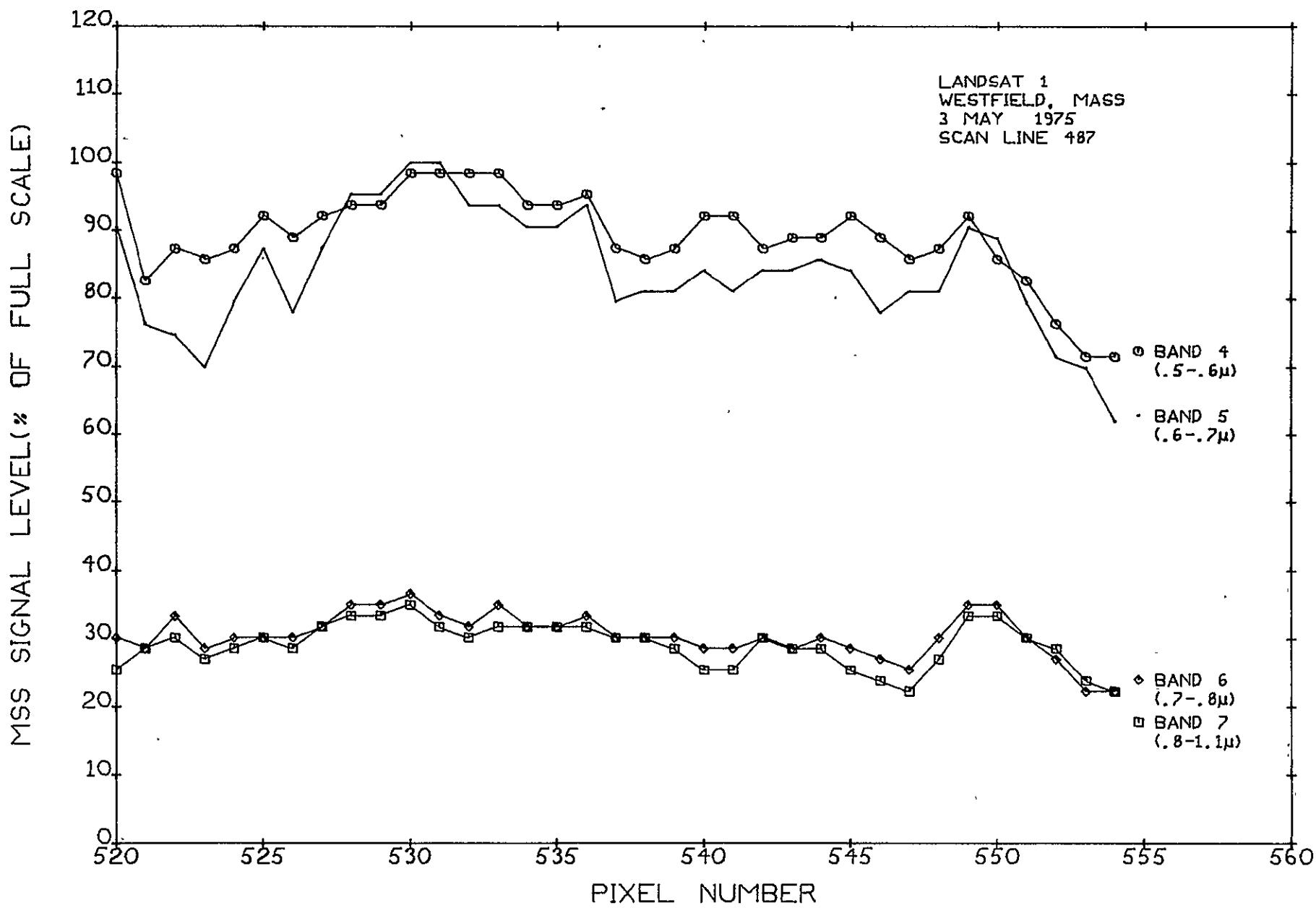
Figure 2-19
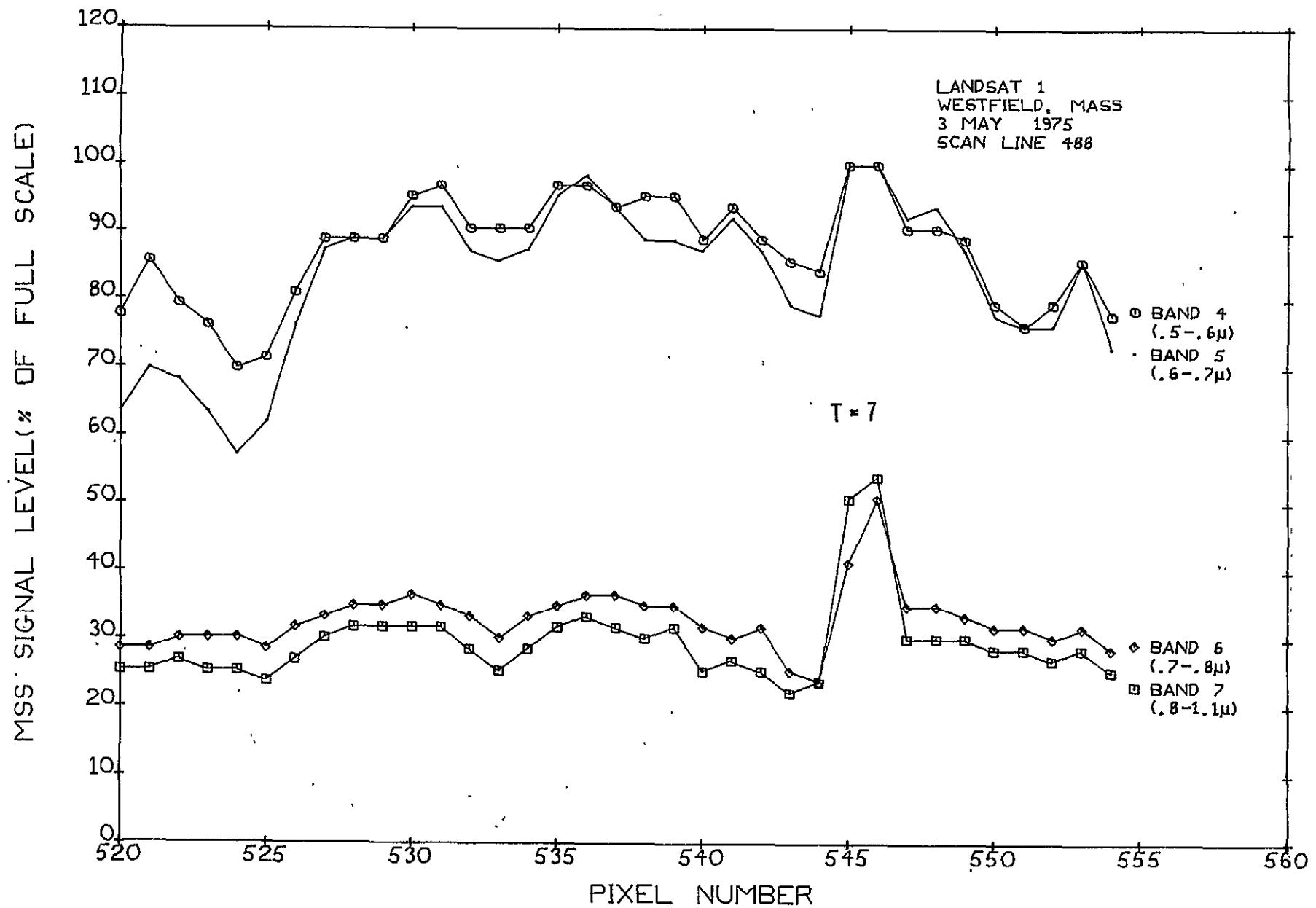
Figure 2-20
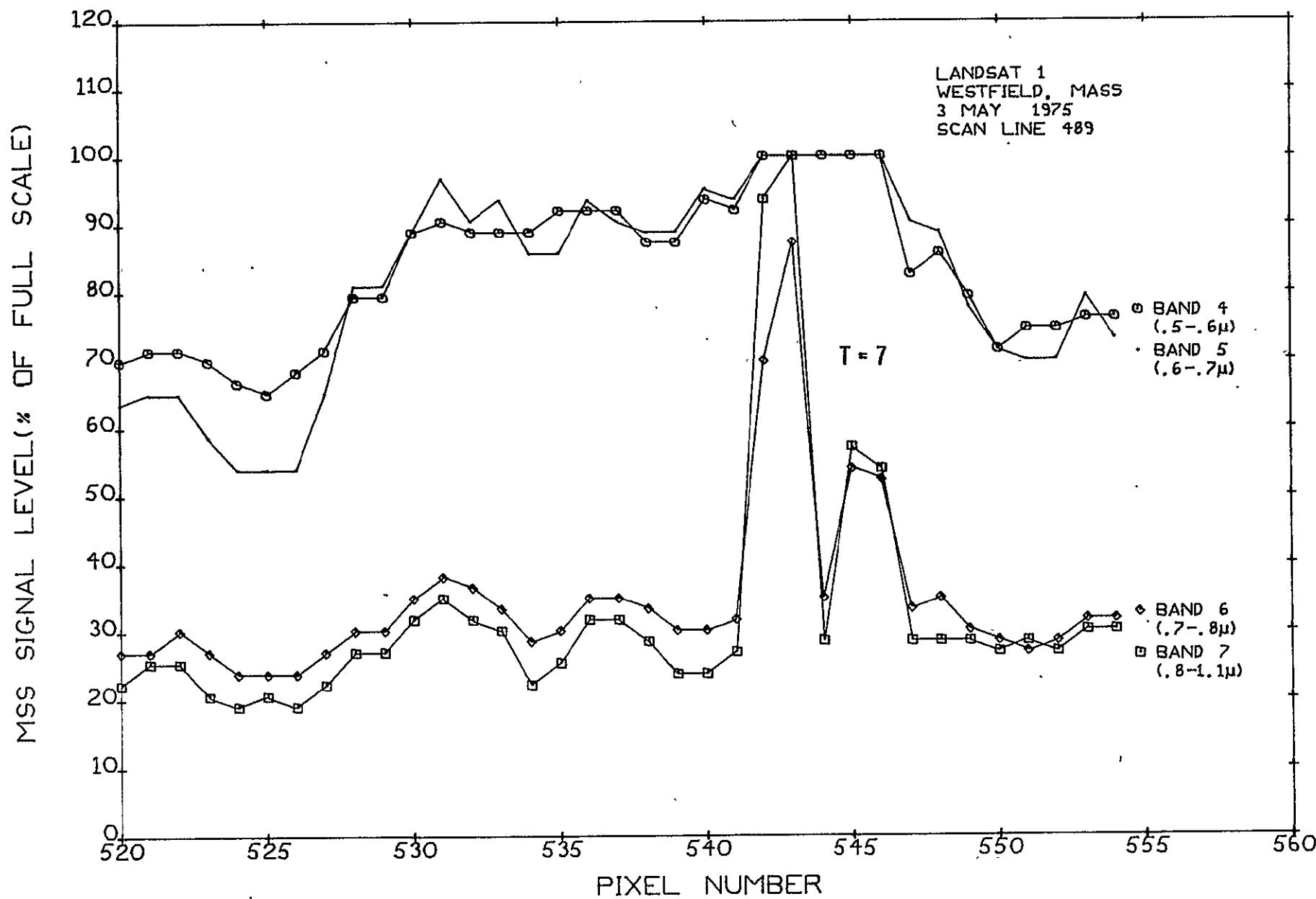
Figure 2-21

Figure 2-22

2-46
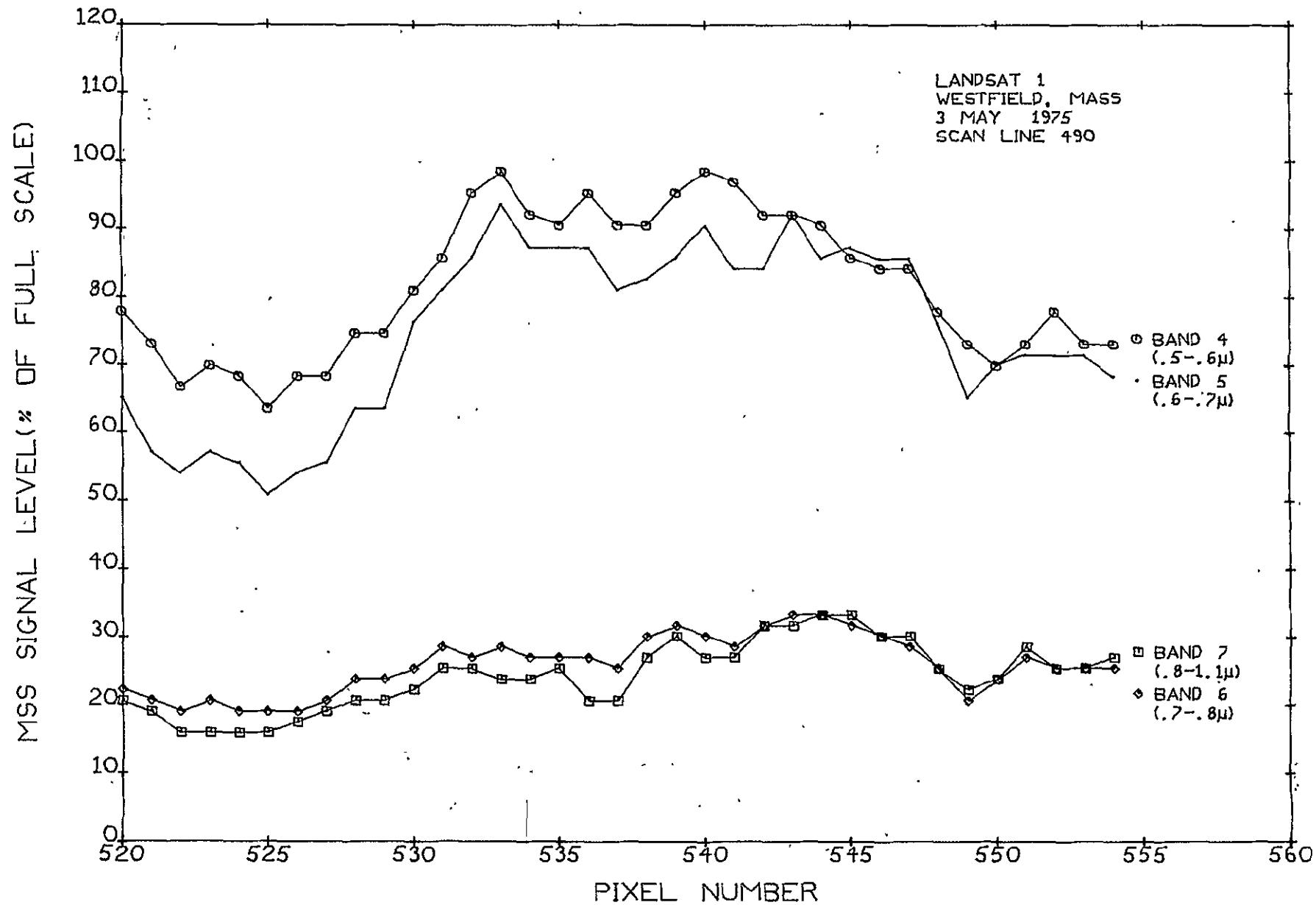
TABLE 2-5

EXPERIMENTAL RESULTS AND THEORETICAL PREDICTIONS
FOR LANDSAT/SEARCHLIGHT EXPERIMENT NO. 5

(May 3, 1975)

	NE LIGHT			SE LIGHT			SW LIGHT		
	E	T	SR	E	T	SR	E	T	SR
Band 6	22	47	0.47	19	48	0.40	54	47	1.15
Band 7	27	64	0.42	29	66	0.44	>73	64	>1.14

The signature of the SW light, as recorded by the Landsat 1 MSS, is consistent with the two signatures recorded previously by the Landsat 2 MSS for experiments 2 and 4, in that the experimental results are slightly greater than the theoretical prediction. This tends to confirm the belief that the scale factors or sensitivities are the same for the MSSs of Landsat 1 and Landsat 2. At the same time this suggests that the results of Experiment No. 3 were indeed abnormal, for reasons unknown. The experimental results for the NE and SE lights in this experiment are equally puzzling, however, because of the fact that they are so identical and yet so far off from what was theoretically expected. Also, the actual band 6 and band 7 responses of these two lights are both very nearly equal to 38% of the actual band 6 and 7 responses for the SE light. It is also curious that the SR values for these eastward lights are very nearly the same as the SR values for the eastward light in the first experiment of 11/3/74.

2.4.6 Experiment No. 6 (Landsat 1)

Experiment No. 6, of 5/7/75, was carried out in the large parking lot of the Batavia Downs Race Track, in Batavia, N.Y., using the same experimental set up as that of Experiment No. 5. The signatures obtained, and the adjacent scan line data, are shown in Figures 2-23 through 2-26. As in Experiment No. 5, there is no visible evidence of detector sharing, and the separate signatures occurred again on two consecutive lines, even though the searchlights were separated by the equivalent of 1.5 detector widths in the intrack direction.
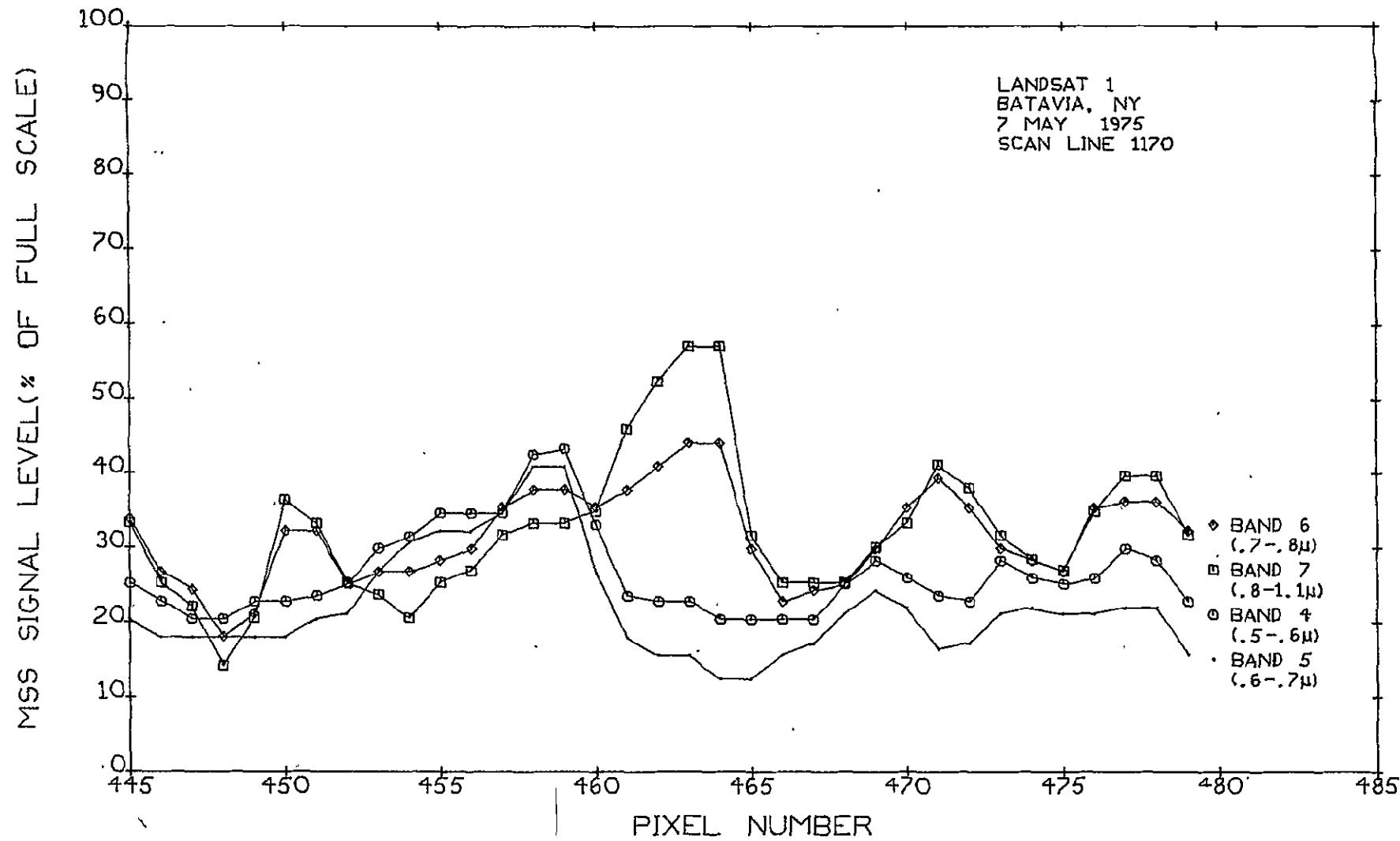
Figure 2-23
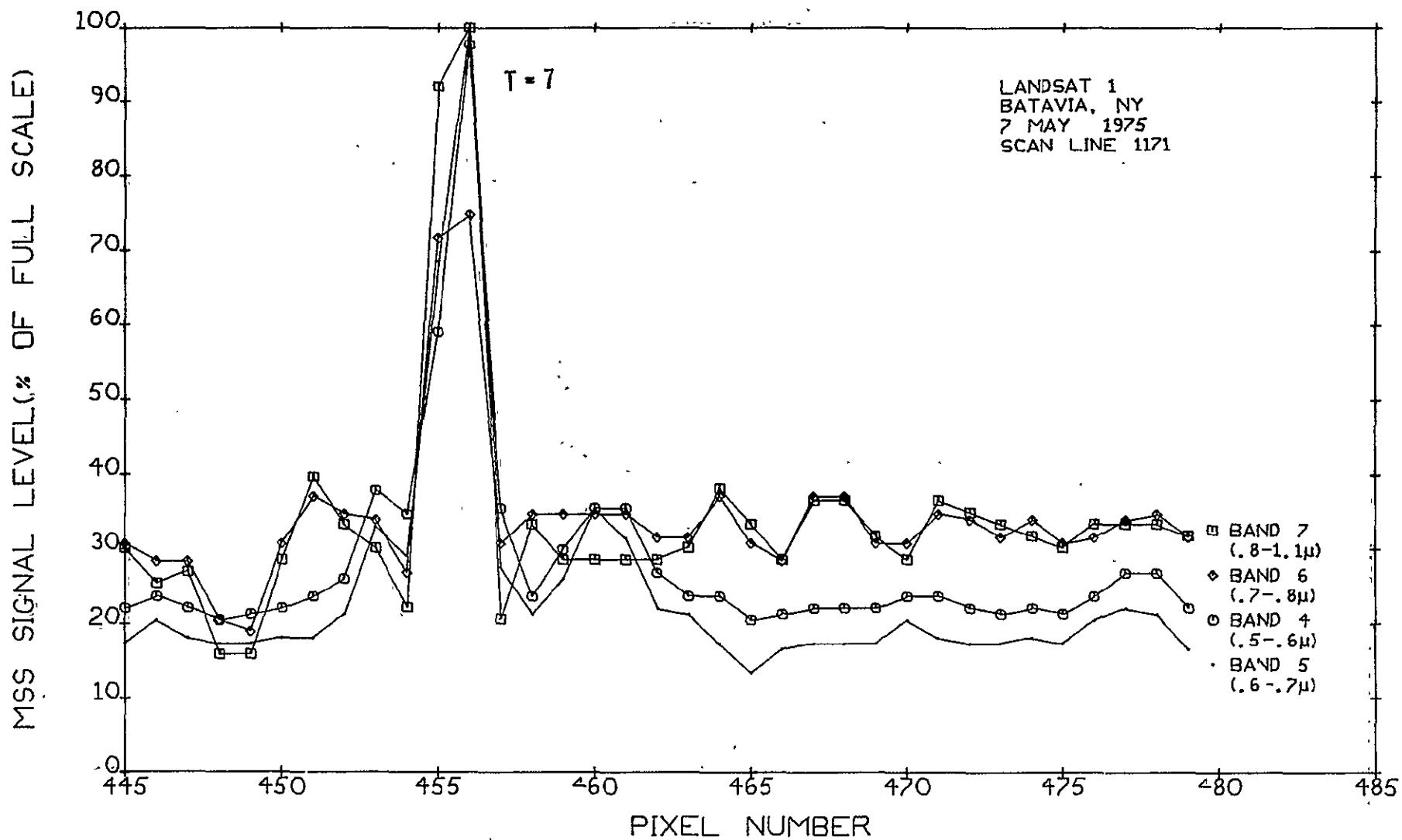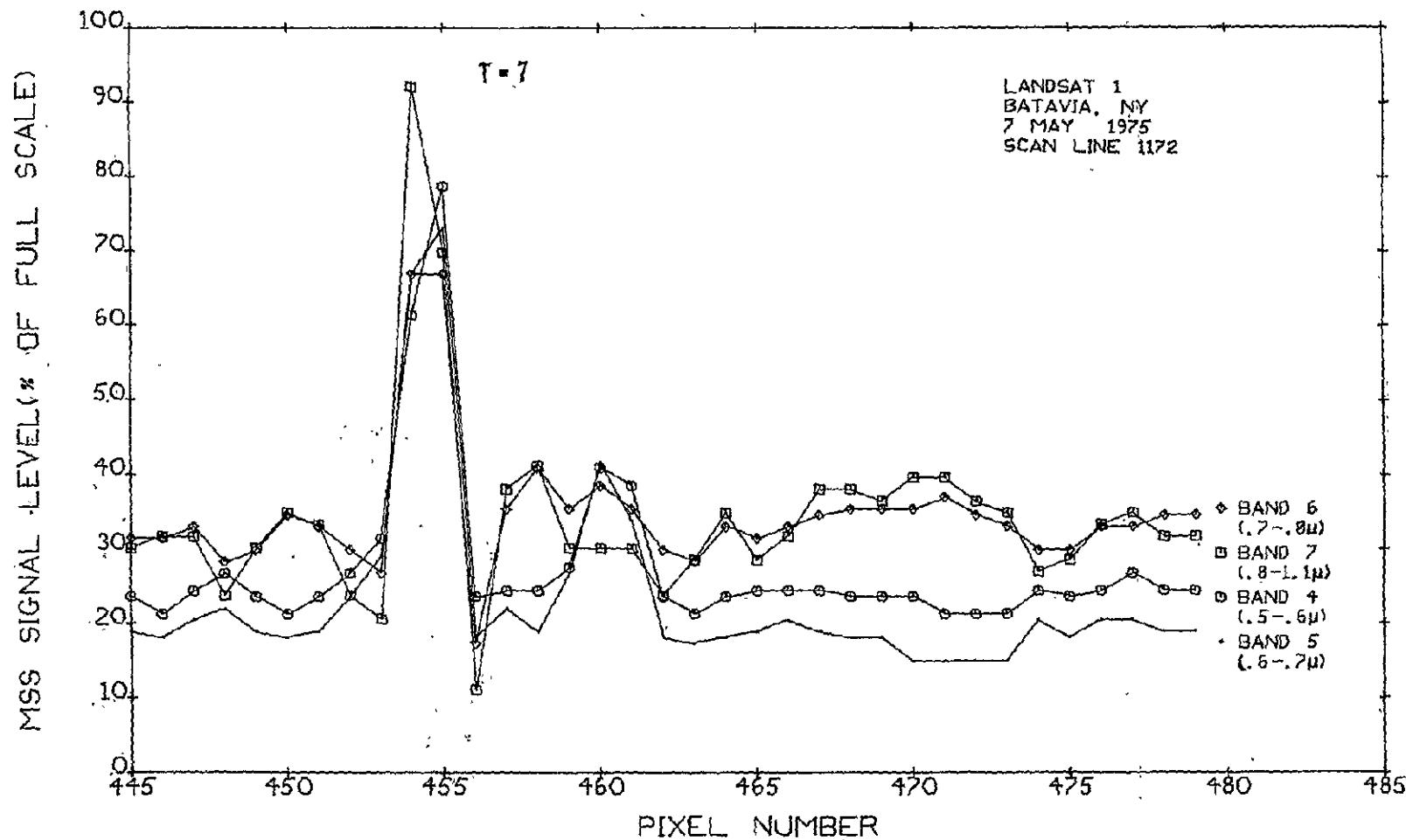
Figure 2-24

Figure 2-25
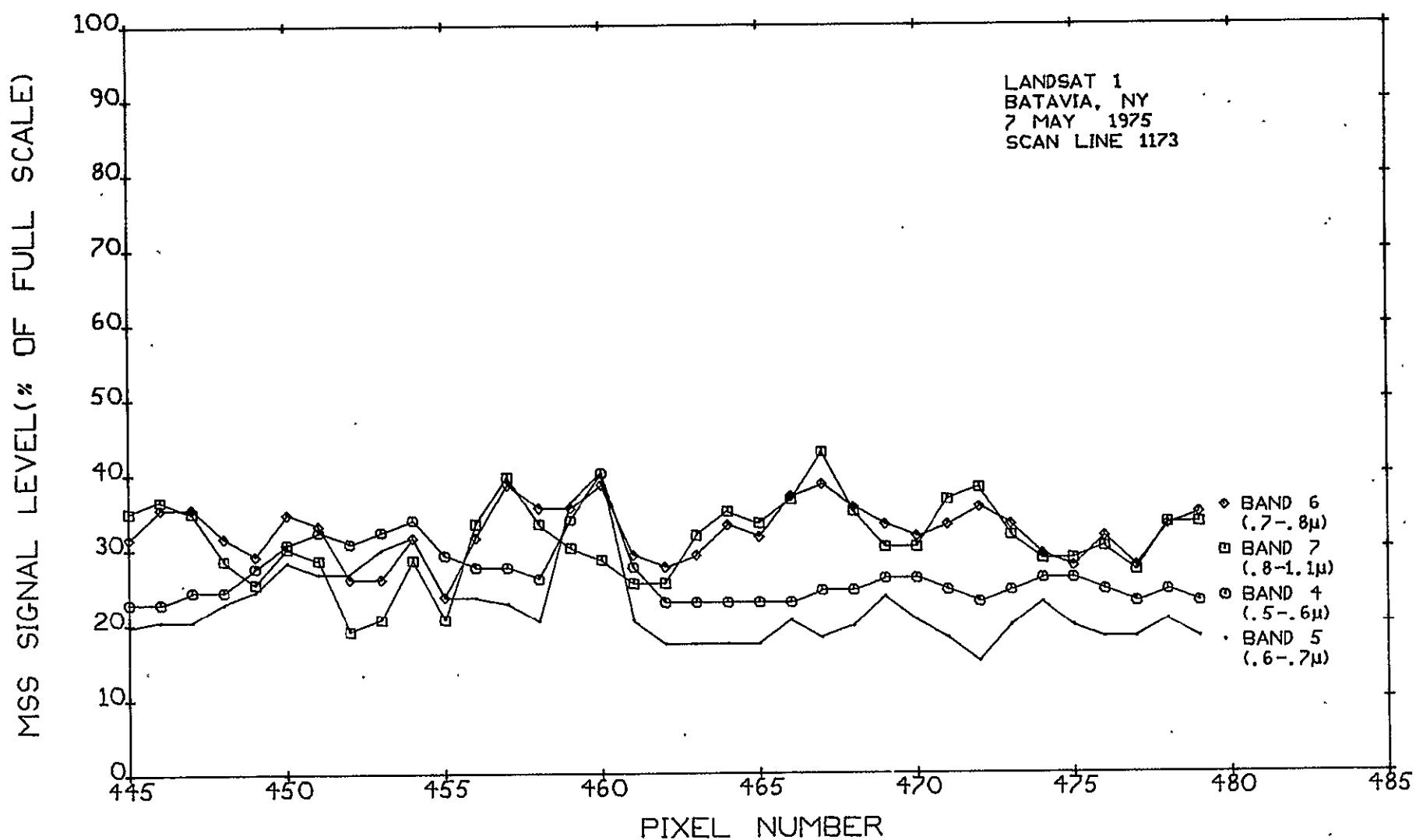
Figure 2-26

In contrast to results of Experiment No. 5, however, the signatures of the two eastward lights came through loud and clear, and it was the signature of the SW light that was abnormally low, so low in fact that it is not visible at all. Since power correction factors of 1.01 were reported for all three lights, it can only be concluded that an abnormally large pointing error was inadvertently introduced in the azimuth and/or elevation setting of the SW light. A comparison of the experimental results and theoretical predictions for the two eastward lights is shown in Table 2-6.

TABLE 2-6

EXPERIMENTAL RESULTS AND THEORETICAL PREDICTIONS
FOR LANDSAT/SEARCHLIGHT EXPERIMENT NO. 6

(May 7, 1975)

	NE LIGHT				SE LIGHT		
	E	T	SR		E	T	SR
Band 4	68	35	1.94		51	35	1.46
Band 5	≥ 75	42	≥ 1.79		50	42	1.19
Band 6	46	47	0.98		45	47	0.96
Band 7	≥ 79	64	≥ 1.23		77	64	1.20

These results show an abnormaly high response for the band 4 and 5 signatures of the NE light and also the band 4 signature of the SE light. Inspection of scan lines 1170 to 1173 suggests that this can most likely be attributed to the unusually large amplitude and high frequency structure of the background noise.

2.4.7 Experiment No. 7 (Landsat 2)

Experiment No. 7, of 6/26/75, was conducted in the mountainous sagebrush terrain of the Army's Camp Williams Military Reservation in Riverton, Utah. This experiment utilized a total of 9 AN/TVS-3 searchlights and was carried out by the entire complement of the Army National Guard's Searchlight Battery A, in lieu of a night training mission previously scheduled for that date.[3] The experimental arrangement employed is illustrated in Figure 2-27 and described below.

```
                              True
                              North
                                              x (9)
                                 |
                              c  |
      |←— a —→|               |  |      Scan
——x———————x———————x———————x——⊗——x—————x————————x——→ Direction
  (7)      (6)     (5)     (4)    |(3)  (2)     (1)
                              b  |
                                 |
                                  x (8)

        a = 157 meters
        b = 134 meters
        c =  80 meters          Spacecraft
                                 Heading
```
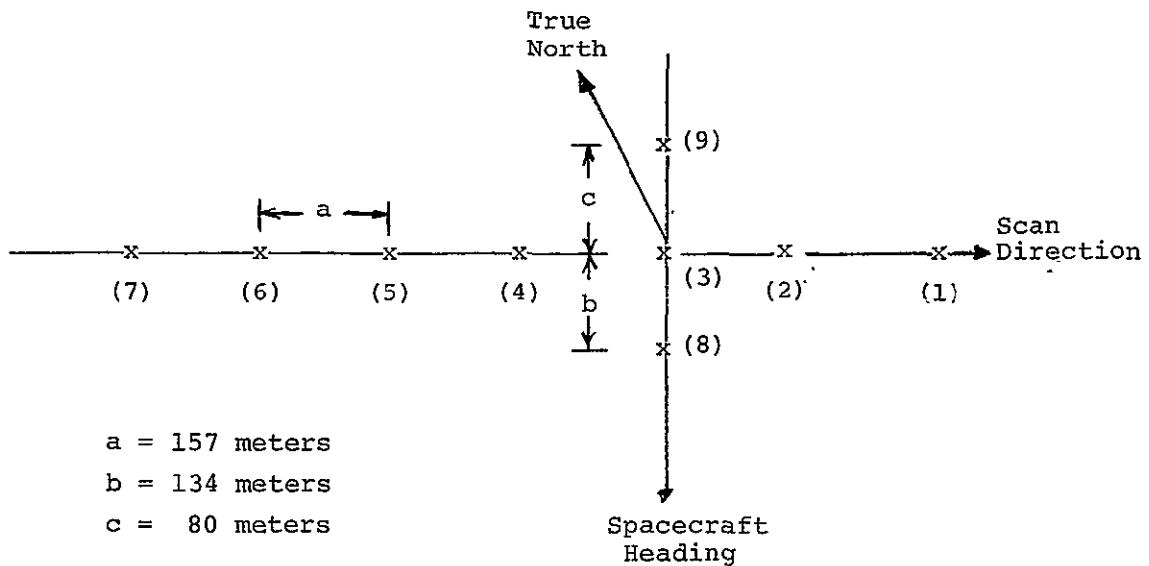
Figure 2-27   ARRANGEMENT OF SEARCHLIGHTS FOR LANDSAT 2 SEARCHLIGHT
EXPERIMENT NO. 7

In Figure 2-27, the AN/TVS-3 searchlights are identified by the reference numbers 1-9. Lights 1-7 were spaced 157 meters apart in the scan direction and light No. 4 was aimed to intercept the predicted orbit of Landsat 2. The beam spread of each light was adjusted to the T=9 profile, and the pointing angles for lights 5 to 7 and lights 3 to 1 were increased and decreased symmetrically, relative to that of light No. 4, by 0.84, 1.4, and 2.25 degrees respectively. Lights 8 and 9 were positioned along the intrack direction, spaced 134 meters (down-track) and 80 meters (uptrack) relative to light No. 3, and pointed in the same direction as light No. 3. The signatures obtained, and the adjacent scan line data,are shown in Figures 2-28 through 2-33.

The first signature encountered, that for light No. 9, is shown in the data for scan line 882. The signatures for lights 1 through 6 are clearly visible in the data for scan line 883, and the signature for light No. 8 is clearly visible in the data for scan line 885. The $I_o(\theta=2.5, T=9)$ for lights 1 and 7 was very close to the end

points of the T=9 profile, where $I_o(\theta,T)$ drops off very rapidly. Thus, the absence of a signature for light No. 7 could easily be accounted for by a pointing offset (relative to the true position of Landsat 2) of 0.3 degrees. Inspection of scan lines 881 through 886 failed to reveal any evidence of intrack detector sharing. Thus, eleven scan lines in all, containing a total of 17 searchlight signatures, were obtained without any visible evidence of intrack detector sharing. A comparison of the experimental results and theoretical predictions for this experiment is shown in Table 2-7.

TABLE 2-7

EXPERIMENTAL RESULTS AND THEORETICAL PREDICTIONS

FOR LANDSAT/SEARCHLIGHT EXPERIMENT NO. 7

(June 26, 1975)

Band	Light No. 1			Light No. 2			Light No. 3		
	E	T	SR	E	T	SR	E	T	SR
4	8	6	1.33	11	11	1.00	8	15	0.53
5	7	8	0.88	15	13	1.15	13	18	0.72
6	6	9	0.67	16	14	1.14	15	21	0.71
7	12	12	1.00	18	20	0.90	31	28	1.11

Band	Light No. 6			Light No. 5			Light No. 4		
	E	T	SR	E	T	SR	E	T	SR
4	12	12	1.00	19	16	1.19	19	22	0.86
5	16	15	1.07	25	20	1.25	21	27	0.78
6	19	16	1.18	29	24	1.21	25	31	0.81
7	31	22	1.41	39	30	1.30	43	42	1.02

Band	Light No. 8			Light No. 9		
	E	T	SR	E	T	SR
4	5	14	0.36	6	13	0.46
5	11	17	0.65	9	15	0.60
6	9	19	0.47	12	17	0.71
7	15	26	0.54	25	24	1.04
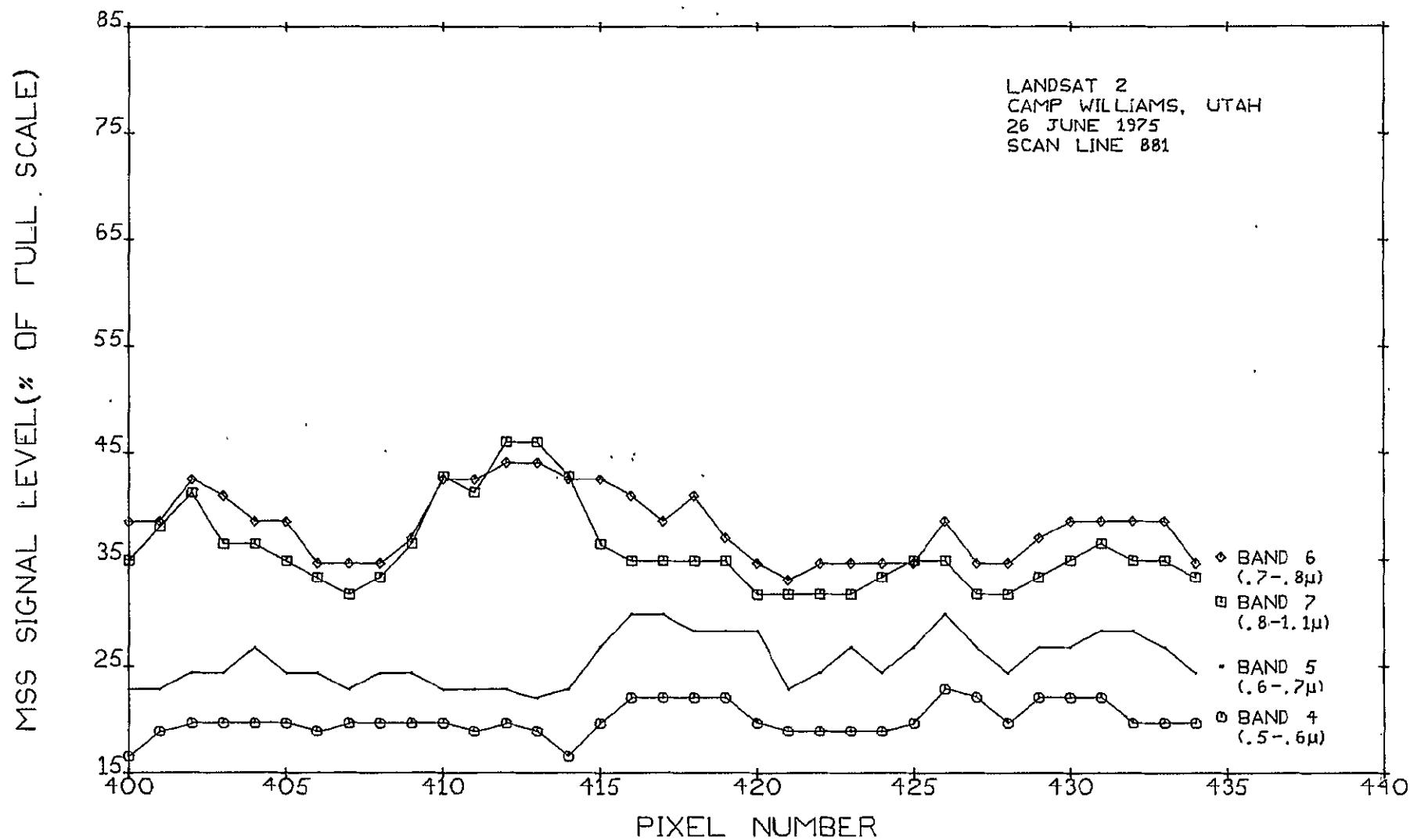
Figure 2-28
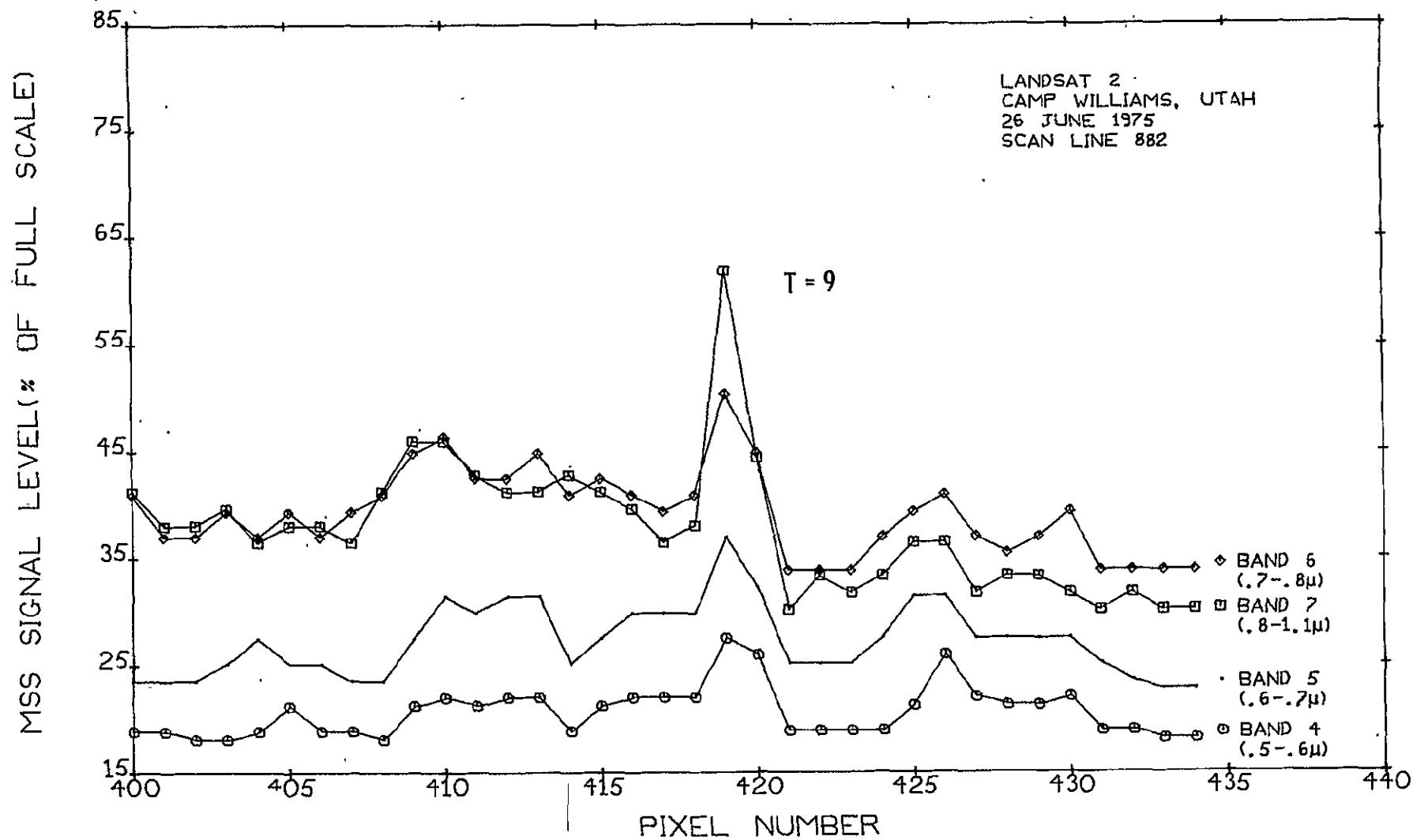
Figure 2-29

Figure 2-30

Figure 2-31

LANDSAT 2
CAMP WILLIAMS, UTAH
26 JUNE 1975
SCAN LINE 885

$T = 9$

BAND 6
(.7-.8μ)

BAND 7
(.8-1.1μ)

BAND 5
(.6-.7μ)

BAND 4
(.5-.6μ)

MSS SIGNAL LEVEL(% OF FULL SCALE)

PIXEL NUMBER
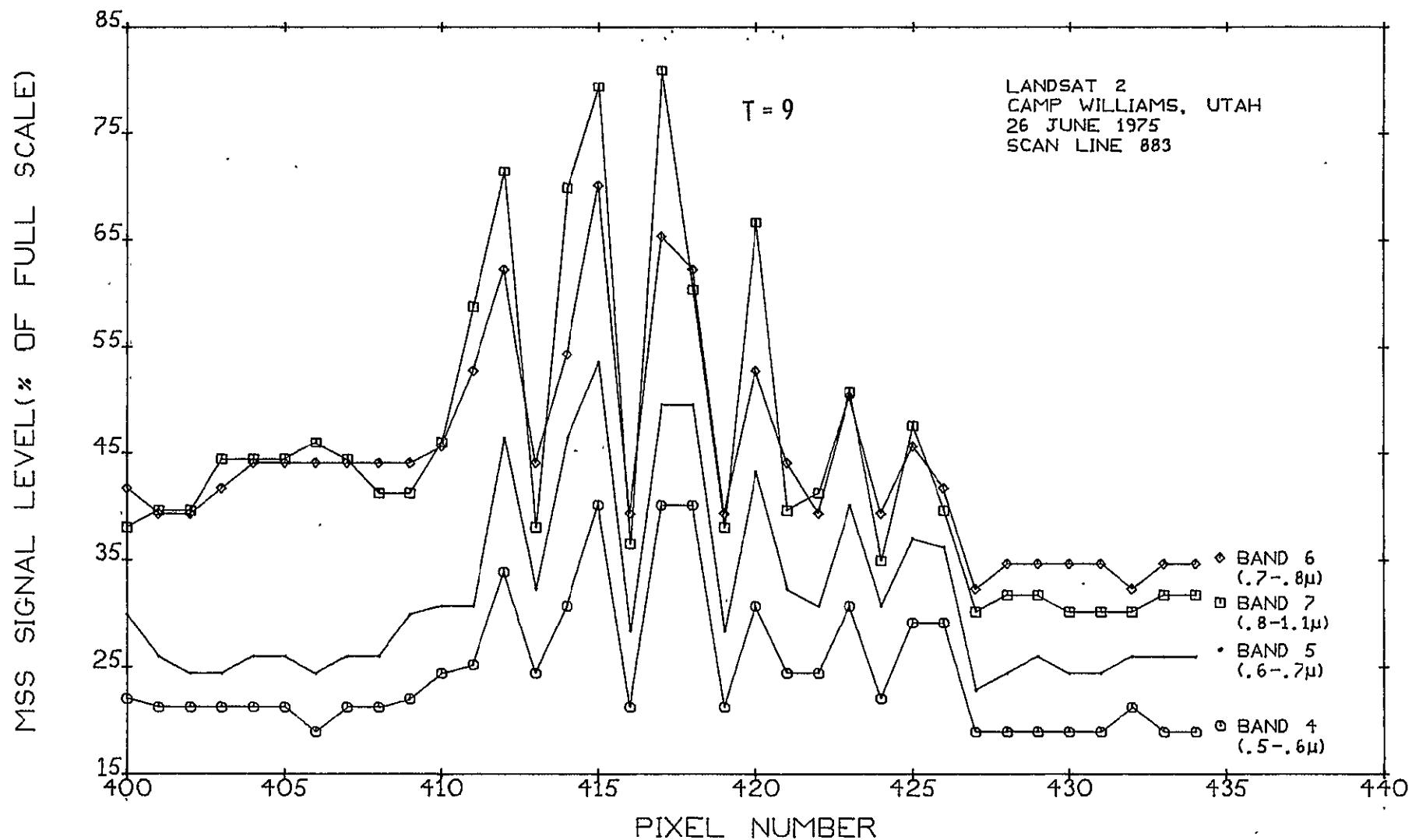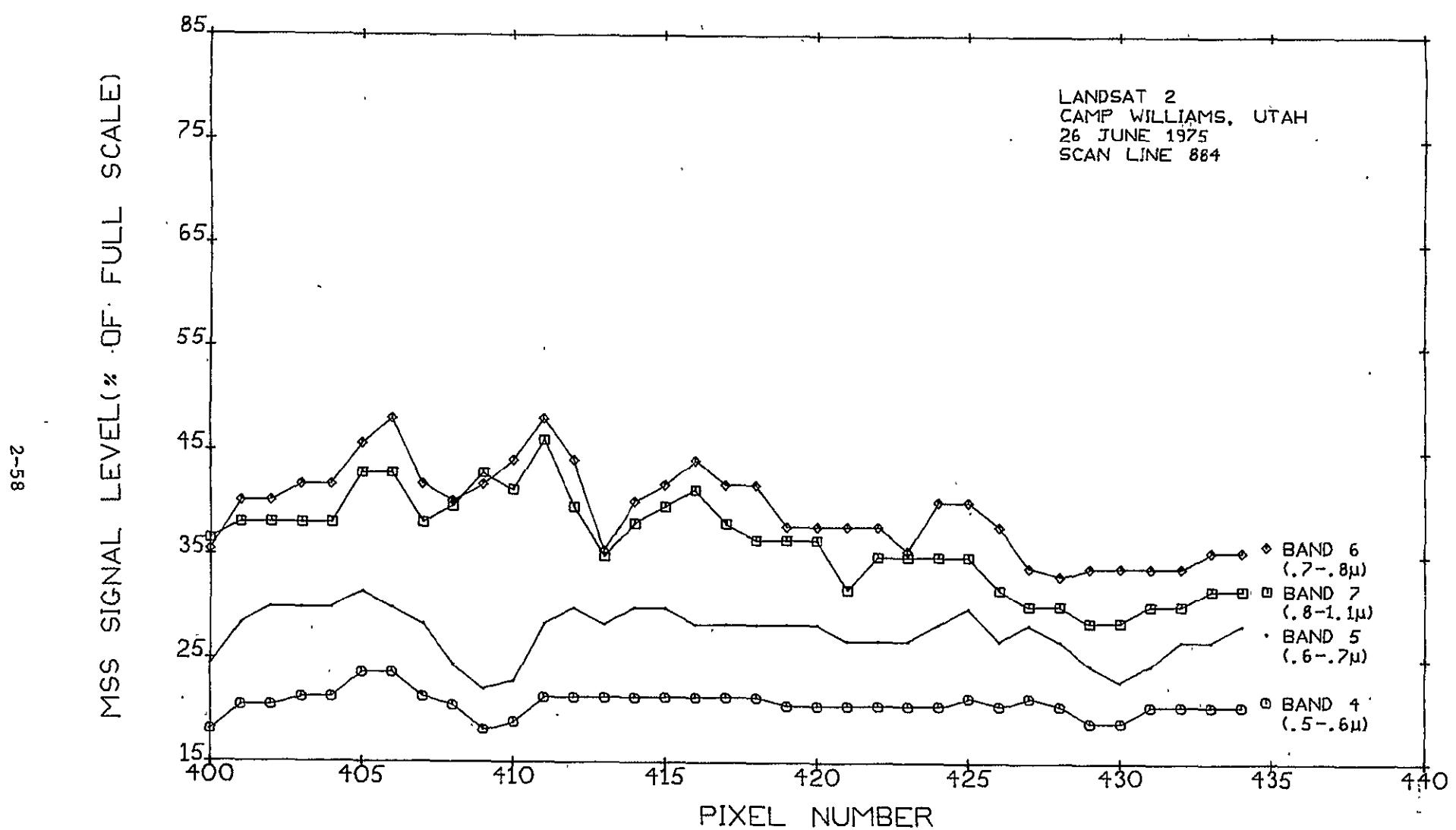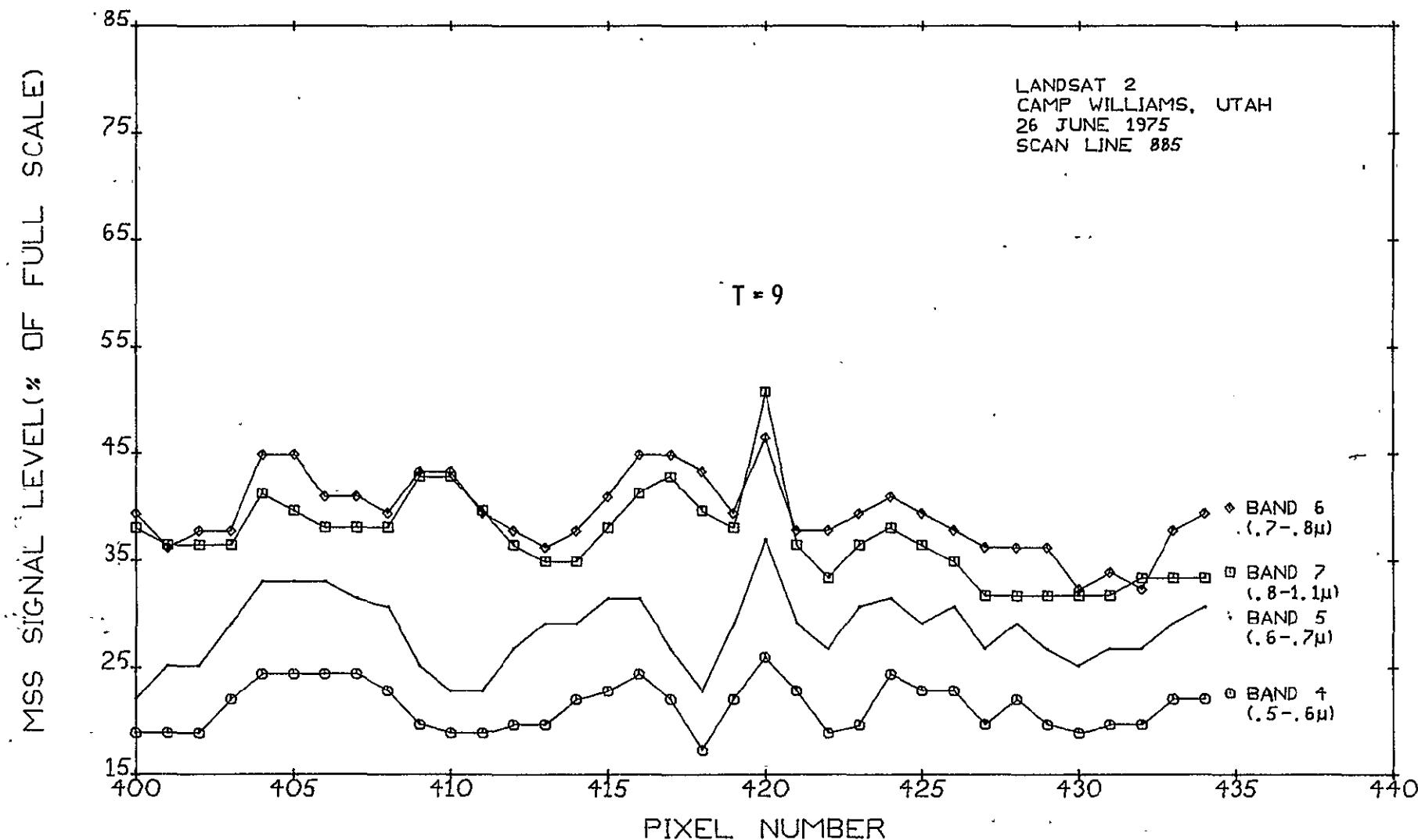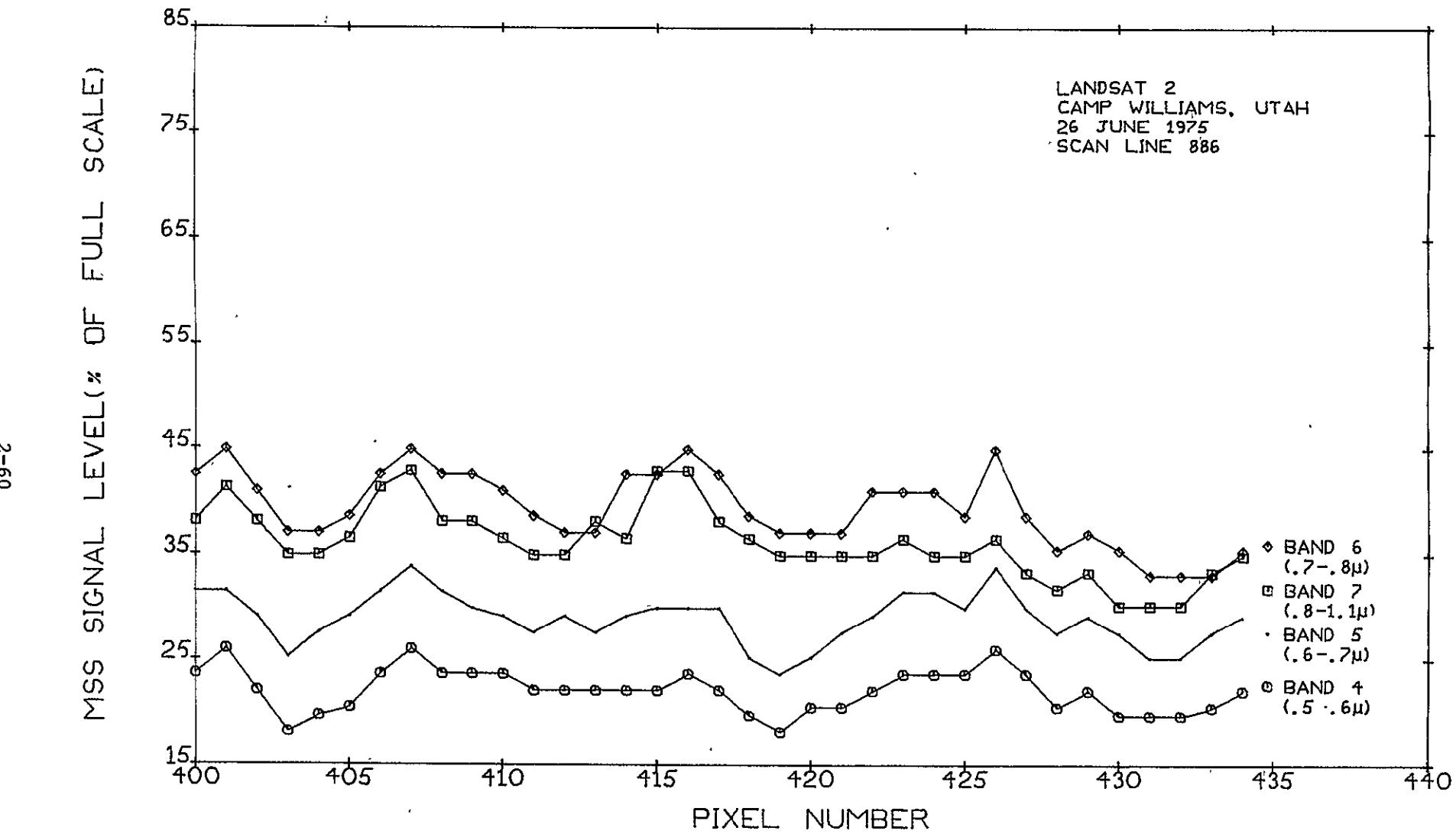
Figure 2-32

Figure 2-33

2.5   COMPARISON OF THEORY AND EXPERIMENT

2.5.1 Accuracy of Predictive Model

The accuracy of the theoretical pulse amplitude model (Equation 2-16) was estimated separately for each of the MSS spectral bands (i) in terms of the average values obtained for the ratios of the experimental to theoretical pulse amplitudes (SRi). The SRi values given in Tables 2-4 through 2-7 are recompiled in Table 2-8 as a function of experiment number and the searchlight designation. The SRi values for the search-lights identified by an asterisk were excluded from the averaging process for one or more of the following reasons: (1) the exact value of the experimental pulse amplitude could not be determined because of satu-ration; as indicated by a $>$ sign; (2) the CCT tape data was considered to be unreliable, as was the case for experiment number 5; (3) the ex-perimental pulse amplitude was either abnormally high or abnormally low in one or more of the channels, based on an arbitrary 50 percent dis-crepancy criterion, as was the case for the east light of experiment number one, the NE light of experiment number six, and lights 7 to 9 of experiment number 7. There are a number of factors which could have accounted for such anomalously low or high results, but which could not be either conveniently controlled or identified after the fact. These factors include total or partial light failure, differences in the actual $I_o(\theta,T)$ profiles between the many lights used, anomalous point-ing errors, an anomalously low or high contribution from the background noise (which was quite high for the hilly sagebrush terrain of experi-ment number 7), and the possibility of MSS data collection and/or CCT conversion errors.

The average SRi values of 1.08, 1.05, 0.97, and 1.10 shown in Table 2-8 were therefore based on the experimental signatures from 10 xenon searchlights. The monotonic decrease in the corresponding stand-ard deviation (0.26, 0.22, 0.21, and 0.15) with increasing wavelength is consistent with the observed increase of pulse amplitude (and thus signal to noise) with increasing wavelength, as predicted by the theoretical pulse amplitude model. Part of the variation in the experimental data could also be attributed to undetermined variations in the actual verti-cal optical thicknesses of the atmosphere in one or more of the wave-

2-61

TABLE 2-8

SUMMARY OF EXPERIMENTAL/THEORETICAL
RATIOS FOR SEARCHLIGHT PULSE AMPLITUDES
(*Data Excluded From Estimates of Average Values)

Exp. No.	Light	PCF	SR4	SR5	SR6	SR7
1	E*	1.00	–	–	–	–
1	W*	1.00	>0.99	>0.86	>0.74	>0.54
2	1	1.04	1.22	1.33	1.19	1.06
3	1	1.04	0.89	0.80	0.73	0.98
4	1	1.03	1.29	1.31	1.05	1.02
5	NE*	1.00	–	–	0.47	0.42
5	SE*	1.03	–	–	0.40	0.44
5	SW*	1.01	–	–	1.15	>1.14
6	NE*	1.01	1.94	>1.79	0.98	>1.23
6	SE	1.01	1.46	1.19	0.96	1.20
7	1	0.94	1.33	0.88	0.67	1.00
7	2	1.05	1.00	1.15	1.14	0.90
7	3	1.00	0.53	0.72	0.71	1.11
7	4	1.01	0.86	0.78	0.81	1.02
7	5	1.07	1.19	1.25	1.21	1.30
7	6	1.20	1.00	1.07	1.18	1.41
7	7*	1.00	–	–	–	–
7	8*	0.94	0.36	0.65	0.47	0.53
7	9*	0.84	0.46	0.60	0.71	1.04
Averages:		1.06	1.08	1.05	0.97	1.10
STD DEV (±)		0.06	0.26	0.22	0.21	0.15

length bands) from experiment to experiment. Any descrepancy between the actual and published values of any of these optical thicknesses, on the other hand, would be expected to show up as a fixed bias or offset, which would be reflected in a consistently high or low value for the SRis and thus their averages. An additional source of variation in the data can also be attributed to a small but finite amount of 2400 hz ripple that was present in the radiation from the AN/TVS-3 searchlights. This should have been faithfully reproduced by the 50,000 hz bandwidth of the MSS detector/amplifiers and resolved (or stopped) by the 0.4 microsecond sampling interval (or shutter duration). The 2400 hz ripple results from the fact that the "d.c." discharge of the xenon lamp is sustained by an unfiltered full-wave rectified current from a 400 hz, three phase power supply. Measurements of the intensity ripple at 0.52, 0.7 and 0.9 microns revealed fractional variations, about the mean intensity of $\pm$ .09, $\pm$ .13 and $\pm$ .08 respectively. Since the searchlight intensity variations associated with the ripple were statistically independent of the other sources of intensity variation, it can be argued that the contribution of such variations to the total standard deviation of the experimental results was less than 10 percent of the values obtained for channels 4 and 7 and less than 23 percent of the values obtained for channels 5 and 6.

Thus, on the basis of the acceptable data from 10 xenon searchlight signatures, it appears that the theoretical pulse amplitude model provides a satisfactory and slightly conservative basis for predicting the pulse amplitude of a xenon searchlight landmark in the near IR channel of an orbiting MSS. Consequently it was decided to use the theoretical pulse amplitude model, as it stands, for the purpose of selecting a xenon searchlight that would be suitable for an EOS MSS. This selection is discussed next.

2.6 SELECTION OF A LOW POWER XENON SEARCHLIGHT FOR EOS MISSIONS

2.6.1 Calibration Intensity Considerations

The present design specifications for the EOS MSS place an upper limit of 43 microradians on the IFOV of the first four MSS channels, with a design goal of 25 microradians. Apart from this, the first four wavelength channels of the EOS MSS should be optically equivalent to the four wavelength channels of the Landsat MSS, which have an IFOV of 86 microradians. The bolometric calibration radiation intensity (I_o^*) required to assure a given minimum pulse amplitude (BPA_4^*) in the near IR channel of the EOS MSS, can therefore be conservatively determined from the experimentally confirmed pulse amplitude model (Equation 2-16) as

$$I_o^* = BPA_4^* \, (\theta N_D)^2 / F_4', \qquad (2-25)$$

where I_o^* is the minimum intensity over a rectangular 1.5 by 6.0 degree portion of the beam at a calibration distance (R_o) of 62 meters, and F_4' is the channel constant for an MSS altitude of 700 km. Since the mean altitude of the EOS orbit is presently specified as 700 km, the channel constant (F_4') in Equation 2-25 is greater than that for the Landsat MSS by the factor $(916/700)^2=1.712$. Inserting $F_4'=1.712F_4=6.712$, and $(\theta N_D)^2=(43/25)^2=2.958$ in Equation 2-25 gives the desired numerical relationship between the minimum calibration intensity

$$I_o^* = .441 \, BPA_4^* \qquad (2-26)$$

and the minimum desired band 4 or near IR pulse amplitude. Comparison with Equation 2-24 shows that, for a given near IR pulse amplitude, the minimum calibration intensity required for an EOS searchlight landmark is a factor of 6.8 times smaller than that which would be required for a Landsat searchlight landmark. The AN/TVS-3 searchlights that were used in the Landsat searchlight landmark experiments, at only 75 percent of their maximum power rating (15 kw vs. 20 kw (max)), were therefore much too powerful, and hence costly, to be considered for an EOS searchlight landmark station (SLS).

In order to determine the minimum calibration intensity actually required for an EOS searchlight landmark, it was first necessary to determine a realistic value for the minimum pulse amplitude (BPA_4^*) that could be reliably detected in the digital CCT data. For this purpose, a digital Xenon Searchlight Landmark Detection (XSLD) algorithm was developed and tested using the CCT data obtained from the Landsat/Searchlight experiments.

2.6.2 <u>Characteristics and Performance Results of an Automated</u>
       <u>Xenon Searchlight Landmark Detection Scheme</u>

The XSLD algorithm performs basically as a xenon searchlight signature filter. The filter processes CCT data over a specified line-pixel data array, looking for narrow pulses, in all four bands, which exceed a set of specified amplitude thresholds and which comply with the known spectral characteristics of a xenon searchlight signature. The experimentally verified enhancement of the near IR pulse amplitude, due to the pronounced "Xenon Flare" (discussed in Section 2.3) was found to provide a highly effective basis for discriminating between low level xenon searchlight signatures and the variety of low level solar radiation pulse signatures that are present in the MSS imagery data. Experimentation with the CCT data showed that optimum selectivity and noise rejection was obtained by requiring that the channel 7 pulse amplitude be greater than 1.2 times the channel 6 pulse amplitude.

The sensitivity of the filter was then determined by increasing the minimum pulse amplitude requirements (thresholds) until a total rejection of erroneous pulses was achieved for at least 200,000 data points (pixels) associated with four 50,000 line-pixel data arrays taken from four separate and particularly noisy portions of the scenes from four different searchlight experiments. The pulse amplitude sensitivity of the filter, as defined by the resulting pulse amplitude threshold for the near IR channel, was thus found to be seven percent (of full scale).

Proper (positive) operation of the filter was verified during the selectivity tests by insuring that one of the four 50k data blocks used in the testing contained the eight xenon searchlight signatures generated

in experiment number 7. Positive filter operation was thus verified by observing that the filter automatically identified and flagged the correct scan line numbers and pixel numbers corresponding to all eight of the xenon searchlight signatures contained in the data (see Figure 2-29, 2-30, and 2-32). The pixel number of a pulse, as such, was consistently defined by the maximum channel 7 pixel intensity, or in the unlikely event of a flat top pulse (consisting of two equal channel 7 pixel intensities) by the pixel number representing the first channel 7 pixel intensity maximum.

2.6.3 Searchlight Selection

Using BPA_4^* = 7 in Equation 2-26 gives a value of 3.1 (watts/ meter^2) for the minimum calibration intensity (I_o^*) of a xenon search-light that could be utilized in an EOS searchlight landmark station. From a practical point of view, however, allowance has to be made for an occasional 50 percent decrease in the recorded pulse amplitudes due to the phenomenon of detector sharing (discussed in Appendix A) with additional allowances for possible decreases in the beam intensity it-self, due to ageing and/or contamination of the searchlight optics, and/or possible increases in the optical thickness of the atmosphere. All in all, it would not be unreasonable to consider a design calibration intensity specification of four times the absolute minimum (I_o^*), cor-responding to a nominal, theoretical, channel four pulse amplitude of 28 percent of full scale. This requirement was found to be adequately satisfied by a commercially available, 4 kw, xenon searchlight (trade-named Xenospot). Calibration intensity measurements, made without the benefit of an optimally designed beam spread lens, yielded a minimum calibration intensity, over a 1.5 by 6.0 degree cone, of 13 watts/ meter^2 (4.2 I_o^*). Based on discussions with the manufacturer it appears that a xenospot calibration intensity design goal of 20 watts/meter^2 (6.5 I_o^*) would not be at all unrealistic. Thus, from the foregoing theoretical considerations and experimental findings, it appears that the use of a xenospot xenon searchlight in an EOS SLS could be expected to generate a nominal landmark pulse of between 30 and 46 percent of the full scale range available to the near IR channel of the EOS MSS. This should be more than adequate to insure an extremely high degree of landmark detection reliability and station integrity.[12]

SECTION 3

PRELIMINARY CONSIDERATIONS RELATING

TO THE DESIGN, IMPLEMENTATION, AND

OPERATION OF EOS SEARCHLIGHT

LANDMARK STATIONS (SLSs)

3.1   INTRODUCTION

The feasibility of generating readily detectable surface position
marker pulses, in the multispectral scanner (MSS) imagery data from an
earth observation satellite (EOS), has been advanced theoretically and
confirmed by means the Landsat/Searchlight experiments reported in
Section 2. The motivation for this work, as described in Section 1,
was based on the findings of a Landmark Utilization Study[1] which sug-
gested that ground truth data of this nature can be exploited, in com-
bination with star measurement data, to determine the orbital ephemeris
of an EOS (thus easing the burden now placed on ground tracking stations),
and to improve the accuracy of both the EOS attitude control system and
the geographic mapping process. The expected technical benefits and
advantages of such a program need to be evaluated however in the light
of the overall cost for the implementation and operation of a suitable
network of EOS Searchlight Landmark Stations (SLSs). This cost would
of course include the cost for the initial design and constuction of a
prototype SLS and its qualification testing, as well as the subsequent
generation of production engineering design drawings and finally the
actual fabrication and installation of the total number of SLSs required
for the landmark grid. Contractors are understandably reluctant to offer
even as much as a guess as to what they think the total cost of such
vaguely defined tasks might be. This section of the ALIS report is there-
fore concerned not with the generation of realistic cost estimates, but
with the generation of a more detailed description of an SLS and the
specific tasks that would have to be undertaken in connection with the
implementation of a useful SLS network for the EOS program. The approxi-
mate costs of components and tasks which can be reliably estimated are
noted, but it will be clear that they represent only a small part of the
total implementation cost. It was originally hoped that this phase of the
ALIS study would result in a rough, first cut, ball park estimate for
the overall implementation cost, but it has become increasingly clear

that this can only be reasonably accomplished through the generation of (and the responses to) RFQs for the major tasks. The purpose of this phase of the ALIS study is therefore to clarify the specifics of those major tasks to which such RFQs would be addressed, and in doing so to provide a more detailed assessment of the total magnitude of an SLS implementation program.

An assessment of the approximate distribution and the number of SLSs that would be required for a landmark utilization program is generated in Section 3.2. Section 3.3 describes the presently envisioned theory of operation of a single SLS in terms of a preliminary conceptual reference design, and Section 3.4 discusses the practical problems of SLS site selection and the acquisition of land and/or leases for such. Section 4 then summarizes the conclusions that have been reached in the ALIS study and the recommendations for future studies and RFQs that are needed to obtain realistic cost estimates for the overall implementation task.

3.2   ASSESSMENT OF SLS GRID SIZE

The analytical results obtained in the Landmark Utilization Study[1] have indicated that the locations of the landmarks could be restricted, for the most part, to the continental U.S., with a frequency distribution sufficient to insure the observability of only one or two landmarks per orbital pass. A seemingly reasonable SLS distribution, is illustrated in Figure 3-1 in which three SLSs are distributed along most of the 42 EOS ground tracks in the U.S., to provide a nominal redundancy of between one and two sightings per orbital pass over the U.S., using a total of 114 SLSs. A redundancy of two sightings could very well be excessive, in many instances, and future LUS studies would have to be undertaken to determine the statistical variations of the cloud cover along the EOS ground tracks, and also, the minimum number of sightings per orbit that could actually be tolerated for the kinds of applications and accuracies desired. In view of these considerations, it might be reasonable to develop fabrication and installation oriented RFQs on the assumption that 100 SLSs would be required.
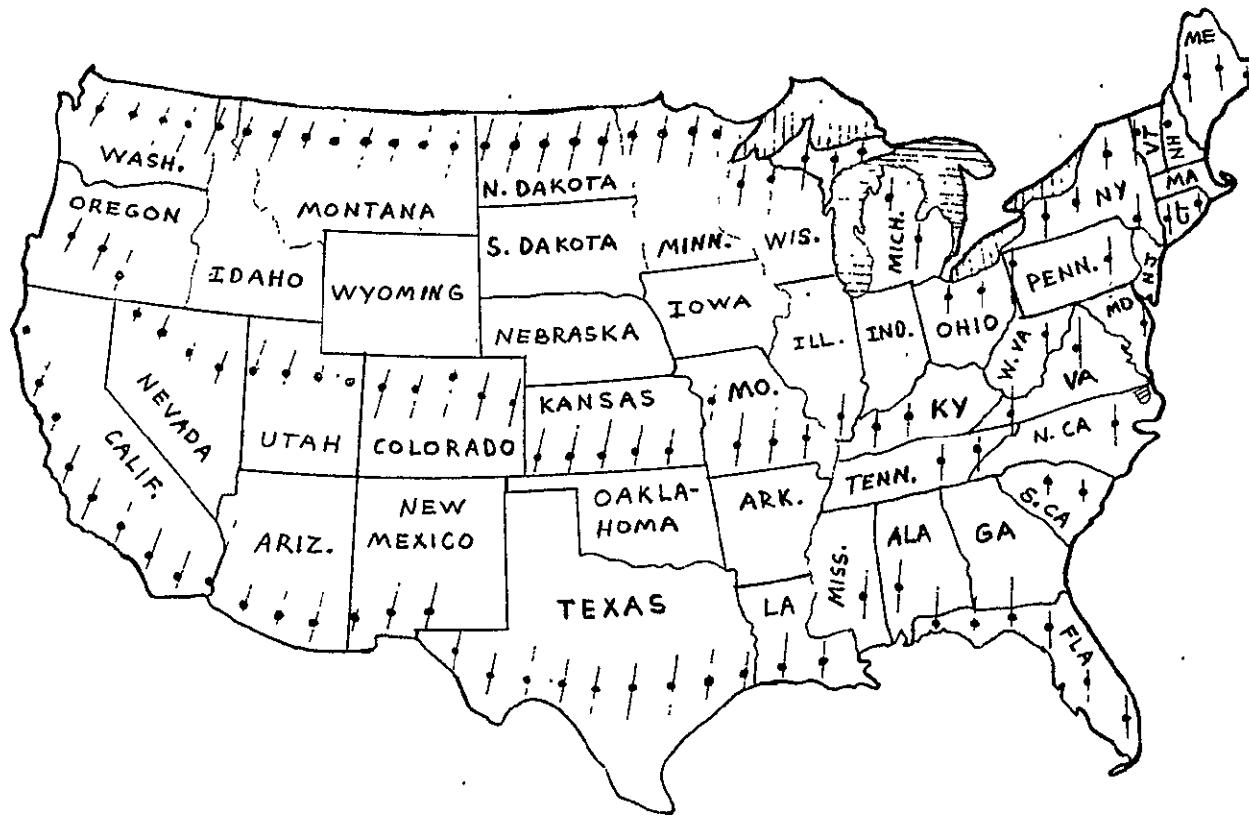
Figure 3-1 Approximate Distribution (ᐧ) of 114 Searchlight
Landmark Stations. Slashed Lines Indicate
Directions of EOS Ground Tracks.

3.3   SLS CONCEPTUAL REFERENCE DESIGN

This Section provides a qualitative description of the presently
envisioned construction and operation of an SLS, consistent with the
operational guidelines discussed in Section 3.3.1. The description, as
such, provides only a preliminary SLS conceptual reference design,
which could possibly serve as the basis for generating an RFP to obtain
a detailed engineering design and realistic cost estimates for the con-
struction of a prototype SLS and also for the fabrication, installation
and check out of 100 production models.

3.3.1 Operational Guidelines

For the purposes of this study, it was assumed that the EOS satel-
lite design will include provisions for the continuous transmission
(over the U.S.A. at least) of an omni-directional carrier signal, which
can be employed to activate each SLS one or two minutes before the
satellite passes over the SLS. Activation, in this sense, means the
initiation of an automated timing sequence for controlling the start-
up, operation, and shut-down of the SLS. It was also assumed that the
SLS design would include an optional provision for communicating its
identify or station number and its operational status or integrity to
an onboard data collection system (DCS), like that currently employed
in the Landsat spacecraft for collecting and disseminating data from a
variety of earth based data collection platforms (DCPs).[12] In addition,
it was assumed that the SLS design would provide an adequate degree of
protection against potentially harsh environmental factors, including
provisions for an automatic NO-GO or abort in the case that inclement
weather conditions prevail at the time of the flyby.

The basic operating principles and components associated with the
presently envisioned SLS design are briefly described next with refer-
ence to the function block diagram shown in Figure 3-2.

3.3.2 SLS Power Requirements

Primary station power is provided by a 220 volt single phase line
capable of furnishing a peak power load of approximately seven kilowatts
for a period of about six minutes once every 18 days when the search-
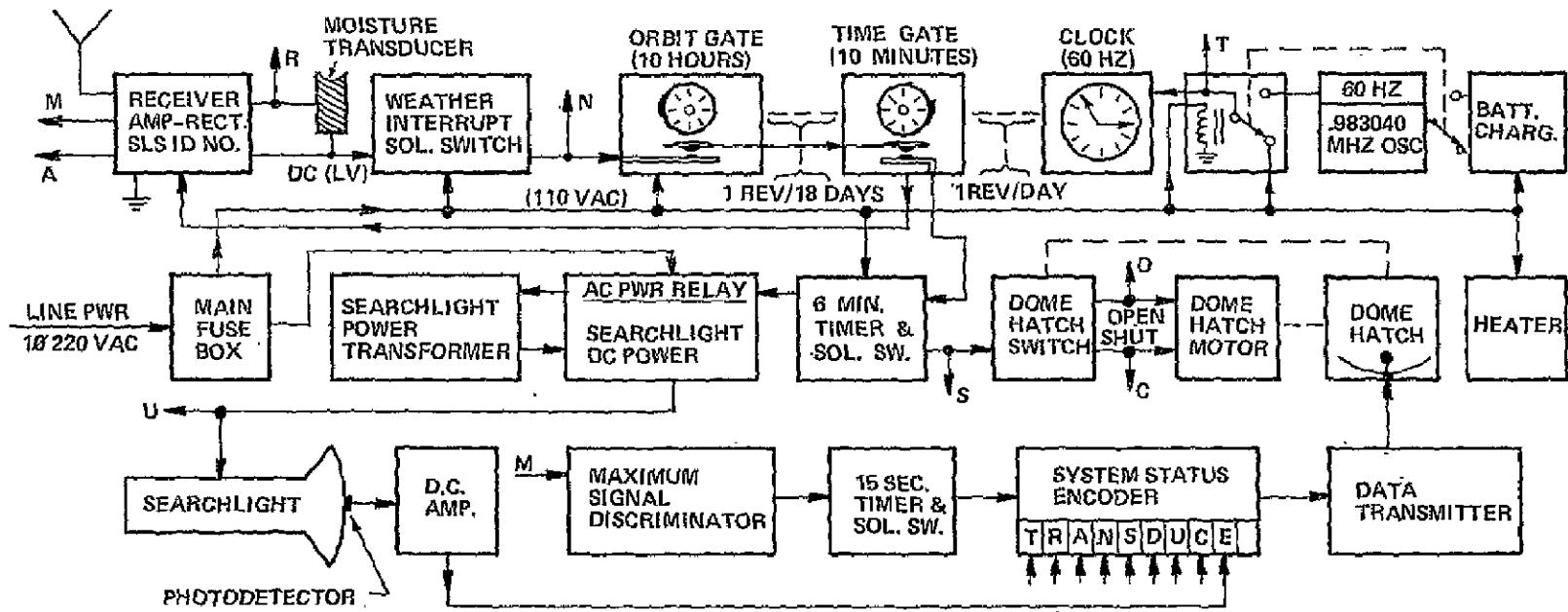
Figure 3-2 Searchlight Landmark Station Block Diagram

light is turned on. An internal transformer (not explicitly shown) is used to provide a 500 watt source of 110 volt power for SLS activation and control components. With the exception of a 14 minute standby and operation period, which occurs only once every 18 days,* the SLS power consumption should be quite small, being only that which would be required to operate a 60 Hz station clock and to maintain a full charge on the clock-drive back-up battery. The power, if any, that would be consumed by the SLS heater is difficult to estimate at this time, since it will depend on both the actual location of the SLS and the operating temperature ranges for its components.

3.3.3 SLS Activation Window

In accordance with the guidelines given in Section 3.3.1, the activation of each SLS in advance of an EOS flyby will be triggered by an omni-directional carrier signal emanating from the EOS. Thus, in order to limit the activation of SLSs during each orbit to only those which lie within the actual ground path of the EOS, and to also maximize the overall efficiency and lifetime of each SLS, the SLS design should include a timing mechanism that prevents electrical power from being applied to the SLS RECEIVER (and all other SLS components) unless the local date and time at an SLS coincide with that for an EOS flyby to within zero days and approximately $\pm$ 5.0 minutes.

A number of possible configurations can be envisoned for such a timing mechanism, and there is a natural tendency to envision a configuration based on the use of modern digital hardware, encompassing a precision digital clock, two preset counters, a permanent memory storage buffer, switching relays and associated d.c. amplifiers, and a back-up battery sufficient to supply the power that would be required to keep all timing components functioning during an extended power failure. The specific problem at hand is considerably simplified however because of the precise 18 day periodicity of successive flybys and the fact that the variations in the local flyby times are controlled and kept within a small fraction of the $\pm$ 5.0 minute activation window.*

---

*These considerations would not be seriously affected by a daily activation for 18 EOSs. See discussion in 3.3.4.

Thus, while an activation window of this size represents a very small fraction of 18 days, it also represents a very generous margin of safety for the nominal timing errors that can be associated with a simple and reliable mechanical gating mechanism, driven by a synchronous 60 Hz electric clock motor.

The basic components and operation of such a timer are illustrated in Figure 3-2. A primary 60 Hz station clock is used to drive a pair of mechanically coupled conincidence gates or switches. The ORBIT GATE switch, being driven at one revolution per 18 days, closes for a period of about 10 hours, centered on the nominal flyby time (T_o^i). T_o^i refers to the ith satellite in a pattern consisting of 2, 3, 6, 9, or 18 EOSs (see discussion at the end of 3.3.4). When this happens, power to the station receiver is then controlled exclusively by the TIME GATE switch, which, being driven at the rate of one (or two) revolutions per day, closes accurately for a period of about 10 minutes, also centered on T_o^i. When this happens, line power is then applied to the station RECEIVER and the SLS is said to be in a STAND-BY condition. The receiver power on/off switches are in parallel with the Activation Gate switches shown in Figure 3-2. Integrity of the station clock during a local power failure is secured by a back-up, battery powered oscillator and a 60 Hz amplifier.

3.3.4 SLS Activation Functions

Detection of the EOS carrier transmission can be said to occur at that instant when the strength of the received signal exceeds a certain threshold value, causing closure of a relay in the receiver and a low voltage d.c. activation signal to appear at the receiver output (R). It is envisioned that the receiver gain would be adjusted so that detection will occur, nominally, when the EOS is approximately two minutes or about 890 curvilinear miles away from an SLS. Following detection of the EOS carrier signal, the activation signal is applied to a MOSITURE TRANSDUCER, designed to block passage of the activation signal if there is a detectable amount of snow and/or rainfall present. Otherwise, the activation signal forces closure of a normally open WEATHER INTERRUPT SOLENOID SWITCH which feeds a low current 110 volt signal (through the now closed activation switches in the Orbit and Time gate components) to activate the six minute station control timer. The circuitry in

this TIMER should be such that once the TIMER is energized it provides full and independent control of the remaining SLS functions, causing line power to be applied to the control timer itself, the searchlight power relay, the dome-hatch drive motor, and the SLS Data Collection Platform components. A Maximum Signal Discrimator circuit is envisioned for restricting the transmission of station integrity data until the EOS is approximately overhead. The SLS response time, for searchlight warm-up and dome-hatch opening, is estimated at 0.5 minutes. Consequently, the combined timing errors associated with the SLS clock, the time gate switch, and the EOS flyby can be as large as + 9.5 minutes and as small as - 4.5 minutes. Nominally, the time gate cam would be offset by two minutes so that the total timing error range is symmetric (+ 7.0 minutes).

Allowance for multiple EOSs, in a symmetric pattern consisting of 2, 3, 6, 9, or 18 EOSs could easily be provided by incorporating 18 individual but adjustable risers or cams in the "18 day" cam that could be easily set, by means of a simple twist-lock action, in either the "out" (activate) or "in" position. The frequency of the standby condition (or activiation window) could thus be manually increased as needed, or as anticipated, to allow for successive flybys every 9, 6, 3, 2 or 1 day(s). In this regard it would be advisable to make the stand-by window equal to the launch window.

3.3.5 SLS Housing

The SLS housing envisioned and illustrated in Figures 3-3 to 3-9 is briefly discussed as follows. Figure 3-3 shows an artists conception of an SLS located in a field. In practice, one half or more of the SLSs would probably be located on top of commercial buildings. The estimated dimensions for the overall SLS and the individual subsections is shown in Figure 3-4. The alignment baseplate shown in Figure 3-5 is prealigned so that when the SLS is installed, with the *'d leg on the *'d mounting bolt, the 6 degree beam spread from the xenospot will be automatically aligned in the cross-track direction for that SLS site. The vertical dimension of the searchlight power supply section shown in Figure 3-6 was configured initially to accommodate the standard three phase power supply which is required for continuous operation of the searchlight. The manufacturer has stated, however, that a smaller (20 inch high),

220 volt single phase power supply would be adequate for the SLS duty
cycle. Figure 3-7 shows the approximate physical arrangement of the
electronic components shown in the block diagram of Figure 3-2, and
Figure 3-8 shows the approximate layout of the housing section contain-
ing the 4 kw xenospot searchlight. Figure 3-9 then shows an approxi-
mate layout of the dome-hatch section with the EOS receiving and data
collection platform transmission antennas. During operation the dome-
hatch is rotated 180 degrees to a full open position as indicated in
Figure 3-8.

3.4 SLS INSTALLATION AND OPERATION COST CONSIDERATIONS

The largest expense associated with the installation and operation
of a national SLS grid would, in all likelihood, be that associated
with the purchase and/or leasing of the land parcels and/or building
spaces on which the SLSs would be located. A realistic estimate for
these fixed and yearly costs could be obtained through a study encom-
passing the following two work statements:

(1) Assuming that 114 SLS sites will be required, and
that the down range or intrack separation between SLS sites
along any EOS ground track must be greater than 300 miles, and
that the offset of any SLS site in the crosstrack direction
must be within $\pm$ 10 nautical miles of the nominal ground track,
determine the optional (most cost effective) distribution of
SLS sites with regard to a realistic assessment of the RELATIVE
(as opposed to absolute) purchase costs and leasing options for
the various candidate types of SLS real estate within the total
SLS location zone defined by the intrack and crosstrack con-
straints noted above.

(2) From the most effective distribution of SLS sites de-
termined in (1) which is based on RELATIVE real estate purchase
and leasing costs, select a representative sample of 15 potential
SLS sites and, through actual negotiations with the property
owners, determine the actual purchase and leasing costs for the
15 sites selected, and then weigh these results in an appropriate
manner to obtain a realistic ($\pm$ 10 percent) estimate for the
total purchase and leasing costs for the entire grid of 114 SLS
sites.

Additional factors that would have to be included in both of the above tasks would be (a) the cost of bringing in a 220 volt, single phase power line to the test sites, (b) the yearly electric power costs, (c) the accessability of the site locations to major roads (for the purposes of installation, repair, and surveying), (d) the costs for access right-of-ways where necessary, and (e) the total cost for an accurate survey of the 114 SLS locations.

U.S. ·GOVERNMENT
PROPERTY

NASA EOS
SEARCHLIGHT
LANDMARK STATION
NO. 85
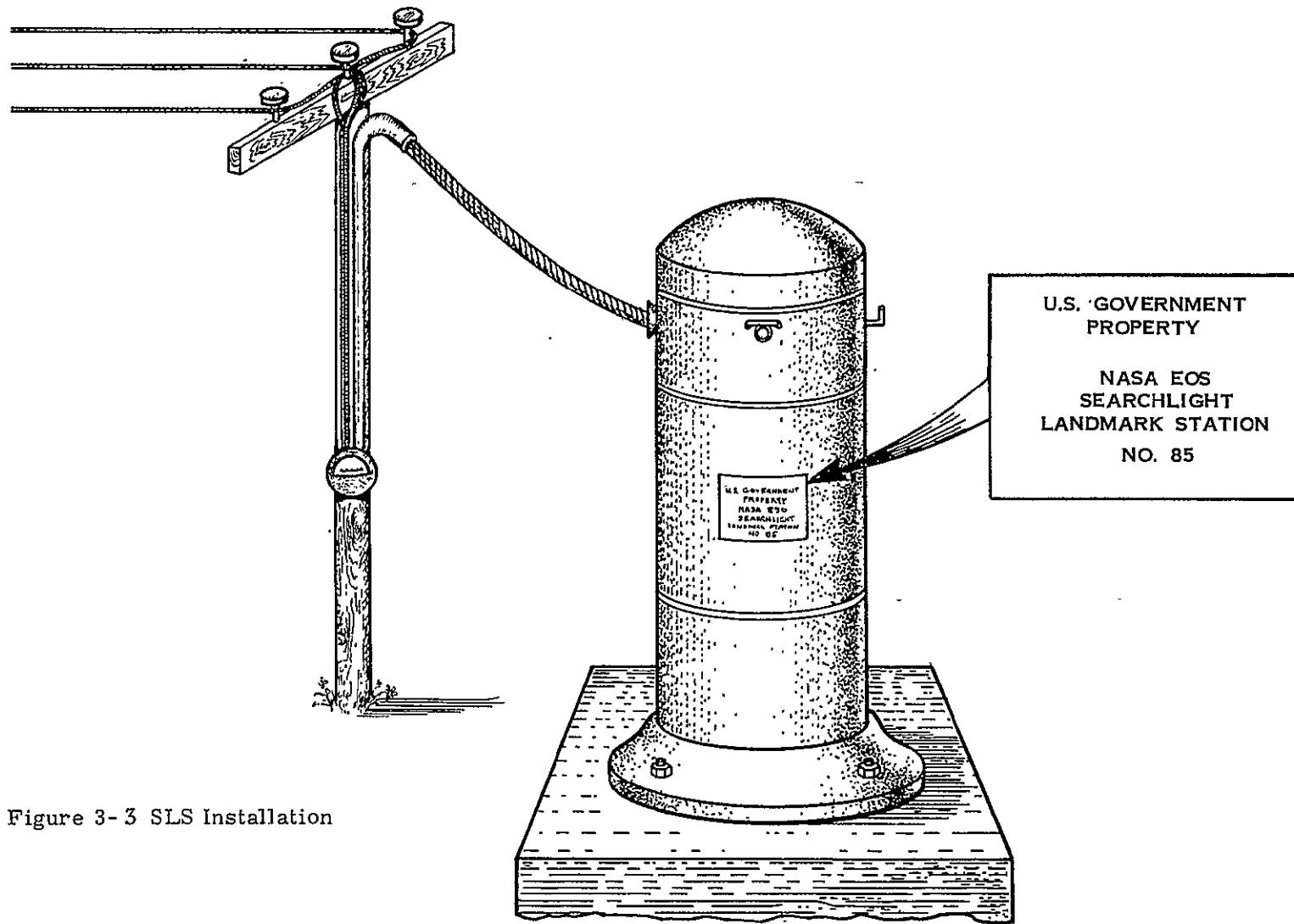
Figure 3- 3 SLS Installation

DOME HATCH
SECTION D

10"

SEARCHLIGHT

27"

SECTION C

ELECTRONICS

18"

SECTION B

3 FT

SEARCHLIGHT

39"

POWER SUPPLY

SECTION A

MOUNTING
BASE PLATE

8 FT
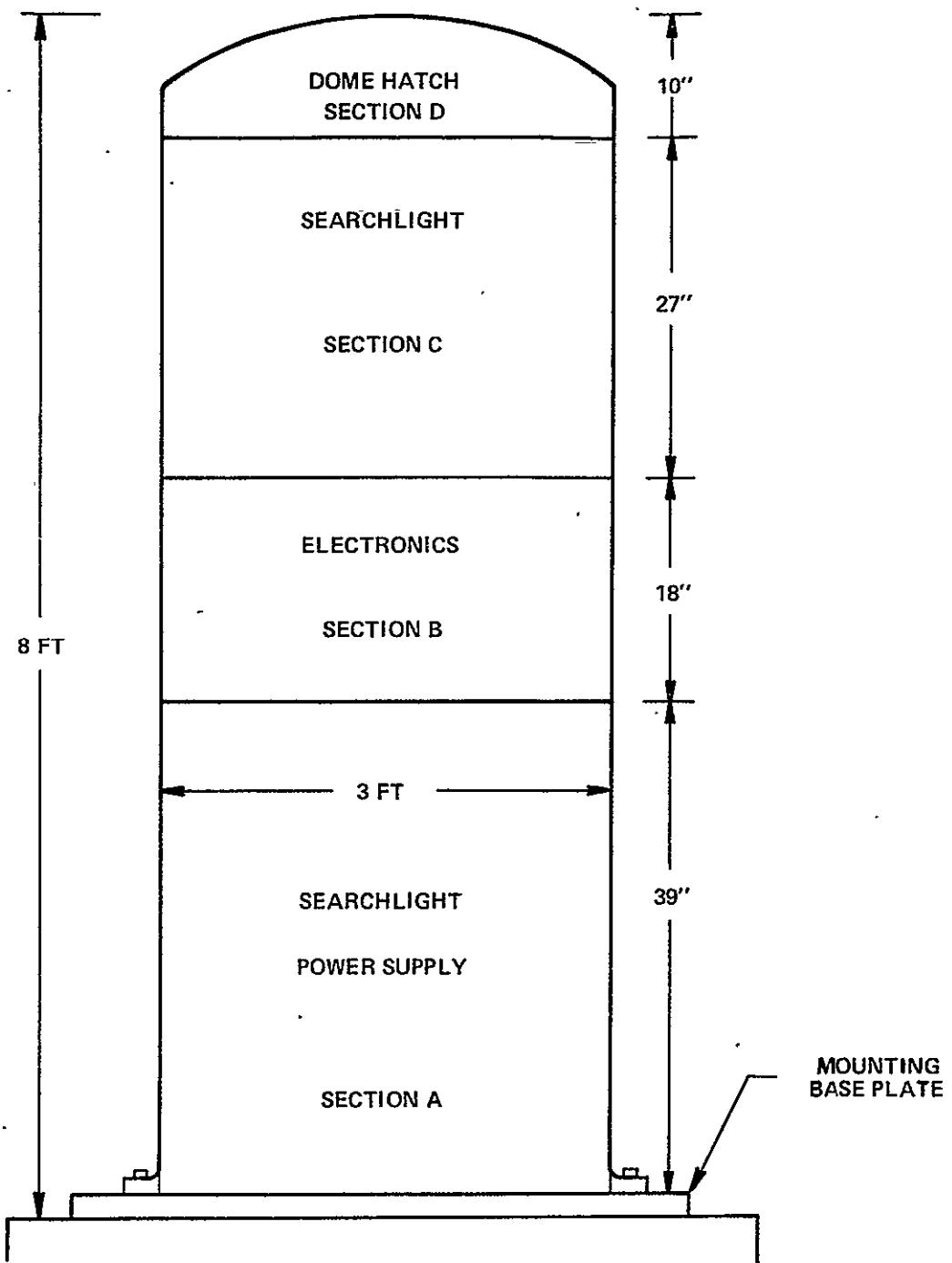
Figure 3-4 SLS Dimensions (1/12 Full Scale)

ALIGN XX.X DEG. N.E.

SLS SLAB 5′ x 5′ x 3′

SLS BASE PLATE 2″ x 50″ DIA.

36″

60″
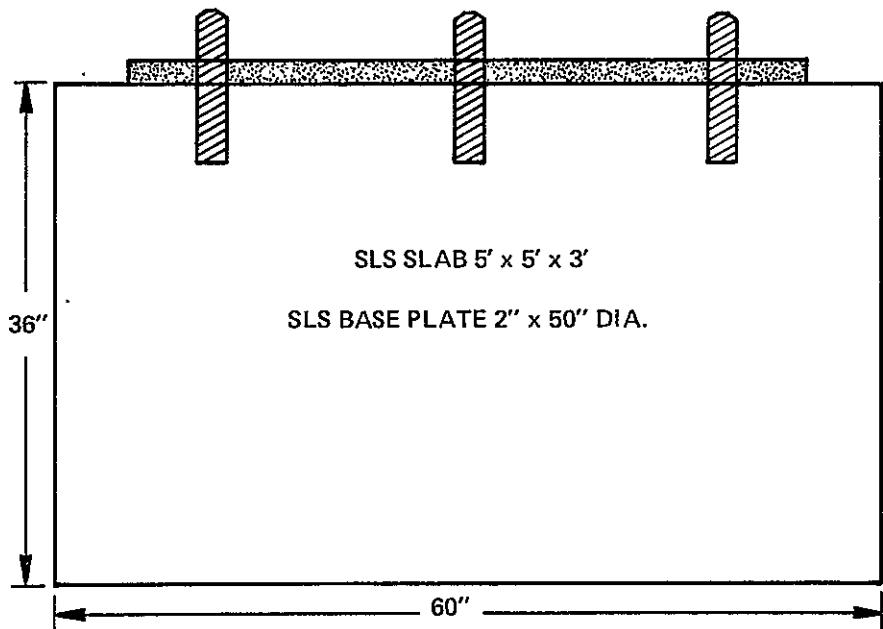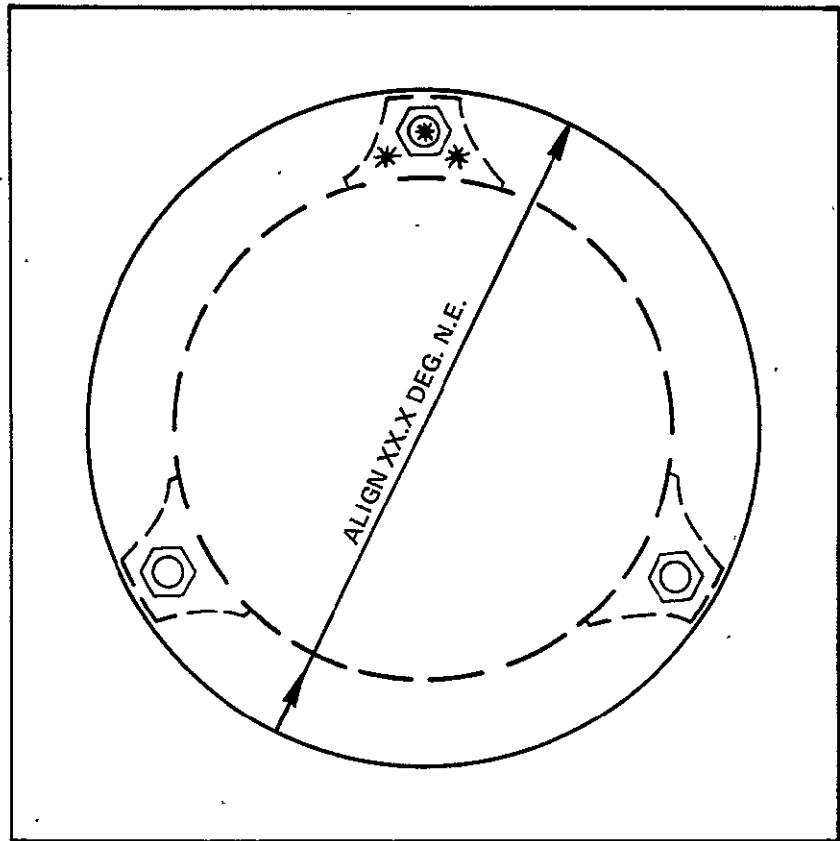
Figure 3-5 SLS – Slab and Baseplate (1/12 Full Scale)

DC POWER

TO SEARCHLIGHT

1φ   220 VAC

AC POWER RELAY

OUT   IN   ON/OFF

SEARCHLIGHT
POWER

RELAY
TRANSFORMER
RECTIFIER

39"

36"
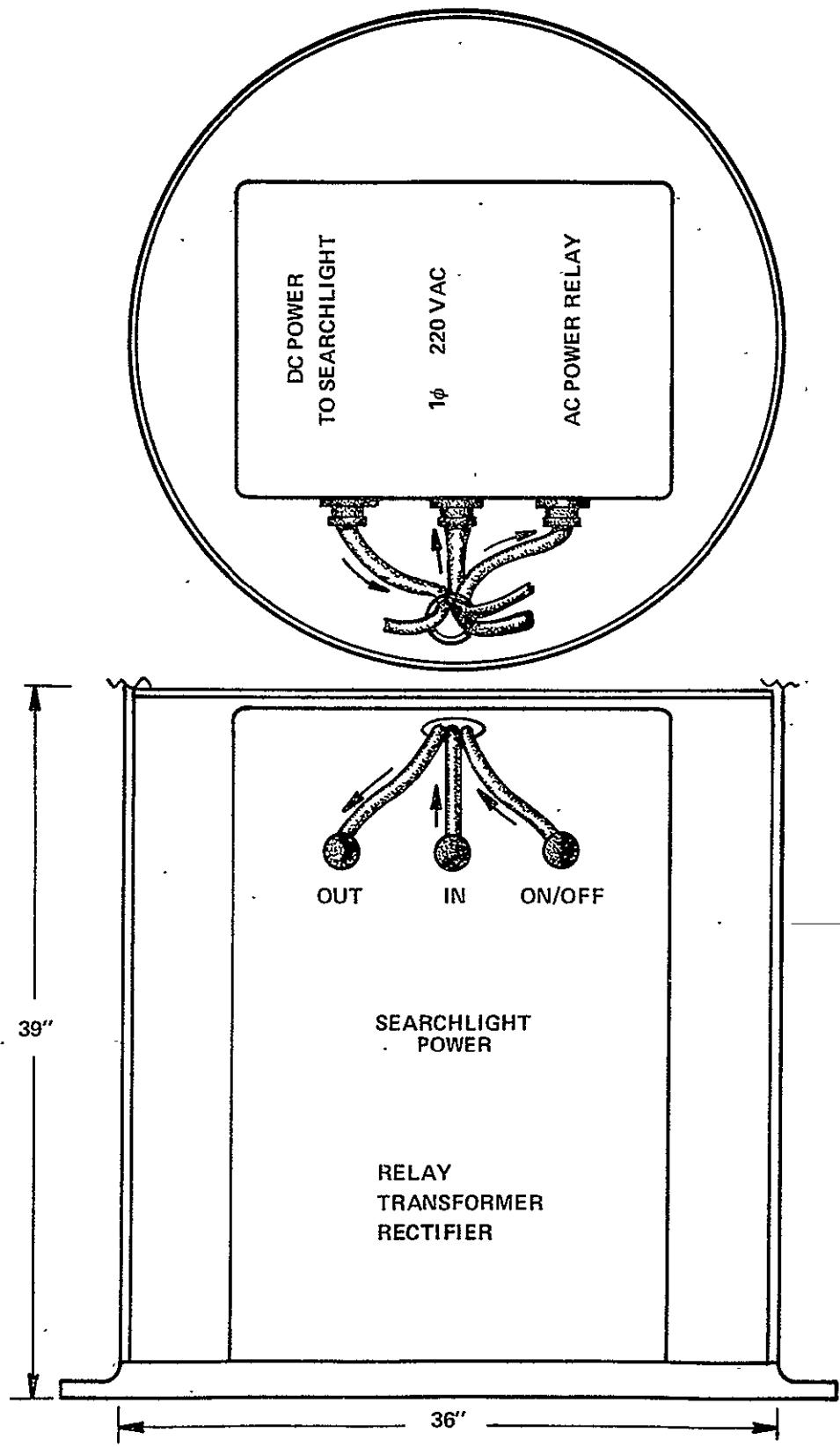
Figure 3-6 SLS - Section A (1/8 Full Scale)

HEATER

BATTERY AND CHARGER

SYSTEM STATUS ENCODER/XMTR 15 SEC TIMER/ SW

LINE PWR BOX

REC/AMP/RECT MAX SIG DISCR SLS ID NO. WEATHER SOL. SW.

DOME-HATCH MOTOR/GEAR AND SW. BOX

.983040 MHZ OSC

60 HZ OUT

SLS CLOCK TIME GATE ORBIT GATE

4 MIN. TIMER SOL. SW.

D.C. AMP

ACCESS DOOR

18"

36"
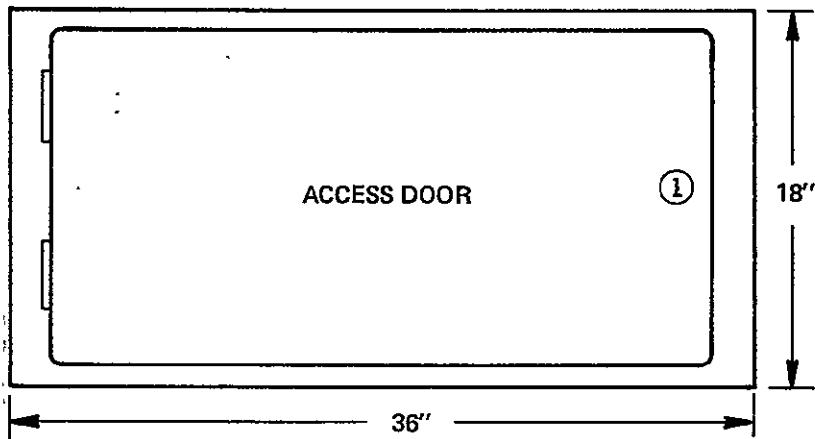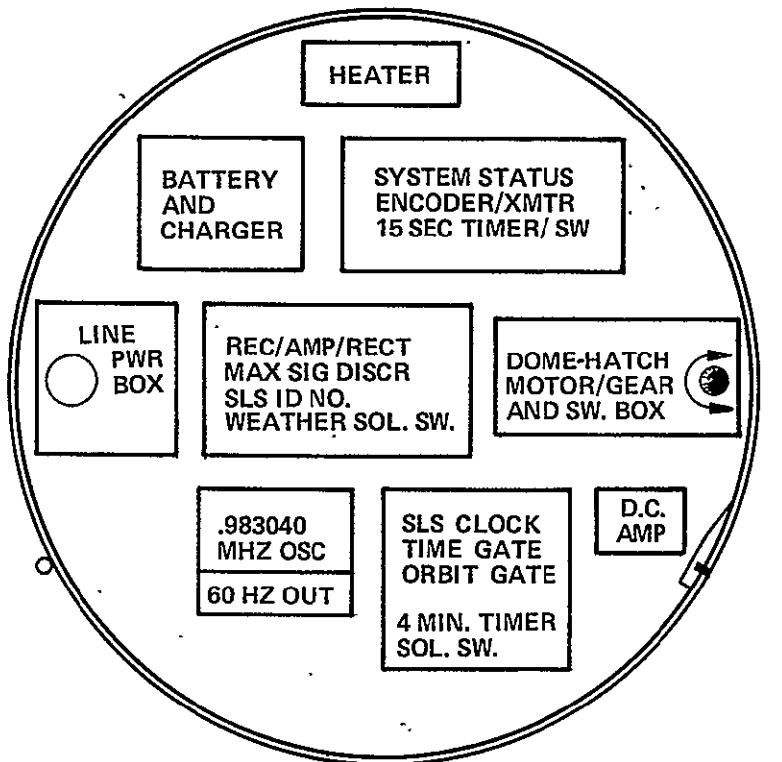
Figure 3-7 SLS - Section B (1/8 Full Scale)

MOISTURE TRANSDUCER

12° SPREAD

1.5° SPREAD

HOIST BRACKET

LINE POWER INLET

4 KW SEARCHLIGHT
(XENON SHORT ARC)

27"

36"
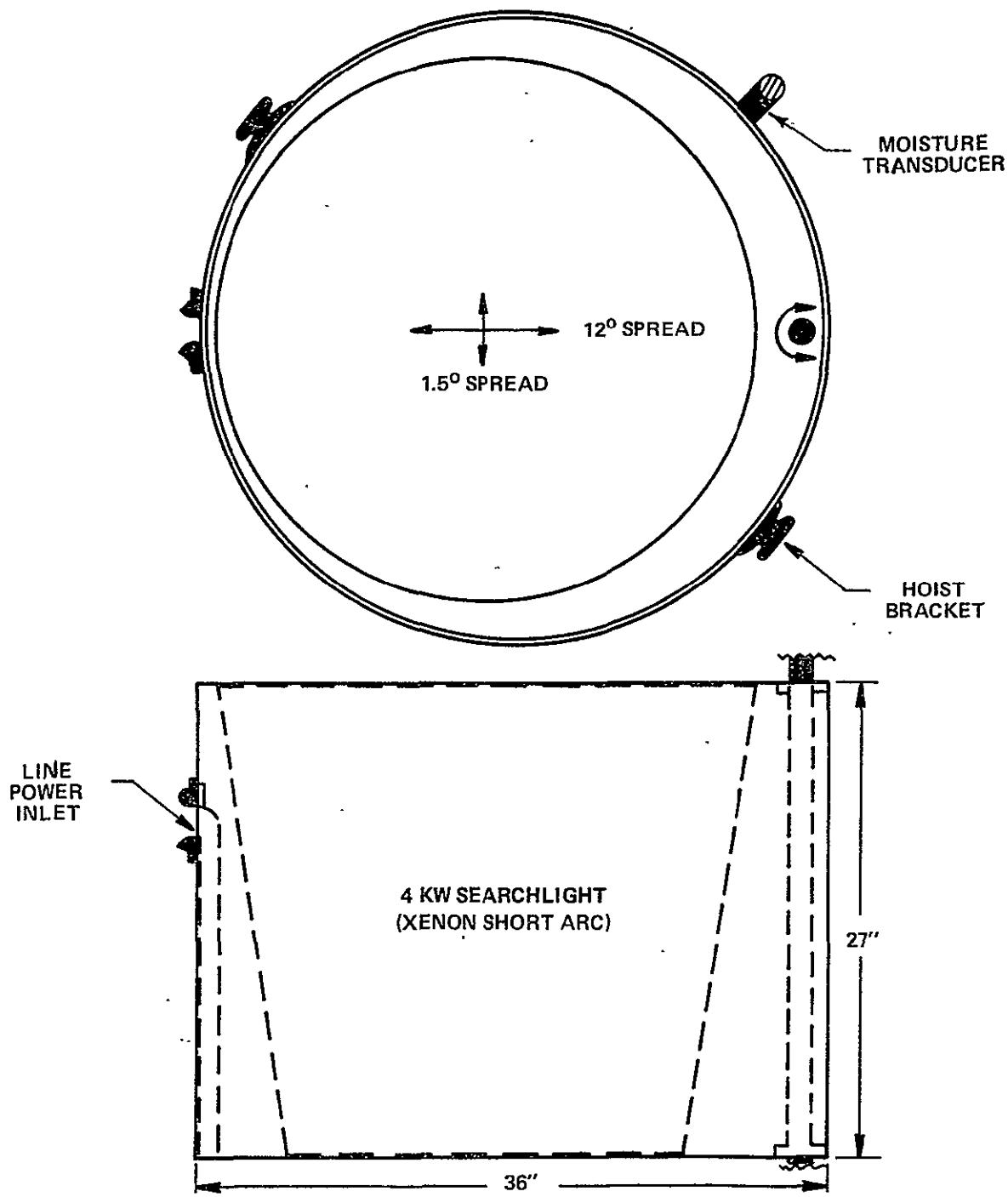
Figure 3-8 SLS-Section C (1/8 Full Scale)

TRANSMITTING
ANTENNA

RECEIVING
ANTENNA

36"

10"

DOME HATCH
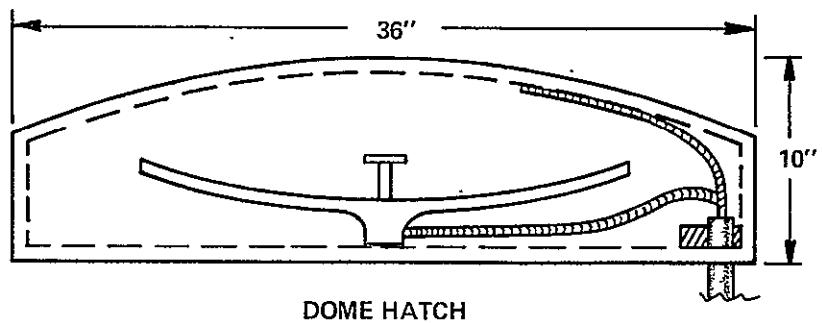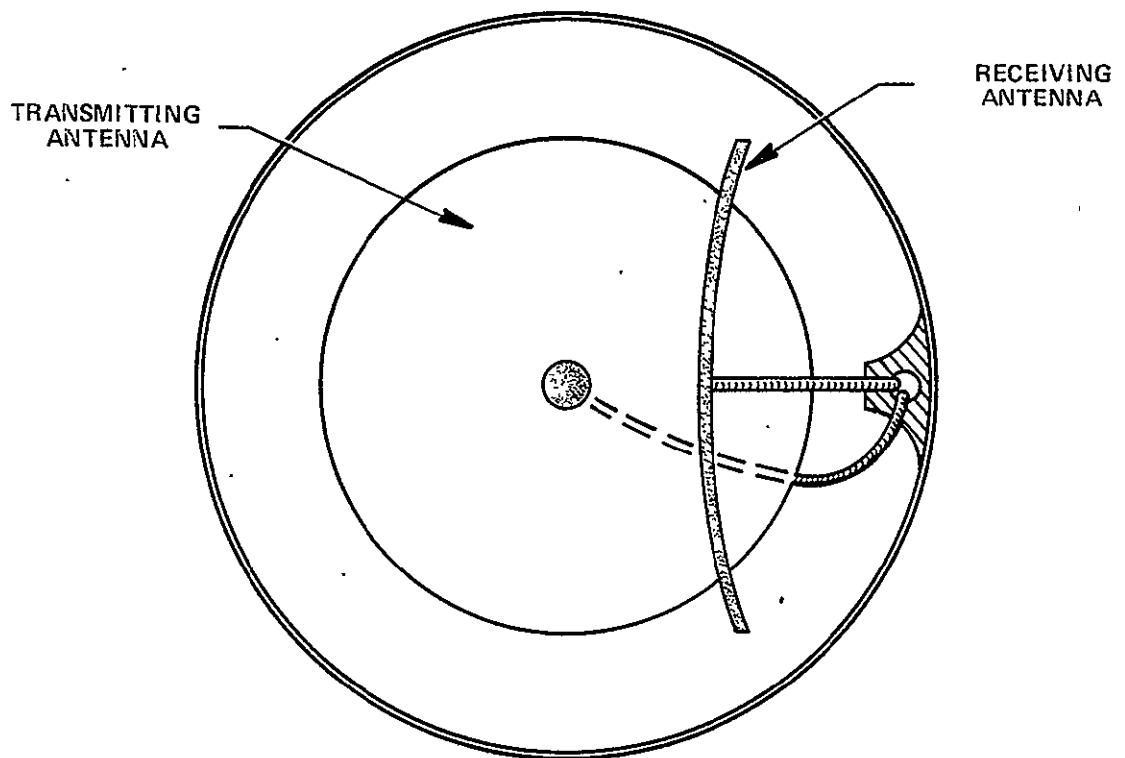
Figure 3-9 SLS - Section D (1/8 Full Scale)

SECTION 4

CONCLUSIONS AND RECOMMENDATIONS

4.1   CONCLUSIONS

The feasibility of generating readily detectable searchlight landmark position marker pulses in the multispectral scanner imagery data from an earth observation satellite has been advanced theoretically and confirmed by means of a series of experiments with Landsat 1 and Landsat 2. And the results were extrapolated to identify a commercially available low power xenon searchlight that would be suitable for an EOS Searchlight Landmark Station (SLS), based on an EOS MSS IFOV of 43 micro radians.

A number of the major tasks that would have to be undertaken in order to carry out the actual implementation of a suitable national grid of SLS were discussed in terms of a preliminary conceptual reference design for an SLS, and an attempt was made to outline the types of future studies that would have to be carried out in order to obtain a realistic assessment of the approximate costs that would be involved in such a program. These studies are summarized next.

4.2   RECOMMENDATIONS

The technical benefits and advantages that the EOS program could expect to derive from the type of Landmark Utilization Program discussed in this report need to be carefully weighed against a realistic estimate for the total expenses that could be expected in connection with the implementation and operation of a national grid of SLS. It is perhaps regretable that such an estimate can not be reliably obtained without further studies, but the nature of the problem is such that realistic estimates simply cannot be generated when such a large gap exists between the general concepts that presently exist and the specifics that have to be identified and properly appraised at a point much closer to the potential suppliers of the hardware products, services, and real estate property that would actually be required. In this regard the following studies are recommended for future consideration.

(1) An extenstion of the Landmark Utilization Study
to establish a realistic distribution for SLSs throughout
the continental U.S. taking into consideration such factors
as cloud cover statistics and the corresponding minimum
SLS redundancy factor.

(2) An RFQ for the preliminary design of a prototype
SLS with realistic ($\pm$ 10 percent) cost estimates for its
fabrication and qualification testing, and for the gener-
ation of engineering production design drawings and the
fabrication and installation of the quantity of SLSs
determined from (1) above.

(3) An RFQ for a study to determine a realistic esti-
mate for the costs that would be associated with the
purchasing and/or leasing of SLS real estate, electric
power hook up, and surveying, as detailed in Section 3.4.

(4) An RFQ for the design and testing of a prototype
near real time xenon searchlight pulse signature detector
for use in an on board detection scheme.

APPENDIX A

STOCHASTIC DEGRADATION OF
BEACON LANDMARK PULSES
DUE TO DETECTOR SHARING
AND DATA SAMPLING

A.1   DETECTOR SHARING STATISTICS

    The maximum amplitude of a given beacon landmark pulse should
occasionally be degraded by as much as 50 per cent due to the fact that
the corresponding power (or number of photons per second) will occasion-
ally be divided·equally between the spectral detectors in two adjacent
rows of the total intrack-field/spectral detector array as illustrated
in Figure A-1.   Referring to Figure A-1, .we note that when a beacon
landmark is sighted, the position of its spot image along the intrack
coordinate of the MSS detector array is determined entirely by the
position which the landmark happens to occupy with respect to the total
intrack field of view (θ_T) at the instant it is sighted.   Thus, because
of the Stochastic variations in the orbital ephemeris and attitude
of·the EOS, it is reasonable to assume that artificial landmark images
will have an equal a priori probability of occurring anywhere along
the intrack coordinate of the MSS detector array.

    The statistics of the pulse amplitude degradation is derived here
for the realitic case in which the maximum spot diameter (D_s) is less
than the linear dimension (L) of each detector element.   The analysis
is facilitiated by assuming a uniform photon flux density over the
spot area $A_s = \pi D_s^2/4$.   With reference to Figure A-1, the parameter FD
(expressed in units of D_s) represents the linear distance by which the
edge of an image spot protrudes into any given detector row.   Since the
occupation space of an in-track detector row is L, the probability that
the edge of an image spot overlaps by a distance between FDD_s and D_s
from either edge is numerically equal to the probability that the cen-
ter of the spot (regarded as point) is located within an enclosed path

IMAGE MOTION ⟶

ROW λ_4 λ_3 λ_2 λ_1

6   1   2   13   14

5   3   4   15   16

SCAN DIRECTION
(NW ⟶ SE)

$f\theta_T$

4   5   6   17   18

$\dfrac{f\theta_D}{8} = L$ ← L →

3   7   19   20

2   9   10   21   22

SPACECRAFT MOTION
(NE ⟶ SW)

1   11   12   23   24

D_S

TIME

DATA SAMPLING PULSES
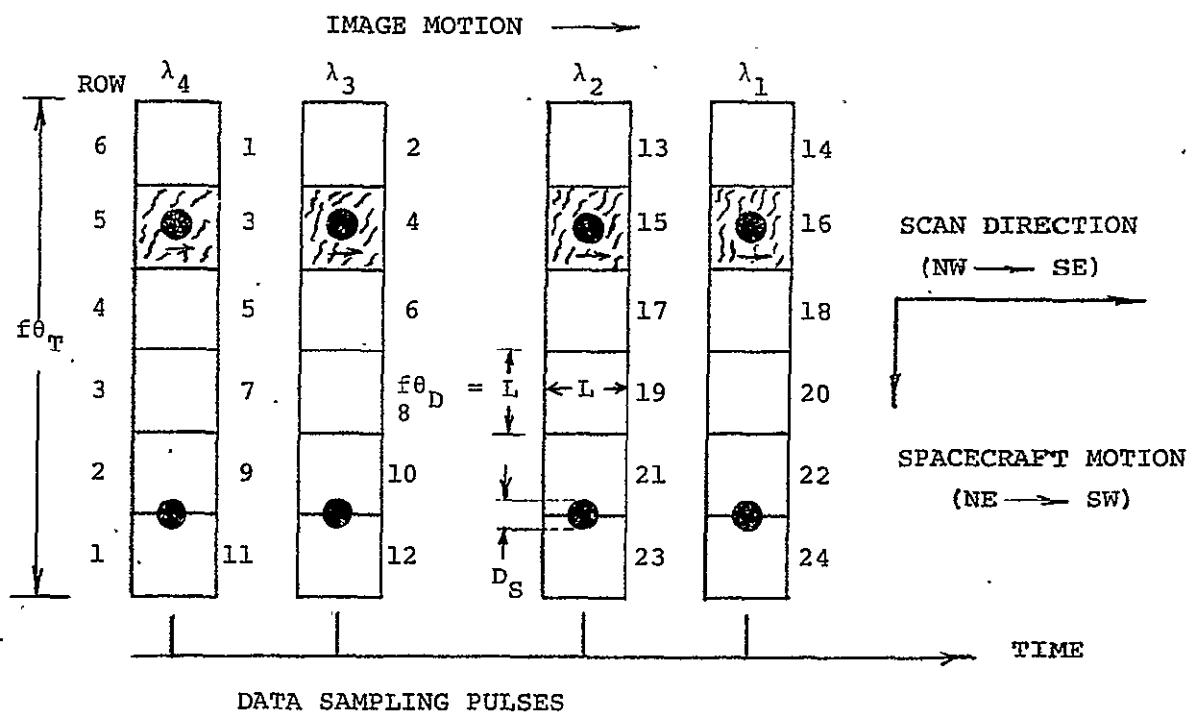
FIGURE A-1   Landsat MSS Detector Array Showing
Sequential Positions and Sampling of
Beacon Landmark Image

of width $S = [L - D_s (2 \text{ FD}-1)]$. Since every possible position of the spot along the intrack coordinate is equally probable, and the probability of finding the center of the spot in some detector row is unity, it follows that the probability of finding the center of the spot in a strip of width S is just equal to the ratio S/L. Thus,

$$P (D_s, \text{FD}) = \frac{S}{L} = [1 - D_s \frac{(2 \text{ FD}-1)}{L}] \qquad (A-1)$$

Equation (A-1) shows that the probability of finding the entire spot in an in-track row of the detector array is simply

$$P (D_s, \text{FD}=1) = 1 - \frac{D_s}{L} \qquad (A-2)$$

while the probability $P (D_s, \text{FD} = .5)$ of finding from 50 to 100 percent of the spot in a detector row is clearly always equal to unity or 100 percent. $P(D_s, \text{FD})$ can therefore be used to compute the probability that the beacon landmark power falling on a detector row will exceed a certain fraction (RPH) of the total power in the spot image, defined as the Relative Pulse Height (RPH). For the assumed case of a uniform flux density over the spot, RPH is simply the fraction of the total spot area $(A_s = \pi D_s^2/4)$ which is contained in a spectral detector row due to the protrusion of the edge of the spot by a distance $D_s\text{FD}$. RPH is therefore equal to FD only for the special cases when FD is equal to either 1.0 or 0.5. With the assumption of uniform intensity then, the relationship between RPH and FD is given by the equation

$$\text{RPH(FD)} = \frac{1}{2} + \frac{1}{\pi} [A \sqrt{1-A^2} + \sin^{-1}(A)] \qquad (A-3)$$

where $\quad A = (2 \text{ FD}-1) \qquad (A-4)$

Thus, if FD' and RPH'(FD') are the actual sampled values of the fractional overlap for the spot diameter and area (or power) respectively, then the probability $P(D_s,\text{FD})$ given by Equation (A-1) is the probability that FD' is between FD and 1.0, and the probability that RPH' is between RPH (FD) and 1.0. The quantity 1-P then gives the probability that the observed amplitude of a beacon landmark pulse (BPA') was degraded by a factor greater than 1-RPH(FD).

Table A-1 lists six values of FD and RPH(FD) in the range of 0.5 to 1.0 for the smallest and largest spot dismeters of the Landsat MSS, as given by Equation 2-4 of Section 2. Specifically, $D_s(.55\mu)/L=0.21$ and $DS(.95\mu)/L = 0.37$.

TABLE A-1

STATISTICAL DEGRADATION OF ARTIFICIAL LANDMARK PULSES
DUE TO THE PHENOMENON OF DETECTOR SHARING

Linear Overlap Fraction	Probability that observed pulse height is between RPH and 100% of its nominal (undegraded) value		Relative Pulse Height
FD	P(.55μ) (%)	P(.95μ) (%)	RPH(FD) (%)
1.0	79	63	100
0.9	83	70	95
0.8	87	78	86
0.7	92	85	75
0.6	96	93	63
0.5	100	100	50

The interpretation of these results is discussed for the case of a hypothetical sample of 100 random landmark pulses in the .55μ channel data. In this case one would expect to find that 79 of the pulses suffered no degradation due to detector sharing (P(FD=1.0) = .79), and that the remaining 21 pulses suffered a degratation by a factor greater than 0 (1.-RPH(FD=1) and less or equal to 50 percent. Eighty three of the pulses, on the other hand, would be expected to have pulse amplitudes that were equal to or greater than 95 percent of the maximum. Consequently, one would expect to find that the number of pulses which suffered an amplitude degradation of greater than 5 percent [100(1-RPH(FD=.9)] was 17 or 100 (1-P(FD=.9)). In a like manner one finds that the probability of a degradation or decrease greater than 25 percent is 8 percent (or 8 pulses out of 100), the probability of a decrease greater than 37 percent decrease is 4 percent, and the probability of a decrease greater than 50 percent is zero.

A-2   SAMPLING DEGRADATION STATISTICS

The discrete sampling of MSS imagery signals (as described in Section 2.1.3.3) can under certain conditions result in a decrease in the recorded pulse amplitude of a beacon landmark signature, corresponding to a fractional relative pulse amplitude (RPH) of less than unity. These conditions, and the statistical degradation that results when they exist are described as follows.

With reference to the definitions and notations defined in the preceding discussion, we recall that during the time interval between successive samples of a given detector, the image spot translates through a distance $\Delta X = gL$ in the image plane, where $g \equiv T_{sr}/DT$ is the ratio of the sample repetition period (T_{sr}) to the detector dwell time (DT). The data is said to be oversampled if $T_{sr} < DT$, making $g = \Delta X/L < 1.0$. For the Landsat MSS, the value of g was shown (in Section 2.1.3.3) to be approximately equal to 0.74. The digital representation of an analog pulse signature will therefore generally consist of several non zero samples or pixels representing a particular distribution of intensities which depends on the exact but random value of the first non zero sample and the relative values of ΔX, the detector width L, and the image spot diameter D_s, or, $g \equiv \Delta X/L$ and $\alpha \equiv D_s/L$.

The various possible pulse shapes associated with a given value of g and α are illustrated in Figure A-2 for g = 0.6 and for three values of α (1, 1/3, and 1/5). The various pulse shapes for a given g and α were created by simply varying the initial amount of the spot overlap $(FD \equiv X/D_s)$ associated with the first non zero sample. This variation of the initial condition was accomplished in discrete increments corresponding to $X_k = kL/10$ (for k = 1, 2, 3. . .), and the resulting (kth) pulse shape was then obtained from the sequence of the (jth) sampling positions defined by

$$X_{kj} = X_k + (0.6L)j \quad \text{(for } j = 0,1,2,\ldots\text{)}, \qquad \text{(A-5)}$$

which were used to determine the corresponding overlap fractions FD_{kj} and the corresponding $RPH_{kj}(FD_{kj})$ values from Equation A-3.
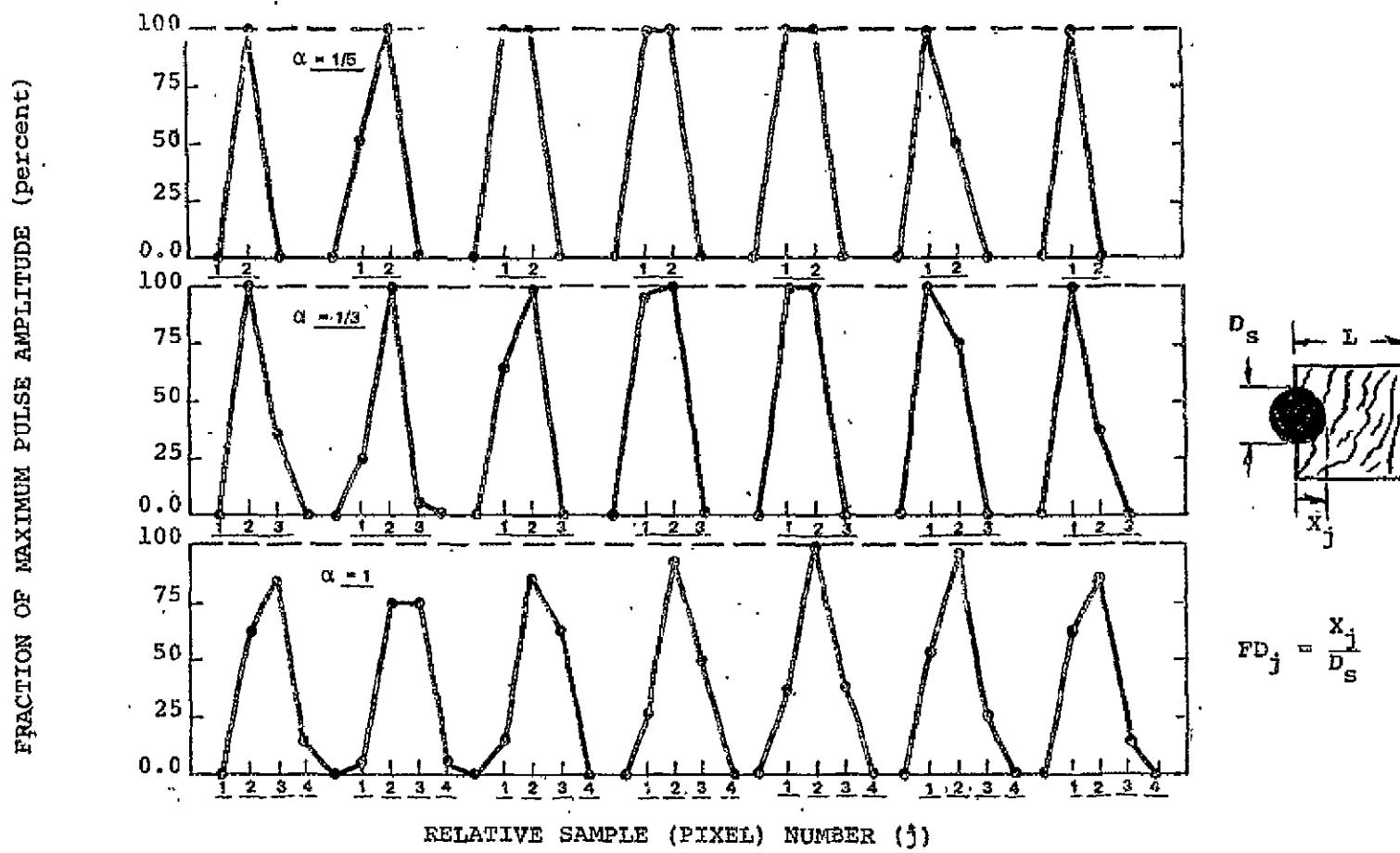
Figure A-2 Efficiency and Shapes of Beacon Landmark Pulse Signatures
for a Uniform Distribution of Equally Probable Initial Conditions.
Shown for 3 Fractional Spot Diameters ($\alpha = D_s/L$) and a Sampling
Step Size $\Delta X = 0.60L$

From Figure A-2 it is clear that the possibility of pulse amplitude degradation due to sampling is enhanced by large values of α and/or g. The condition which guarantees an undegraded signal amplitude for at least one of the samples of a pulse signature is expressed by the relationship

$$(g + \alpha) < 1.0. \tag{A-6}$$

The validity of this condition is supported by the constructed pulse shapes shown in Figure A-2, for the two smaller values of α, which correspond to values of 4/5 and 28/30 for $(g+\alpha)$. Failure to satisfy this inequality condition does not mean that one of the RPH values cannot be unity, but only that a unity value is not guaranteed. This is illustrated for the third case, where $\alpha = 1.0$, and it is seen that an undegraded pulse amplitude results for one point in the initial sample spectrum even though $g+\alpha$ is as large as 1.6. In this case the maximum pulse amplitude degradation, corresponding to another point in the initial sample spectrum, can be as large as 25 percent. Under these conditions one would expect the degradation of observed pulses to be randomly distributed over a range of from 0 to 25 percent of the maximum possible pulse amplitude.

From Figure A-2 it is clear that the maximum degradation (for the case when $g+\alpha < 1.0$) occurs for the initial sample condition that results in a symmetric pulse shape characterized by two equal relative-maximum sample signals, while the undegraded pulse shape (for $\alpha \leq 1.0$) is associated with a symmetric pulse shape having only one maximum sample signal. Thus, from the symmetry involved, one finds that the lowest relative pulse amplitude RPH*(FD*) for the maximally degraded pulse shape corresponds to a fractional overlap of magnitude

$$FD^* = .5 \left[1 + \frac{(1-g)}{\alpha}\right]. \tag{A-7}$$

For the general case then, in which $g + \alpha > 1.0$, one can use Equations A-7 and A-3 to determine RPH* and the fractional degradation range DR* defined by DR* = (100-RPH*) percent of the maximum (undergraded) pulse amplitude. Thus, taking $g = 0.74$ and $\alpha_i = .21, .25, .29,$

and .37 for the Landsat MSS, we conclude from the above agruments that the corresponding theoretical degradation ranges (DR$_i^*$) are 0, 0, 2, and 9 percent of the maximum possible pulse amplitudes in the corresponding wavelength channels. From this we conclude that the statistical effects of pulse amplitude degradation due to discrete sampling (in the Landsat MSS) would not be appreciable compared to the nominal background noise associated with the ordinary scan signal. Thus in relation to the analysis of the results of the Landsat/Searchlight landmark experiments (discussed in Section 2.5), it appears that the only meaningful conclusion which can be drawn from the above findings is that they serve only to magnify the conservative nature of the theoretical pulse amplitude model which underestimated the observed near IR pulse amplitudes, on the average, by 10 percent.

APPENDIX B

SOLAR ZENITH ANGLE VARIATIONS
AT SUBSATELLITE POINTS AS A
FUNCTION OF TIME AND LATITUDE

Because EOS orbits are designed to be sun synchronous, the satellite will pass over the same point on the earth at essentially the same local time every 18 days. However, even though the local time remains essentially the same, changes in the north/south position of the sun with time of year (or season) will alter the solar zenith angle (θ_o) at the subsatellite point (as defined in Figure B-1), thus producing variations in the lighting conditions under which EOS imagery is obtained. The value of θ_o at any given subsatellite point can therefore be represented as a function of three parameters; the latitude of the subsatellite point, the local time at the descending node (north to south equatorial crossing), and the time of year. For any given EOS orbit, however, the local time at the descending node remains essentially constant throughout the entire mission.

A general expression for the variation of θ_o with time of year and latitude is derived with the aid of Figures B-2 and B-3 as follows. Figure B-2 shows the sun and satellite position vectors S and R in an earth centered descending node reference frame (XYZ) which is regarded as fixed in inertial space. The x-axis defines the fixed direction from the center of the earth to the descending node, and the z-axis defines the fixed direction of the earth's spin axis. The satellite position vector (R) is referenced to the XYZ coordinate frame through the spherical polar coordinate angles θ and φ, while the sun position vector (S) is referenced to the XYZ frame through the solar elevation angle ψ (measured from the equatorial plane) and the descending node – sun angle γ measured in the equatorial plane between the descending node and the projection (ξ) of S onto the equatorial plane. The solar elevation angle (ψ) varies bi-yearly between plus and minus 23.5 degrees (in a manner to be described) and the descending node-sun angle (γ) for an A.M. crossing time T_{DN} (measured in hours) is given by

$$\gamma = 15 (12 - T_{DN}) \text{ degrees.} \qquad (B-1)$$

From Figure B-2, the components of the unit satellite and sun vectors (R and S) along the directions $\underline{x}$, $\underline{y}$, and $\underline{z}$ are clearly given by

$$\underline{R} = \text{Sin} (\theta) \text{ Cos} (\varphi) \underline{x} + \text{Sin} (\theta) \text{ Sin} (\varphi) \underline{y} + \text{Cos} (\theta) \underline{z}, \qquad (B-2)$$

$$\underline{S} = \text{Cos} (\psi) \text{ Cos} (\gamma) \underline{x} + \text{Cos} (\psi) \text{ Sin} (\gamma) \underline{y} + \text{Sin} (\psi) \underline{z}. \qquad (B-3)$$
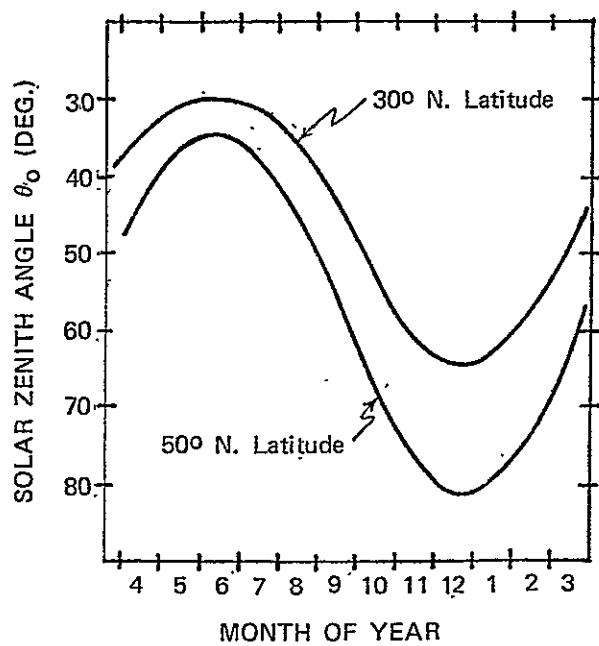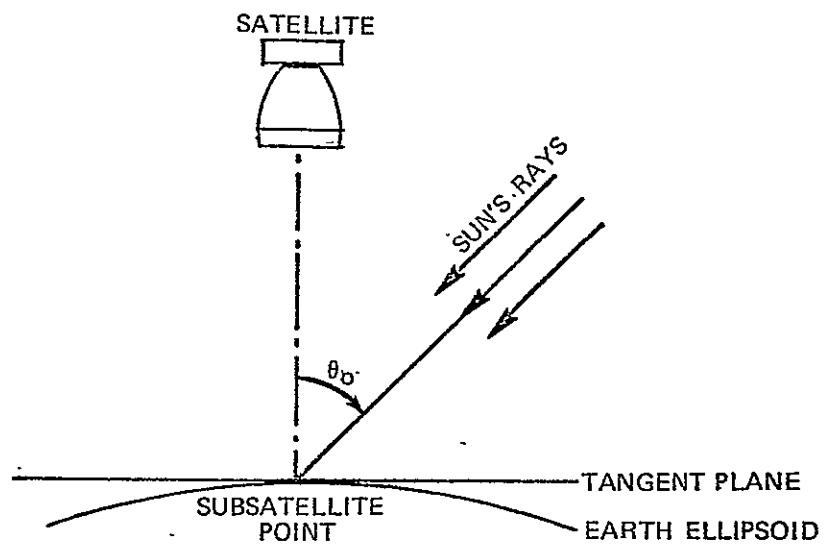
Figure B-1 . Solar Zenith Angle Variations at Subsatellite Point
as a Function of Season and Latitude for a 9:30 am
(Descending Node) Sun Synchronous Orbit.
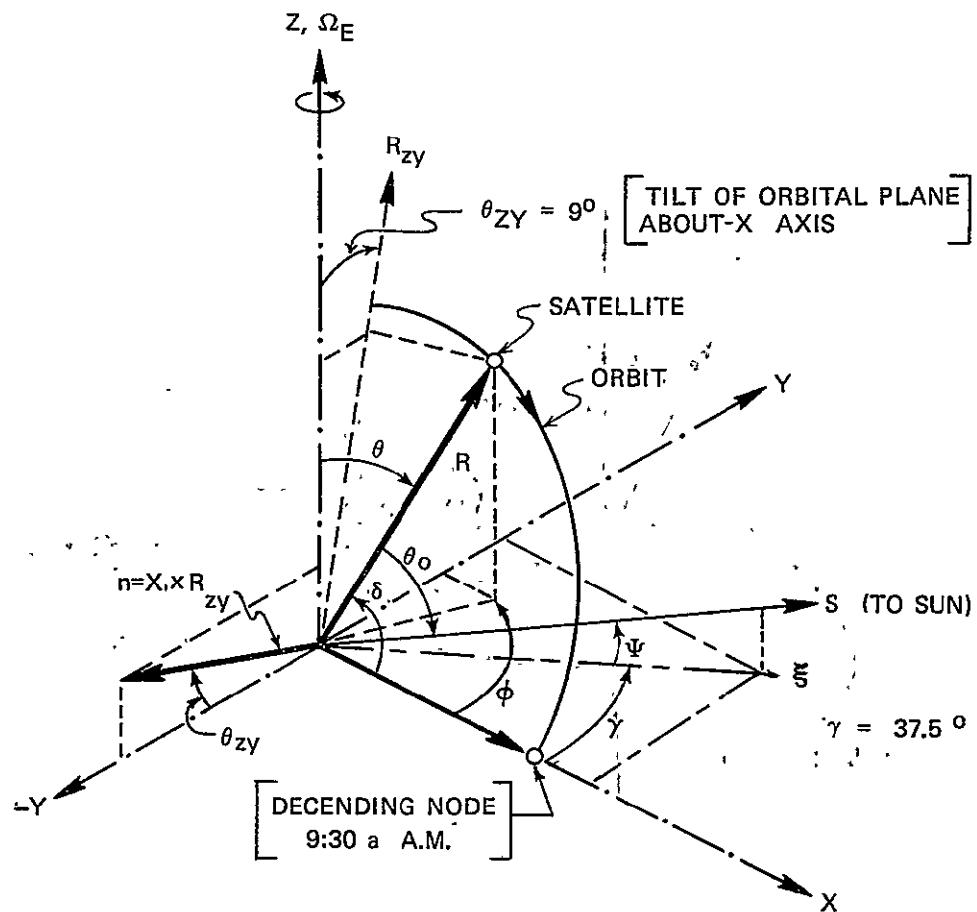
Figure B-2. Sun and Satellite Position Vectors in
the Earth's Descending Node Reference Frame.
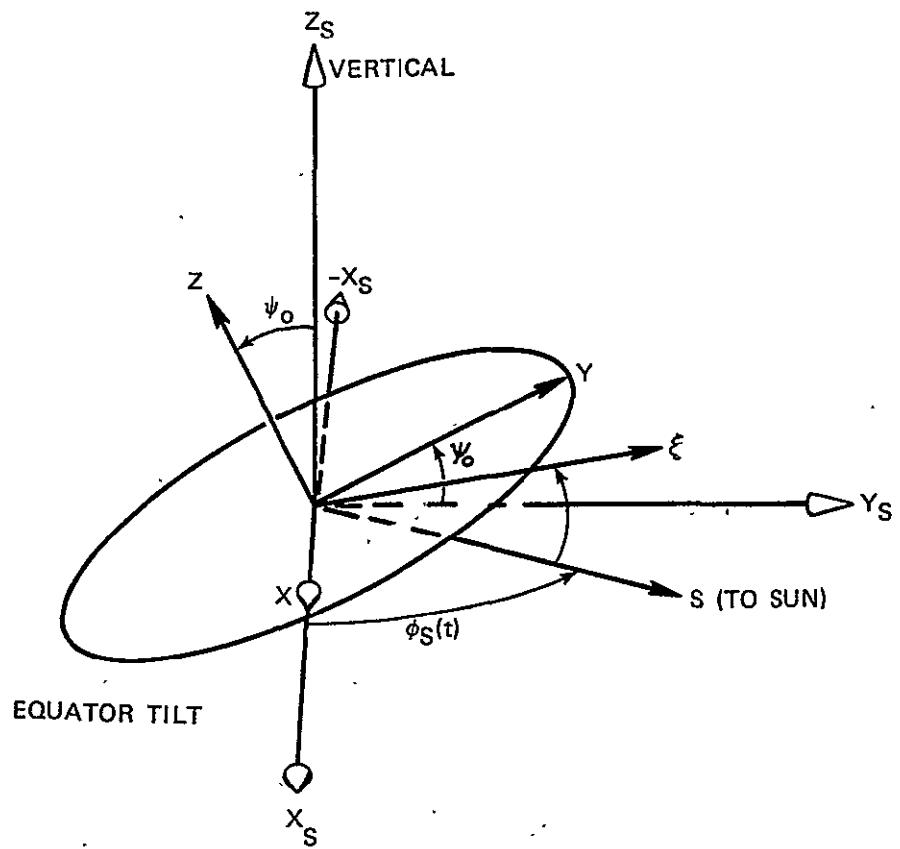
Figure B-3. Orientation of the Earth's Reference Frame (X,Y,Z), the Noon Equatorial Local Vertical ξ , and the Solar Position Vector S in the Ecliptic Reference Frame (X_S, Y_S, Z_S).

Using the vector relation $\underline{R} \cdot \underline{S} = \cos(\theta_o)$ we obtain a general expression for θ_o in the form:

$$\theta_o = \text{arc cos} [\cos(\psi) \cos(\gamma) \cos(\varphi) \sin(\theta)$$

$$+ \cos(\psi) \sin(\gamma) \sin(\varphi) \sin(\theta) + \sin(\psi) \cos(\theta)] \qquad \text{(B-4)}$$

This equation as it stands is unsuitable for determining θ_o however because of the fact that the azimuth angle φ is not an independent parameter. The angle φ can be expressed, however, in terms of the independent parameters θ and the tilt angle (θ_{zy}) of the orbital plane about the negative descending node axis (-X), measured relative to the Z-axis. This is accomplished by temporarily introducing another angle parameter (δ) which defines the angle between the satellite position vector $\underline{R}$ and the X-axis. Then from Figure B-2 it is clear that the components of $\underline{R}$ along $\underline{Y}$ and $\underline{Z}$ can also be expressed in terms of θ_{zy} and δ, giving:

$$R_y = \underline{R} \cdot \underline{Y} = \sin(\theta) \sin(\varphi) = \sin(\delta) \sin(\theta_{zy}) \qquad \text{(B-5)}$$

and

$$R_z = \underline{R} \cdot \underline{Z} = \cos(\theta) = \sin(\delta) \cos(\theta_{zy}) \qquad \text{(B-6)}$$

Elimination of $\sin(\delta)$ from the equations then gives the desired relation

$$\sin(\varphi) = \tan(\theta_{zy}) / \tan(\theta) \qquad \text{(B-7)}$$

Defining $\beta = \theta_{zy}$ and $\alpha = \pi/2 - \theta$ (for convenience) we obtain a general expression for θ_o in the form

$$\theta_o = \text{arc cos} \left\{ \cos(\psi) \left[\cos(\gamma) \cos(\alpha) \left(1 - \frac{\tan^2(\beta)}{\tan^2(\theta)} \right)^{1/2} + \sin(\gamma) \sin(\alpha) \tan(\beta) \right] \right.$$

$$\left. + \sin(\psi) \sin(\alpha) \right\} \qquad \text{(B-8)}$$

which gives θ_o in terms of the latitude (α), the solar elevation (ψ), and the fixed orbital parameters $(\gamma$ and $\beta)$.

The explicit variation of ψ with time is derived with the aid of Figure B-3 which depicts a non-spinning earth coordinate frame (xyz) with the earth's equatorial (xy) plane tilted through an angle $\psi_o = 23.5$ degrees in an ecliptic reference frame (X_s, Y_s, Z_s) which is similarly regarded as being fixed or at rest in space.

The angular position of the sun vector ($\underline{S}$) relative to X_s in the ecliptic plane ($X_s Y_s$) at time (t) is then denoted by φ_s (t), with the vernal equinox being defined for φ_s (t) = π. The solar elevation angle ψ shown in Figure B-2 is here depicted as ψ (t) such that ψ (t) = $-\psi$, with $\underline{\xi}$ still denoting the perpendicular projection of $\underline{S}$ onto the equatorial plane (xy). The vector ($\underline{\xi}$) representing the noon equatorial local vertical lies in the plane determined by $\underline{Z}$ and $\underline{S}$, and the vectors ($\underline{X}_s, \underline{X}, \underline{\xi},$ and $\underline{Y}$) all lie in the equatorial plane with the vector $\underline{Y}$ being in the $Y_s Z_s$ plane and inclined at an angle ψ_o relative to $\underline{Y}_s$.

The variation of ψ (t) with respect to the nearly uniform increase of φ_s (t) is derived from an examination of the direction cosines or components of a unit sun vector $\underline{S}$ in the XYZ frame.

$$\underline{S} = \cos (\varphi_s) \ \underline{X} + \sin (\varphi_s) \cos (\psi_o) \ \underline{Y} + \sin (\psi) \ \underline{Z} \qquad \text{(B-9)}$$

From the normality condition $\underline{S} \cdot \underline{S} = 1$ it follows that

$$\cos^2 (\varphi_s) + \sin^2 (\varphi_s) \cos^2 (\psi_o) + \sin^2 (\psi) = 1 \qquad \text{(B-10)}$$

and $\quad \sin (\psi) = \sin (\psi_o) \sin (\varphi_s)$. $\qquad \text{(B-11)}$

Thus, $\psi = -\psi$ (t) = $-$ arc sin [$\sin (\psi_o) \sin (\varphi_s$ (t))] defines the values of ψ used in Equation B-8 to compute the yearly variation of θ_o shown in Figure B-1, for latitudes of 30 and 50 degrees north, a descending node crossing time of 9:30 A.M. ($\gamma = 37.5$ degrees), and an orbital inclination of 99 degrees ($\beta = 9$ degrees).

APPENDIX C

DESIGN CONSIDERATIONS FOR

SOLAR BEACON LANDMARKS

In this appendix we discuss some of the theoretical and practical considerations relating to the use of curved mirrors as the effective radiation element in an artificial landmark station. From a theoretical viewpoint we show that curved mirrors could be used to do the job, but that the use of such would require the costly addition of an automated, two-axis, sun-tracking and mirror-pointing subsystem or, an uncommonly large curved mirror, in order to compensate for the large seasonal variations in the solar zenith angle (θ_o) shown in Figure C-1.

We note parenthetically, that neither of these alternatives appears to be as attractive, from the viewpoint of cost and reliability, as the alternative of using the compact and commercially available xenon searchlight described in Section 2.6.3 of this report. In addition to providing a theoretically adequate fixed beam radiation source for a nominal cost, a Searchlight Landmark Station (SLS) offers additional reliability and versatility through its capability to function at night and in every case where the overhead visibility is relatively good, even though the slant range solar radiation may be highly attenuated due to haze and/or distant clouds. Also, because of the extremely small duty cycle required, the cost of operating a 4 kw searchlight for a period of just six minutes every eighteen days can be considered insignificant in comparison to the overall operation costs for a national system of beacon landmark stations. This is especially clear when one realizes that a realistic design for the radiation element, and the landmark station as a whole, must include protection against damage that would otherwise result from harsh environmental conditions.

The large yearly variations in the sun's zenith and azimuth positions are therefore shown to introduce technical complications which
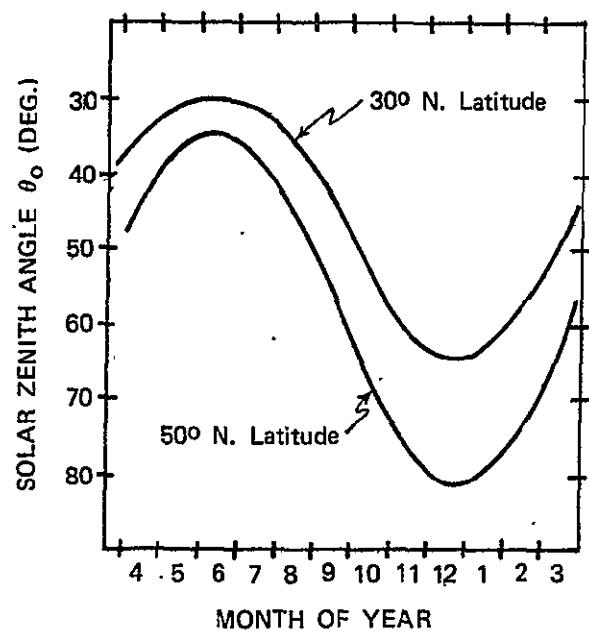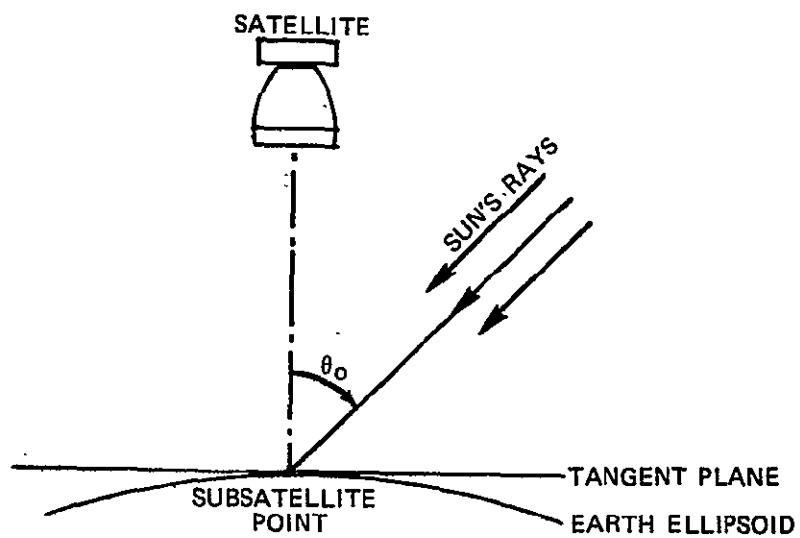
Figure C-1   Solar Zenith Angle Variations at Subsatellite Point
as a Function of Season and Latitude for a 9:30 am
(Descending Node) Sun Synchronous Orbit.

undermine the seemingly ideal virtures of using mirrors for the effective radiation element in a national system of beacon landmarks. These complications are not such as to make a Mirror Landmark Station (MLS) impractical but only less desirable (theoretically) than an SLS from the viewpoint of reliability, cost, and versatility. Although the experiments described in Sections 2.4 and 2.5 have confirmed the anticipated theoretical attributes of an SLS, it is nevertheless of interest to examine the theoretical performance and design considerations relating to the reflector component of an MLS.

In the following analyses we assume that the satellite passes directly over the landmark and we estimate the performance and design characteristics of both relatively small curved mirrors, which would require a sun-tracking and mirror pointing subsystem, and relatively large curved mirrors which could be maintained in a fixed orientation relative to the earth. Estimates of the actual mirror sizes in each case are determined on the basis of the intensity criteria described next.

C.1 SOLAR BEACON INTENSITY CRITERIA

The basic intensity criterion imposed on any landmark beacon is that it be capable of generating a unique and readily detectable pulse signature in the EOS MSS imagery data, when the interception is within a 1.5 by 6.0 degree cone. Automated recognition of a solar beacon landmark, as has been demonstrated with xenon searchlight landmark data, can be achieved by using a combination of uniqueness criteria based on the known spectral shape of the beacon landmark radiation and a set of spectral pulse amplitude thresholds for the MSS channels.

In the case of a xenon SLS for example, the xenon flair (shown in Figure C-2), which is spectrally confined within the near IR channel of the Landsat and EOS MSSs, provided a natural spectral uniqueness criterion which allowed low amplitude xenon searchlight pulses to be readily detected within an otherwise noisey background of the numerous and relatively large solar beacon pulses that exist in the MSS imagery data, due to the variety of natural and man made specular reflectors

NORMALIZED SPECTRAL DISTRIBUTIONS

WAVELENGTH (Microns)

XENON FLAIR

XENON $P_B(\lambda)$

SOLAR SPECTRUM
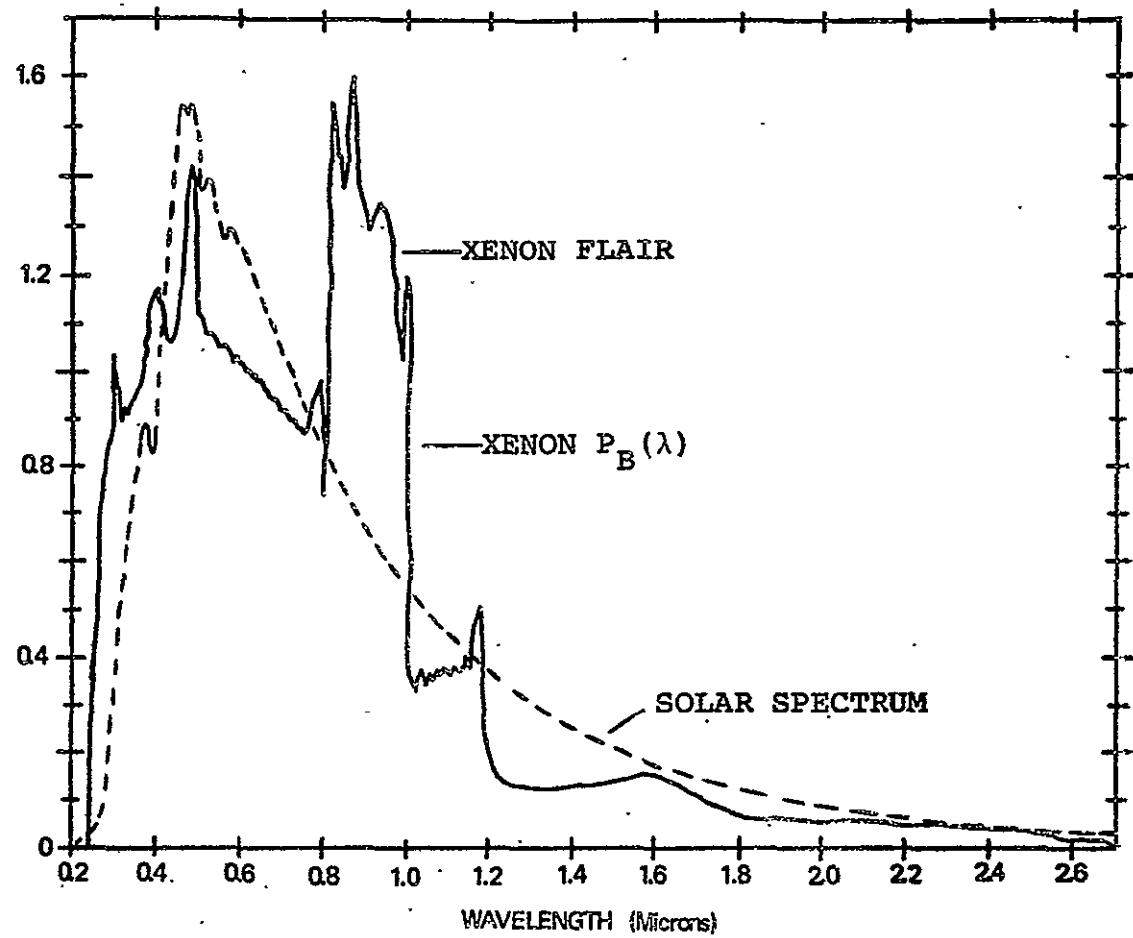
Figure C-2   Normalized Spectral Distributions for Solar
             Radiation (Upper Atmosphere) and Xenon
             Searchlight (in the kilowatt range).

that exist on the earth's surface. Under these conditions it was possible to construct an automated SLS detection scheme with a high degree of selectivity (or noise rejection) for a pulse-amplitude threshold sensitivity of only 7 percent (of full scale) in the near IR channel of the Landsat MSS.

A practical searchlight or solar beacon landmark should be capable of generating a pulse in the most sensitive or dominant MSS channel with an amplitude that would, under normal conditions, be much larger than the threshold sensitivity of the detection scheme. The safety factor must be large enough to allow for a reduction in the recorded pulse amplitudes by a factor of two, due to the phenomenon of detector sharing, as well as likely reductions in the beam intensity due to ageing and/or contamination of the optics, and also for possible increases in the optical thickness of the atmosphere relative to the clear standard atmospheric optical thicknesses assumed in the theoretical model. In addition, an allowance has to be made for the presently unknown pulse-amplitude threshold sensitivity of a near real time, on board, analog beacon landmark detection filter. This analog threshold sensitivity could conceivably be two to three times larger than the pulse amplitude threshold sensitivity for a digital filter due to the fact that the uniqueness test has to be performed in near real time.

Based on these considerations, a prototype xenon searchlight for an EOS SLS was selected with the capacity to generate a nominal (un-degraded) pulse amplitude of 46 percent of full scale, which is over six times larger than the demonstrated pulse amplitude sensitivity of the automated digital pulse amplitude detection scheme discussed in Section 1.6.

The corresponding design goal for the nominal (undegraded) amplitude of a solar beacon landmark pulse cannot be accurately estimated without first having some idea of the corresponding minimum threshold sensitivity that could be achieved in a highly selective automated detection scheme. A high degree of discrimination against other naturally occuring solar beacon signatures could conceivably be achieved by employing a transmission filter to limit the spectrum of the reflected light from an MLS to the range associated with just one

specific MSS channel. It will here be assumed that the use of such a
filter would provide an adequate MLS detection selectivity for a pulse
amplitude threshold of 7 percent of full scale in the .75 micron chan-
nel of the EOS MSS. Thus with due allowance for the attenuation of
the sunlight due to the filter, the design goal for a solar beacon
landmark signature will be assumed to be the same as that for a xenon
searchlight landmark signature. Namely that the nominal (undegraded)
pulse amplitude be 46 percent of the full scale range for the .75 micron
channel of the EOS MSS, over an interception cone angle of 1.5 by 6.0
degrees.

C.2 THEORETICAL SIGNATURE CHARACTERISTICS OF SOLAR BEACON LANDMARKS

In this section we develop a theoretical model for predicting the
amplitude of a solar beacon landmark pulse in terms of the size of a
curved mirror and the angular position of the sun relative to the local
vertical. The model, subject to the aforementioned intensity criteria,
is then used to determine the approximate size of a standardized mirror
for an EOS MLS.

C.2.1 General Geometric Considerations

The function of an MLS mirror, as illustrated in Figure C-3, is
to reflect incident solar radiation into a small cone which can be
maintained in a fixed orientation relative to the earths surface,
irrespective of the seasonal changes in the sun's position. The orient-
ation being that which causes the center of the cone to intercept the
nominal (time-average) orbital path of the satellite at right angles.
In addition, the cone size or beam spread must be sufficient to allow
for the maximum anticipated deviations in the sighting angle due to
deviations of the spacecraft attitude and orbital position from nomi-
nal. In the present case it has been assumed that this requirement
can be met by a beam spread of 1.5 degrees in the intrack direction
and 6.0 degrees in the crosstrack direction.
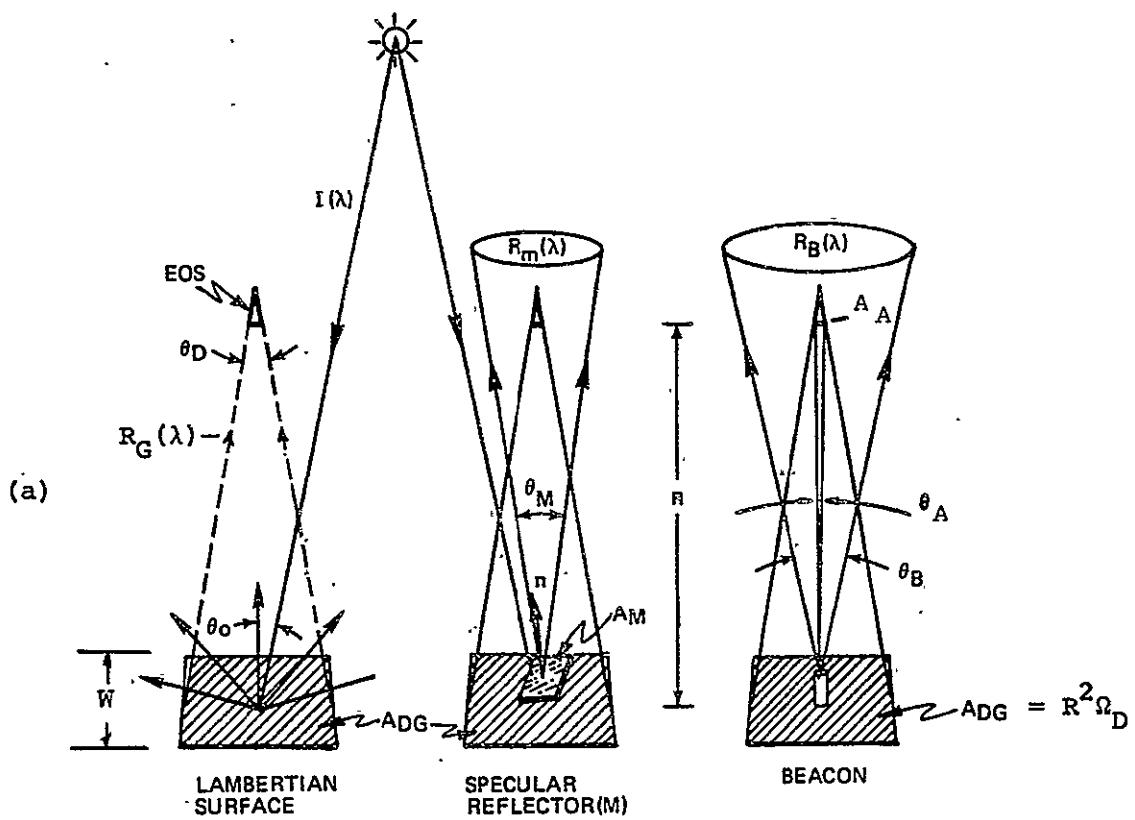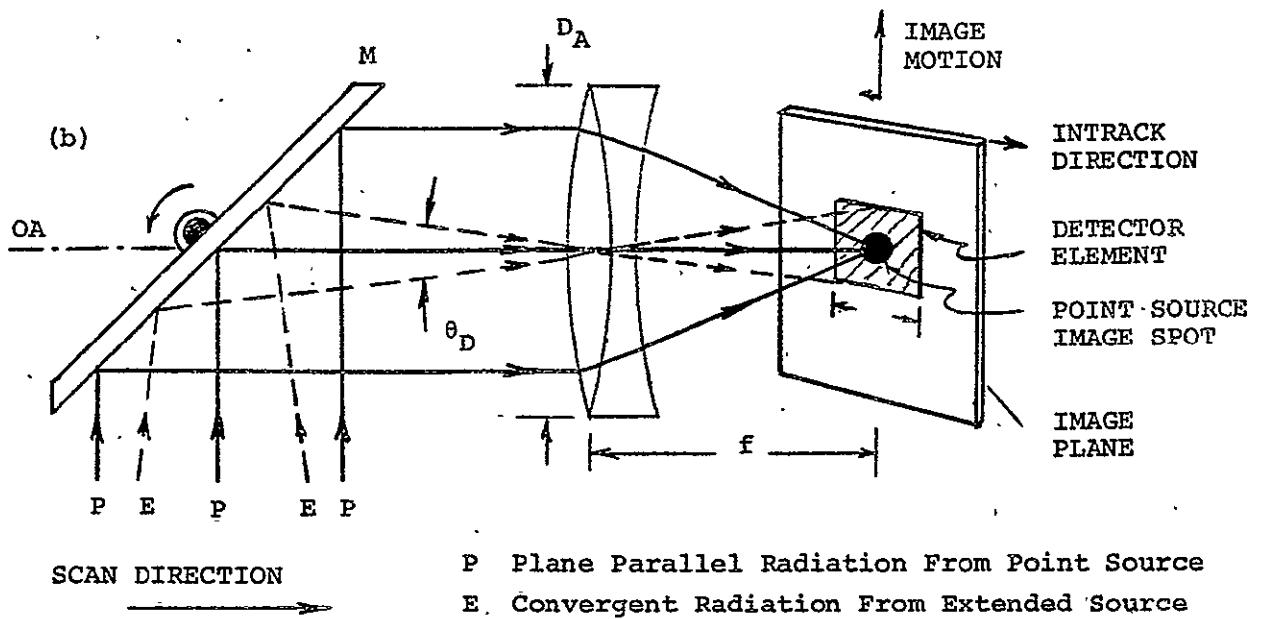
These conditions could be satisfied in principle by employing a fixed curved mirror, as illustrated in Figure C-4 which is large enough to accommodate the seasonal changes in the sun's position for all latitudes in the U.S. and for the time of day determined by the particular sun syndronous orbit employed. The seasonal variations of the sun's zenith angle throughout the U.S., as shown in Figure C-1 (for the case of a 9:30 A.M. decending node), suggest that the angular dimensions of a standardized stationary mirror would have to be large enough to accommodate a 50 degree range of solar zenith angles, with a corresponding azimuth angle range of about 54 degrees. The physical size of such a mirror would then be determined by the magnitude of the radius of curvature that is required to satisfy the intensity criteria for an MLS.

These considerations illuminate an important physical character-istic of a spherical convex mirror. Its three-dimensional size or volume is directly proportional to its surface area ($A_m = \Omega_m r^2$) which is fixed or determined by the product of two functionally independent design parameters: the solid angle subtended (Ω_m), which is determined entirely by the angular zenith and azimuth ranges of the incident radiation that must be accommodated, and the radius of curvature (r) which is determined entirely by the reflected intensity requirements for a given illumination intensity. This characteristic of a curved mirror tends to conflict with the intuitive notion that the reflected intensity should depend explicitly on area of the mirror surface, which is only true for the special case of a flat mirror.

Thus, if the size of a standardized stationary MLS mirror would be impractically large, as the present analysis will suggest, then the only alternative left is to minimize the ranges of the solar zenith and azimuth angles that have to be accommodated through the use of an automated two-axis sun tracking and mirror pointing control system. Thus minimizing the values of the mirror's polar and azimuth angle in-crements $\Delta\theta$ and $\Delta\phi$, and hence its overall size for a given radius of curvature. The determination of these minimum polar and azimuth angles is discussed next.
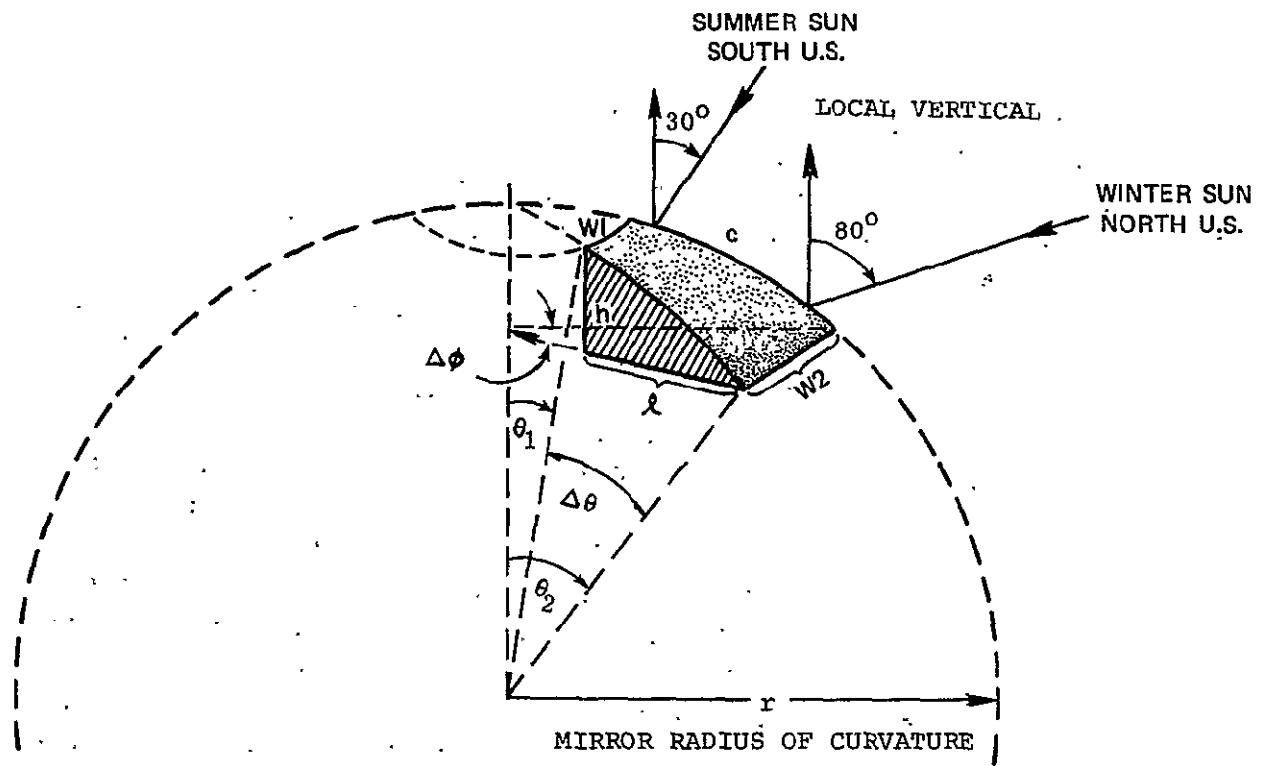
Figure C-4 Geometry and Size Parameters for a
Standardized Stationary Curved Mirror
Landmark Element.

C.2.2 Minimum Polar and Azimuth Angle Ranges for a Curved Solar Beacon Mirror

The minimum values of the curved mirror's solar and azimuth angle increments, $\Delta\theta$ and $\Delta\phi$, required to provide a reflected beam spread of 1.5 by 6.0 degrees along the intrack and crosstrack directions, respectively, were determined with the aide of two CSDL computer programs. One program (REV.ALIS) was used to compute the seasonal changes in the zenith and azimuth angles of the sun, relative to both a longitude-latitude surface coordinate frame and an intrack-crosstrack surface coordinate frame for latitude points between 30 and 50 degrees north. Then using the crosstrack direction as the azimuth reference, it was found that the solar zenith and azimuth angles varied over the ranges of 30 to 80 degrees and +2 to -50 degrees, respectively. The second computer program (REV.SPHERE) was then used to compute the minimum values of $\Delta\theta$ and $\Delta\phi$ required to assure a minimum intrack-crosstrack beam spread of 1.5 by 6.0 degrees over these solar zenith and azimuth ranges for the case where a gimbaled two-axis, sun-tracking and mirror-pointing system is employed to track the sun's position and to keep the reflected beam oriented in the vertical direction. The results showed that the angles $\Delta\theta$ and $\Delta\phi$ subtended by the mirror would have to be on the order of 4.6 and 2.0 degrees respectively, for a nearly rectangular mirror segment, corresponding to a mean polar angle of $\theta_o(MAX)/2$ = 40 degrees.

Thus, for a given radius of curvature, these curved mirror design parameters serve to determine the overall size of the curved mirror element for a standardized MLS that could be located at any latitude within the continental U.S., and at any point in a crosstrack strip which falls within about $\pm$ 10 nautical miles of the nominal subsatellite point ground track. These figures are based on an assumed sun tracking and mirror pointing accuracy of approximately $\pm$ 0.1 degrees in the respective zenith and azimuth angles. The minimum radius of curvature required to assure a nominal (undegraded) MLS pulse amplitude of 46 percent in an EOS MSS is discussed next.

C.2.3 The Minimum Radius of Curvature for a Curved Solar Beacon Mirror

The nominal (undegraded) beacon pulse amplitude (BPA_i) in the ith channel of an MSS corresponding to a solar beacon can be computed as a fractional percent of the full scale response for the ith channel by means of the equation

$$BPA_i = 100 \ PB_i/PEM_i \quad \%, \qquad \text{(C-1)}$$

where PB_i is the solar beacon power contained in the ith channel image spot (or blurr circle) in the MSS image plane (for further details on this see discussion of Beacon Landmark Imaging Characteristics in Section 2.1.3), and PEM_i is the maximum recordable extended source power impinging on a given detector in the ith channel. PEM_i is therefore the detector power associated with a maximum (100 of percent full scale) scan signal in the ith channel of the MSS. In terms of the MSS parameters

$$PED_i = k_i \ BR_{gmi} \Omega_D A_A \qquad \text{(C-2)}$$

where k_i is the MSS optical transmission factor for the ith channel; BR_{gmi} is the calibrated (ith channel) Bolometric Intensity Radiance [watts/M^2-str] at the MSS aperture associated with a maximum or full scale scan signal in the ith channel; $\Omega_D = \theta_D^2$ is the solid IFOV of the MSS, given by the square of the linear IFOV (θ_D); and A_A is the aperture area. (For further details on this see discussion of Extended Source Imaging Characteristics in Section 2.1.2).

The solar beacon image power on the other hand can be expressed as

$$PB_i = k_i PR_i \ BW_i \ \Omega_A, \qquad \text{(C-3)}$$

where PR_i is the Power Radiance [watts/μ_i-str] at the aperture associated with the solar beacon (averaged over the ith bandwidth); BW_i [μ] is the bandwidth of the ith channel; and $\Omega_A = A_A/R^2$ is the solid angle subtended by the MSS aperture at an altitude R. The solar beacon power radiance is further defined by the expression

$$PR_i = PR_i^o \ e^{-OT_i [1+\sec(\theta_o)]} \ FT_i, \qquad \text{(C-4)}$$

where PR_i^O is defined as the unattenuated power radiance of the solar beacon; OT_i is the vertical optical thickness of the atmosphere (averaged over the ith bandwidth); θ_o is the solar zenith angle as defined in Figure C-1, and FT_i is the MLS filter transmission factor. The term $\exp[-OT_i(1+\sec(\theta_o))]$ represents the combined vertical and slant range atmospheric transmission factor based on a flat atmosphere approximation.

The unattenuated power radiance of solar radiation reflected from a curved mirror is derived with reference to the ray geometry shown in Figure C-5. Radiation propagating in the -Z direction, and assumed initially to be plane parallel, is intercepted by a small spherical reflecting surface of area A_m whith subtends a small solid angle $\Omega_m = A_m/r^2$ about a polar angle $\theta = .5\theta_o$. If $I(\lambda)$ is the irradiance or spectral intensity [watts/m$^2\mu$] of the incident radiation, then the spectral power density [watts/μ] of the vertically reflected beam is given by

$$PD(\lambda) = I(\lambda) A_m \cos(\theta), \qquad\qquad (C-5)$$
$$= r^2 I(\lambda)\Omega_m \cos(\theta).$$

A ray which impinges on the mirror surface at a point $P(r,\theta,\phi)$ will have an angle of incidence equal to θ and will be reflected through an angle of 2θ in the azimuth plane $\phi = \text{constant}$. The polar angle of a reflected ray (θ_R) is therefore related to the polar angle θ of its point of origin on the mirror surface by the transformation $\theta_R = 2\theta$. The solid angle of reflected beam

$$\Omega_R = \text{Sin}(\theta_R)\Delta\theta_R \Delta\phi \quad, \qquad\qquad (C-6)$$

is therefore related to the solid angle of the mirror

$$\Omega_M = \text{Sin}(\theta)\Delta\theta\Delta\phi \quad, \qquad\qquad (C-7)$$

by
$$\Omega_R = \text{Sin}(2\theta)(2\Delta\theta)\Delta\phi \qquad\qquad (C-8)$$
$$= 4\cos(\theta)\text{Sin}(\theta)\Delta\theta\Delta\phi$$
$$= 4\cos(\theta)\Omega_M \qquad (\text{for } \Omega_M << 1.0)$$

$$R(\lambda) = \frac{r^2}{4} \ I(\lambda) \ \frac{\text{Watts}}{(\mu\text{-STR})}$$
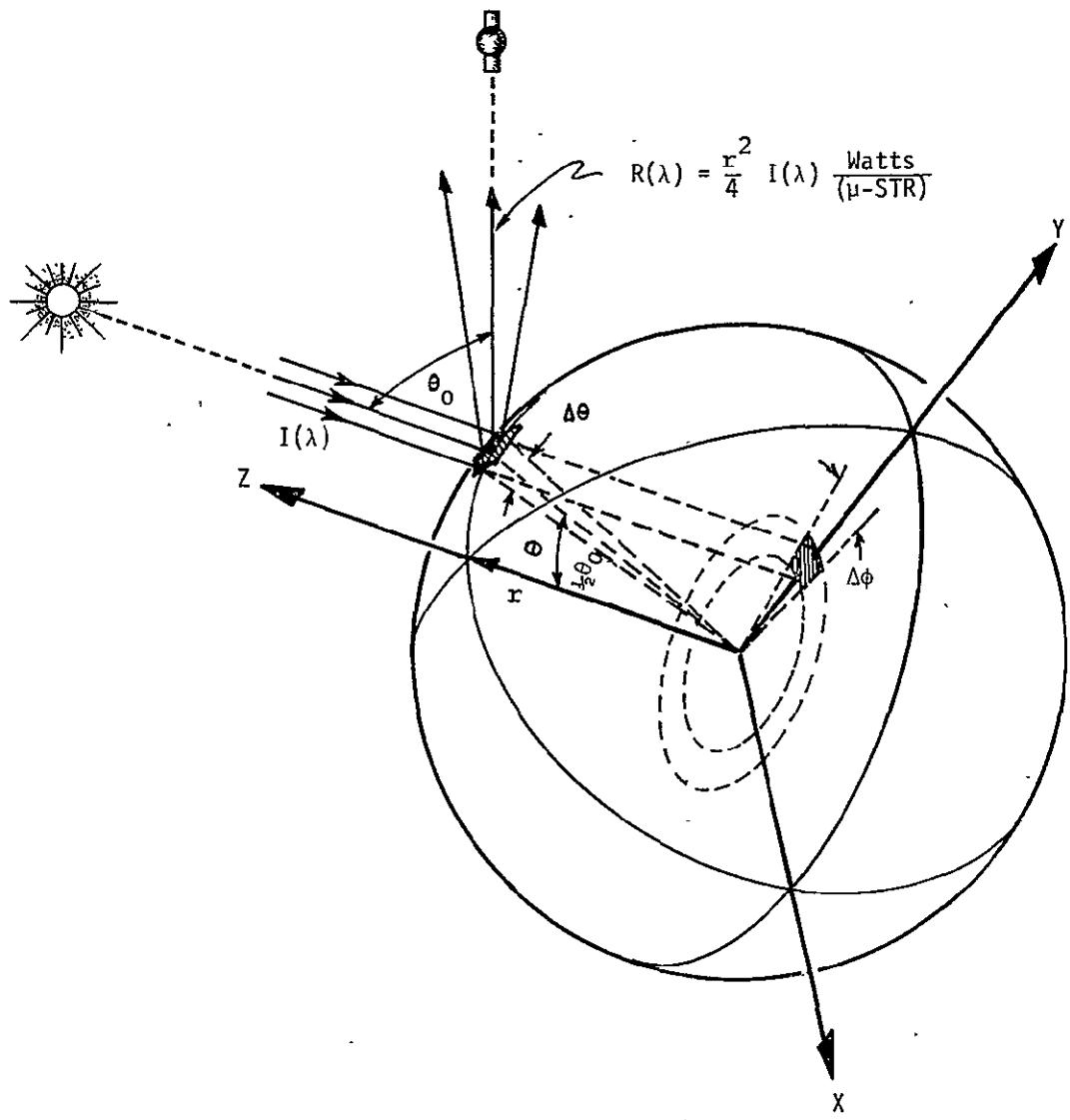
Figure C-5   Reflection-Divergence Characteristics
of a Curved Mirror.

C-13

If the incident radiation is not exactly parallel however, but is derived from an extended source like the sun, then the solid angle of the reflected radiation will be increased by the solid angle $\Omega_s = \pi\theta_s^2/4$ defining the solid divergence of a uniformly bright disc which subtends an angle $\theta_s = .53$ degrees relative to a point on the earth's surface. Thus

$$\Omega_R = 4\cos(\theta)\,\Omega_M + \Omega_S \quad , \tag{C-9}$$

and the unattenuated power radiance (PR_i^O) of solar radiation reflected from a curved mirror can then be epxressed in the form

$$PR_i^O(\theta) \equiv \frac{PD_i}{\Omega_R} = \frac{r^2 I_i\,\Omega_M\,\cos(\theta)}{4\cos(\theta)\,\Omega_M + \Omega_S} \quad . \tag{C-10}$$

which can be simplified to

$$PR_i^O = PR_i^O(\theta) = \frac{r^2 I_i}{4(1+\delta)} \qquad (\frac{\text{watts}}{\mu\text{-str}}) , \tag{C-11}$$

where

$$\delta = \frac{\Omega_s}{4\cos(\theta)\Omega_m} \quad . \tag{C-12}$$

PR_i^O is therefore expressed rather simply in terms of the radius of curvature (r) of the mirror; the solar irradiance I_i at the top of the atmosphere (averaged over the bandwidth of the ith MSS channel); and the parameter δ. Since θ is restricted to the value $\theta_o/2$ in order to provide a vertically oriented beam, δ can be expressed in the equivalent form

$$\delta = \frac{\pi\,\theta_s^2}{8\,\sin(\theta_o)\Delta\theta\Delta\phi} \tag{C-13}$$

Thus for the conditions stated in Section C.2.2, ($\theta_s=0.53$ degrees, $\theta_o(\text{MAX})=80$ degrees, $\Delta\theta=4.6$ degrees, and $\Delta\phi=2.0$ degrees) we have $\delta(\text{MIN})=.012$ and $\delta(\text{MAX})=\delta(\theta_o=30$ degrees$)=.024$. This shows that the changes in the angular orientation (θ) of the mirror, as it tracks the sun's position to maintain $\theta=\theta_o/2$, will have very little affect on the intensity of the reflected beam.

C-14

Finally, using Equations C-1 to C-4 and C-11, we obtain the following simplified expression for the theoretical pulse amplitude of solar beacon landmark

$$BPA_i = r^2 G_i \qquad \text{\% Full Scale} \qquad (C\text{-}14)$$

$$\text{where} \qquad G_i = \frac{25\ I_i\ BW_i\ FT_i\ AT_i}{(R\theta_o)^2\ BR_{GMi}\ (1+\delta)} , \qquad (C\text{-}15)$$

$$\text{with} \qquad AT_i = e^{-OT_i[1+Sec(\theta_o)]} ,$$

defines the MSS channel sensitivity constants. The values of G_i shown in Table C-1 were computed for a satellite altitude (R) of 700 kilometers, an MSS IFOV (θ_D) of 43 micro radians, a filter transmission factor (FT_i) of 0.8 in all channels, and a solar zenith angle of 80 degrees (δ=.012), with the values of I_i taken from Figure C-2.

TABLE C-1

EOS MSS SENSITIVITY CONSTANTS

FOR A CURVED MIRROR SOLAR BEACON

EOS MSS CHANNEL	1	2	3	4
Center Wavelength [μ]	.55	.65	.75	.95
BW_i [μ]	.1	.1	.1	.3
OT_i [-]	.379	.295	.242	.195
AT_i [-]	.077	.136	.195	.268
I_i [watts/M^2-μ]	1759	1583	1251	812
BR_{GMi} [watts/M^2-str]	24.8	20.0	17.6	46.0
G_i [%FS/M^2]	.01191	.02348	.03024	.03095
r_i [M]	62	44	39	39

The radius of curvature required to produce a nominal (undegraded) pulse amplitude of 46 percent of full scale was then obtained from the equation $r_i = (46/G_i)^{1/2} = 62, 44, 39$, and 39 meters respectively. The corresponding minimum size of a standardized sun tracking MLS mirror would therefore be characterized by rectangular curvalinear dimensions on the order of

$$\ell_\phi = r\ \text{Sin}(40)\Delta\phi\ =\ .875\ \text{M or } 2.9\ \text{feet}, \qquad\qquad (C\text{-}16)$$

$$\text{and}\quad \ell_\theta\ =\ r\Delta\theta\ =\ 3.13\ \text{M or } 10.3\ \text{feet}.$$

These mirror dimensions are larger than would be required to satisfy the design goal minimum pulse amplitude criterion (of 46 percent of full scale) at more elevated sun positions and/or at latitudes below 50 degrees north. Consequently we emphasize that the above curved mirror dimensions relate specifically to a standardized EOS MLS mirror element design which theoretically satisfies the following design requirements: It permits MLSs to be located at any latitude within the continental U.S.A.,and with a sun-tracking and mirror-pointing subsystem, having an absolute accuracy of about $\pm$ 0.1 degrees in azimuth and elevation, the mirror element can maintain an intrack-crosstrack beam spread of at least 1.5 by 6.0 degrees (relative to the nominal ground track) throughout the entire year. In addition, it provides a nominal (undegraded) pulse amplitude (for an EOS MSS IFOV of 43 microradians or less) under the most unfavorable conditions of sun position and/or latitude.

The necessity of employing a sun-tracking and mirror-pointing device could of course be circumvented by utilizing fixed curved mirrors that are large enough to accommodate the seasonal changes in the sun's position at the time of flyby. With reference to Figure C-4 again, the size and approximate shape of such mirrors, consistent with a standardized design, would then be governed by the following values for the relevant angular parameters:

$$r\ =\ 128\ \text{feet}$$
$$\theta\ \text{(center)}\ =\ 27.5\ \text{degrees}$$
$$\Delta\theta\ =\ 28.0\ \text{degrees}$$
$$\Delta\phi\ =\ 54.0\ \text{degrees}$$
$$\theta_1\ =\ 13.5\ \text{degrees}$$
$$\theta_2\ =\ 41.5\ \text{degrees}$$

The corresponding physical dimensions would then have the values:

$$c = 63 \text{ feet}$$
$$W2 = 80 \text{ feet}$$
$$W1 = 28 \text{ feet}$$
$$\ell = 55 \text{ feet}$$
$$h = 29 \text{ feet}$$

Fixed mirrors, it seems, would not be desirable for an MLS design, even if it could be shown that the overall cost per station would be less than that for a station design incorporating an automated sun-tracking and mirror-pointing device. In the future it may be possible to consider smaller and more practical mirror systems based on a different set of design requirements for such things as the minimum acceptable pulse amplitude, and/or the uncertainties in the satellite's attitude and orbital position, and/or the IFOV of future EOSs. Any improvements in this regard would of course serve to reduce the size and cost of the sun-tracking and mirror-pointing subsystem required for an MLS and, also, the size and cost of the searchlight component required for an SLS.

LIST OF REFERENCES

1.   R. White, R. Var, et.al., "Interim Technical Report No. 2,
      Advanced Earth Observation System Instrumentation Study (AEOSIS)",
      CSDL Report R-821, October 1974.

2.   Searchlight Battery A, of the 197th Field Artillery Group is
      headquartered in Manchester, New Hampshire. The portable xenon
      searchlights employed by the battery have a 30" diameter and are
      capable of operating with d.c. input powers of 10, 15, and 20 kw.
      Further details concerning Battery A's involvement in the search-
      light experiments are given in the Acknowledgements section.

3.   At the time of the experiment, the entire complement of approxi-
      mately 132 Battery A reservists was in Utah for two weeks of
      training at Camp Williams, under the command of Captain Paul Myron.
      The searchlights utilized in the Utah experiment were provided
      by Searchlight Battery D of the Utah Army National Guard (140th
      FA Group) in Logan, Utah.

4.   NASA-GSFC, "Advanced Scanners and Imaging Systems for Earth Obser-
      vations", (Superintendendent of Documents, U.S. Government Printing
      Office, Washington, D.C. 20402, 1973), pp. 527-534.

5.   See Reference 4., pp. 99-102

6.   W. E. Thouret, et.al., "20 to 30 kw Xenon Compact Arc Lamps for
      Searchlights and Solar Simulators", Journal of IES/October 1972,
      pp. 8-18.

7.   H.S. Strauss, et.al., "New Xenon Compact-Arc Projection Lamps for
     Horizontal Operation", Journal of the Society of Motion Picture
     and Television Engineers, Volume 81, Number 1, January 1972.

8.   W.E. Thouret and H.S. Strauss, "New Designs Demonstrate Versatil-
     ity of Xenon High-Pressure Lamps", Illuminating Engineers,
     Volume LVII, No. 3, Section I, p. 150 (March 1962).

9.   W.E. Thouret, et.al., "High-Brightness Xenon Lamps with Liquid-
     Cooled Electrodes", Paper presented at the National Technical
     Conference of the Illuminating Engineering Society, August 30 to
     September 3, 1964, Miami Beach, Florida.

10. An estimate of 50 percent for the efficiency of a Xenon short-arc
     discharge lamp was given to the author by three independent users;
     Mr. Hatch of the Strong Electric Division of Holophane, Mr. Waskyke,
     Jr. of the Duro-Test Corporation, and Dr. Sampson of the Air Force
     Cambridge Research Laboratory.

11. L. Elterman, "UV, Visible, and IR Attenuation for Altitudes to
     50 km", AFCRL-68-0153, Environmental Research Papers Report 285,
     April 1968.

12. NASA Earth Resources Technology, Satellite-Data Users Handbook,
     General Electric Company, Space Division, 5030 Herzel Place,
     Beltsville, Maryland, 20705, Section A.

13. Strong Electric Division of Holophane, Johns - Manville Sales
     Corporation, Toledo, Ohio.

14. Ogletree, G., G. Karthas and M. Smith, "Interim Technical Report
     No. 1, Advanced Earth Observation System Instrumentation Study
     (AEOSIS)", Report R-792, CSDL, February 1974.

15. Smith, M., "Problems Pertaining to the Sight Vector of a Spaceborne
     Imaging Radiometer", Report R-785, CSDL, January 1974.

16. R. White, et.al., "Interim Technical Report No. 3, Advanced Earth
     Observation System Instrumentation Study (AEOSIS)", CSDL Report
     R-965, December 1975.

R-963
FINAL REPORT
DISTRIBUTION LIST

NASA/GSFC

NAME	CODE	NO.COPIES	NAME	CODE	NO.COPIES
R. Schwartz	287	1	J.R.Schulman	726	1
B. Peavey	563	10	P. Hui	726	1
R.T. Groves	580	1	O. Weinstein	726	1
D.L. Blanchard	580	3	J.H. McElroy	723	1
A. Fuchs	582	5	T.E. McGunigal	723	1
W.G. Stroud	110	1	M.W. Fitzmaurice	723	1
J.H. Boeckel	700	1	A. Guha	730	1
A.E. Jones	700	1	L. Walter	920	3
H.C. Hoffman	712	2	P. Schmidt	932	1
F.J. Kull	712	1	J. Gatlin	942	1
S. Kant	720	10	M. Maxwell	943	1
H.W. Price	720	1	T. Ragland	430	3
Systems Reliability Branch	300	1	Publications Branch	251	1
			Patent Counsel	204	1

NASA/Washington

Headquarters Library   1

NASA/JSC

Library   1

INTERNAL

M. B. Adams   J. Gilmore   R. McKern
P. Cefola   F. Grant   G. Ogletree
D. Cox   R. Harris   E. Olsson
R. Crisp   J. Harrison   G. Ouellette
K. Daley   D. Hoag   R. Ragan
W. Denhard   J. Hursh   R. Ramnath
P. Dogan   R. Hutchinson   T. Reed
W. Drohan   L.B. Johnson   W. Robertson
R. Duffy   B. Kriegsman   N. Sears
T. Edelbaum   A. Laats   K. Soosaar
P. Felleman   J. Lanfranchi   R. Var
K. Fertig   H. Malchow   B. Walker
E. Gai   R. Marshall   R. White

Technical Information Center (10)
AFPR/CSDL Capt. R.T. Evans

MIT

Charles Hayden Library
Engineering Library
Aeronautics and Astronautics Library

D-1